CONTROLLED SYNTHESIS OF ORGANIC-INORGANIC COMPOSITE PARTICLES

A THESIS SUBMITTED TO
THE GRADUATE SCHOOL OF NATURAL AND APPLIED SCIENCES
OF
MIDDLE EAST TECHNICAL UNIVERSITY

BY

ELİF ERÇELİK

IN PARTIAL FULFILLMENT OF THE REQUIREMENTS
FOR
THE DEGREE OF MASTER OF SCIENCE
IN
CHEMICAL ENGINEERING

AUGUST 2022

Approval of the thesis:

CONTROLLED SYNTHESIS OF ORGANIC-INORGANIC COMPOSITE PARTICLES

submitted by **ELİF ERÇELİK** in partial fulfillment of the requirements for the degree of **Master of Science** i**n Chemical Engineering, Middle East Technical University** by,

Prof. Dr. Halil Kalıpçılar
Dean, Graduate School of **Natural and Applied Sciences** _____

Prof. Dr. Pınar Çalık
Head of the Department, **Chemical Engineering** _____

Assoc. Prof. Dr. Emre Büküşoğlu
Supervisor, **Chemical Engineering, METU** _____

Prof. Dr. Nihal Aydoğan
Co-Supervisor, **Chemical Engineering, Hacettepe University** _____

Examining Committee Members:

Assoc. Prof. Dr. Simge Çınar-Aygün
Metallurgical and Materials Engineering, METU _____

Assoc. Prof. Dr. Emre Büküşoğlu
Chemical Engineering, METU _____

Prof. Dr. Nihal Aydoğan
Chemical Engineering, Hacettepe University _____

Assoc. Prof. Dr. Harun Koku
Chemical Engineering, METU _____

Assist. Prof. Dr. Gökçe Dicle Kalaycıoğlu
Chemical Engineering, Hacettepe University _____

Date: 26.08.2022

I hereby declare that all information in this document has been obtained and presented in accordance with academic rules and ethical conduct. I also declare that, as required by these rules and conduct, I have fully cited and referenced all material and results that are not original to this work.

Name Last name : Elif Erçelik

Signature :

ABSTRACT

CONTROLLED SYNTHESIS OF ORGANIC-INORGANIC COMPOSITE PARTICLES

Erçelik, Elif
Master of Science, Chemical Engineering
Supervisor : Assoc. Prof. Dr. Emre Büküşoğlu
Co-Supervisor: Prof. Dr. Nihal Aydoğan

August 2022, 112 pages

Liquid crystal (LC) is a state of matter having long-range orientational order between crystalline solid and isotropic liquid, and its molecular orientation can be altered with external stimuli. The polymerization of liquid crystal droplets has been widely used for the synthesis of LC-templated functional materials due to its ordering property and fluidic behavior. In this study, we investigated the synthesis of composite particles with controlled internal and interfacial structure using surface-modified nanoparticles-adsorbed LC droplets as templates. In the first part of this study, we synthesized silica nanoparticles, silver nanoparticles, and iron oxide nanoparticles and modified their surfaces by using thiol or silane groups to procure either planar, tilted, or homeotropic anchoring to LC droplets and pH-dependent surface charge, hydrophobicity, and hydrophilicity. Secondly, we adsorbed nanoparticles to the LC-aqueous interface and characterized the configurations (internal structuring) of LC droplets. We showed that surface chemistry, concentration, and surface charging of nanoparticles affect the change in configuration of LC droplets and form heterogeneity on the surface. According to our results, adsorption of silver and iron oxide nanoparticles modified with 1-decanethiol and 1-hexadecanethiol (-C10/C16 mixed monolayers of thiols) showed a transition from bipolar to radial, whereas -

COOH/C16 mixed monolayers of thiol terminated nanoparticles (tilted) changed the configuration to preradial. Adsorption of silica nanoparticles modified with dimethyloctadecyl [3-(trimethoxysilyl) propyl] ammonium chloride (DMOAP, homeotropic) and -COOH/DMOAP terminated counterparts exhibited a configuration change from bipolar to radial and preradial, respectively. -NH_2 and -COOH terminated counterparts (planar) did not change the configuration. Thirdly, we used -NH_2 and -COOH terminated silica nanoparticles with different sizes (51.2 nm ± 9.0 nm to 417.1 nm ± 22.1 nm), tuned their surface charges by changing pH, and finally polymerized the LC droplets after adsorption. Charging property of -NH_2 and -COOH terminated silica nanoparticles provided adsorption control. We showed partial coverage of charged, surface-modified silica nanoparticles to enable their preferential positioning, which offered control over the interfacial structure for composite particles. These results in this study provide a basis for synthesizing anisotropic, polymeric composite particles with complex structures for technological products, biomedical or sensing applications.

Keywords: Liquid Crystal Emulsions, Nanoparticles, Internal Structuring, Surface Charge, Polymerization

ÖZ

ORGANİK-İNOGANİK KOMPOZİT PARÇACIKLARIN KONTROLLÜ SENTEZLENMESİ

Erçelik, Elif
Yüksek Lisans, Kimya Mühendisliği
Tez Yöneticisi: Doç. Dr. Emre Büküşoğlu
Ortak Tez Yöneticisi: Prof. Dr. Nihal Aydoğan

Ağustos 2022, 112 sayfa

Sıvı kristal, kristal katı ve izotropik sıvı arasında uzun ölçekli yönelim düzenine sahip bir madde halidir ve moleküler yönelim dış uyaranlarla değiştirilebilir. Sıvı kristal damlacıkların polimerizasyon yöntemleri, oryantasyon özelliği ve akışkan davranışı nedeniyle sıvı kristal şablonlu fonksiyonel malzemelerin sentezi için yaygın olarak kullanılmaktadır. Bu çalışmada, yüzeyi modifiye edilmiş nanoparçacıklar-adsorbe edilmiş LC damlacıkları şablon olarak kullanılarak kontrollü iç ve arayüzey yapısına sahip kompozit parçacıkların sentezi araştırılmıştır. Bu çalışmanın ilk bölümünde silika, gümüş ve demir oksit nanoparçacıklarını sentezlenmiş, yüzey özelliklerini tiyol veya silan grupları kullanarak sıvı kristal damlacıklarına düzlemsel, eğimli veya homeotropik çapalanma sağlamak ve pH'a bağlı yüzey yükü, hidrofobiklik, hidrofiliklik özellik göstermek için modifiye edilmiştir. İkinci olarak, nanoparçacıklar sıvı kristal-sulu arayüzüne adsorbe edilmiş ve sıvı kristal damlacıklarının konfigürasyonları (iç yapılanma) karakterize edilmiştir. Nanopartiküllerin yüzey kimyası, konsantrasyonu ve yüzey yüklerinin sıvı kristal damlacıklarının konfigürasyonundaki değişikliği etkilediği ve yüzeyde heterojenlik oluşturduğu gösterilmiştir. Elde edilen sonuçlara göre, 1-dekanetiyol ve

1-heksadekantiyol (-C10/C16 karışık tek tabakalı tiyoller) ile modifiye edilmiş gümüş ve demiroksit nanoparçacıklarının adsorpsiyonu bipolardan radyal hale geçişini sağlarken, -COOH/C16 karışık tek tabakalı tiyol sonlandırılmış nanoparçacık (eğimli) adsropsiyonu konfigürasyonu preradyal olarak değiştirdiği gösterilmiştir. Dimetiloktadesil [3-(trimetoksisilil) propil] amonyum klorür (DMOAP, homeotropik) ve -COOH/DMOAP ile sonlandırılmış muadilleri ile modifiye edilmiş silika nanoparçacıklarının adsorpsiyonu, sırasıyla bipolardan radyal ve preradyal konfigürasyon değişikliği gözlemlenmiştir. -NH_2 ve -COOH sonlandırılmış muadilleri (düzlemsel) ise damlacık konfigürasyonunu değiştirmediği gözlemlenmiştir. Üçüncü olarak, farklı boyutlarda (51.2 nm ± 9.0 nm ila 417.1 nm ± 22.1 nm) -NH_2 ve -COOH sonlandırılmış silika nanoparçacıkları kullanılmış, ortam pH'ı değiştirilerek yüzey yükleri ayarlanmış, ve son olarak adsorpsiyondan sonra sıvı kristal damlacıkları polimerize edilmiştir. -NH_2 ve -COOH bitişli silika nanoparçacıklarının yük özelliği adsorpsiyon kontrolünü sağlamıştır. Kompozit parçacıklar için arayüzey yapısı üzerinde kontrol sağlayan tercihli konumlandırmayı sağlamak için yüklü, yüzeyi modifiye edilmiş silika nanoparçacıkların kısmi kapsamı gösterilmiştir. Bu tezde elde edilen sonuçlar, teknolojik ürünler, biyomedikal veya algılama uygulamaları için karmaşık yapılara sahip anizotropik polimerik kompozit parçacıkların sentezi için bir temel sağlamaktadır.

Anahtar Kelimeler: Sıvı Kristal Emülsiyonları, Nanoparçacık, İç Yapılanma, Yüzey Yükü, Polimerizasyon

To my family

ACKNOWLEDGMENTS

Firstly, I would like to express my deepest gratitude to my advisor, Assoc. Prof. Dr. Emre Büküşoğlu for his support, guidance, and patience throughout this study. With his support during my undergraduate and graduate studies, he always kept me motivated for my work. I would also like to express my sincere gratitude to my co-supervisor Prof. Dr. Nihal Aydoğan, for her support and helpful suggestions.

I would also like to thank to Soft and Functional Materials Laboratory Group members; Özge Batır, Aslı Karausta, Elif Kurt, Ali Akman, R. Umut Dinç, Selin Şengül, Ceren Kocaman, Dr. Pınar Beyazkılıç Ayas, and Dr. Selda Sezer. During this journey, they became not only my colleagues but also one of my closest friends. Apart from the information Özge Batır gave me as a teaching assistant, I would like to thank her for her moral support and devotion to performing my SEM samples imaging. I would like to thank Aslı Karausta for her support throughout my study and positivity during the weekend laboratory work. I would like to thank Elif Kurt for our fun memories and transportation support in Ankara. I would thank Ali Akman for his patience with my various questions and for helping to perform my SEM samples imaging. I would like to thank R. Umut Dinç for his humor, vast knowledge, and support. I would like to thank Selin Şengül for her help and understanding towards my endless questions. I would like to thank Ceren Kocaman for her work discipline, that I admire, motivation, and fun.

My family deserves the greatest thanks for the patience, support, understanding, and trust they have shown throughout my entire education life. Deepest thanks to Mehtap Pektaş, Bülent Erçelik, Venüs the cat for always being there for me.

Lastly, I would like to thank Ayberk Canpolat for his unconditional love, patience, dedication, and encouragement since he came into my life.

For financial support, I would like to thank the Scientific and Technological Research Council of Turkey under grant number TÜBİTAK 219M068.

TABLE OF CONTENTS

LIST OF TABLES

TABLES

LIST OF FIGURES

FIGURES

CHAPTER 1

INTRODUCTION

Polymeric microparticles have been used in various applications, including drug delivery[1,2], sensors[3], separation processes[4,5], catalyst[6,7]. The shape, surface property, and internal structure of polymeric particles play critical roles in the material sciences or design applications. For instance, the polymeric network and shape complexity of particles are important parameters for drug delivery rate[2] or carrier performance[8], and emulsion stability[9]. Application areas can be increased to fields of biomedical[10], electric, magnetic[11], and self-cleaning[12] by polymeric materials decorated with colloids, with chemically various surfaces. Herein, polymeric particles designed with colloids, so-called polymeric composite particles, requires scientific advancements in terms of shape, internal and interfacial structuring for fundamental information and advanced applications. A broad and simple family of templates for synthesizing spherical and nonspherical polymer composite particles with chemical patches has been investigated using liquid crystal (LC)[13].

LCs are condensed fluid phases that are thermodynamically stable at temperatures intermediate to crystalline solids and isotropic liquids in which constituent molecules (mesogens) possess a high level of fluidic mobility and long-range ordering (micrometer scale[14]) (Figure 1.1). LCs are categorized as thermotropic when the phase behavior changes with temperature. With increasing the temperature of the system, the mobility of LC mesogens increases, and eventually, they lose their orientational ordering, and the state is changed to isotropic. Mesogens in LCs are ordered over a long range, which gives the bulk material anisotropic mechanical and optical qualities that are frequently found in crystalline solids. However, unlike a crystalline solid, the mesogens can diffuse at rates comparable to isotropic liquids[15]. The simplest phase of thermotropic LCs is called nematic (e.g., 4-cyano-4′-

pentylbiphenyl (5CB) at room temperature), in which the mesogens align in an average order, so-called nematic director, without any positional order.

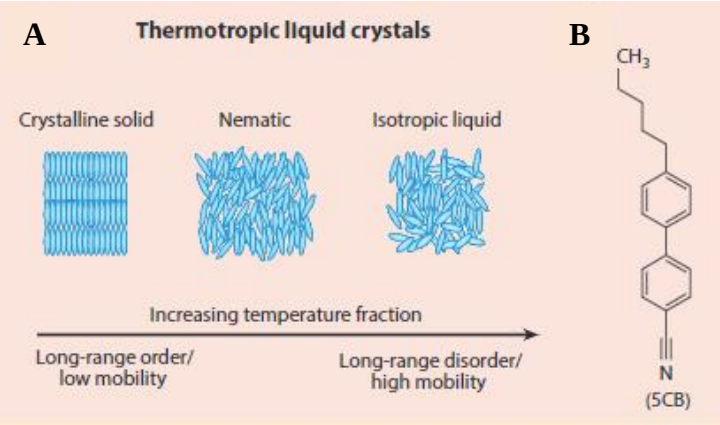

Figure 1.1 (A) Schematic illustration of the temperature-dependent phase behavior of thermotropic LCs, (B) the molecular structure of the 5CB, nematic LC [15].

The orientation of LC molecules changes according to three key concepts that define the LC orientation[15]. The first key concept is the surface anchoring that can be defined as the surface-induced ordering of LCs and it results from the intermolecular interaction of LC mesogens and confining medium (e.g., droplets, microwells, porous materials, etc.). In the absence of an external field, the molecules of LCs, align in the direction of the easy axis, which states the lowest free energy of the orientation of the LC director. The external field, such as magnetic or electrical force, causes a perturbation to the orientation of LC molecules which causes free energy increase and results in deviation of director from the easy axis, as shown in Figure 1.3A. The interfacial free energy is described in Equation 1.

$$F_s = F_o + \frac{1}{2} W_a \sin^2(\theta_s - \theta_e) \qquad \text{(Equation 1)}$$

where F_s is interfacial free energy, F_o is free energy of the interface from easy axis, W_a is surface anchoring energy and θ_s and θ_e denotes the angles of surface director and easy axis. Depending on how LC molecules are positioned at the interface, two different surface anchoring conditions are created. LC molecules align perpendicular

to the surface for homeotropic anchoring (Figure 1.2A). On the other hand, planar anchoring develops when the alignment is parallel to the surface (Figure 1.2B).

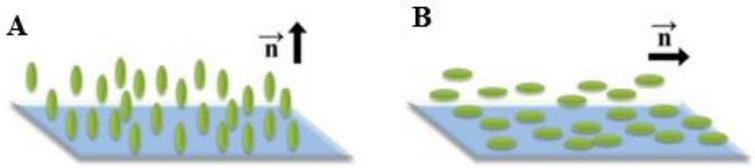

Figure 1.2 Schematic illustration of (A) homeotropic and (B) planar anchoring condition [16].

The second key concept is the elasticity of LCs, which provides long-range orientational ordering of mesogens in LC. There are three main types of strain in LC, which are splay, twist, and bend, as shown in Figure 1.3B. The Frank-Oseen equation describes the free energy density as follows,

$$F_e = \frac{1}{2}K_1(\nabla \cdot \underline{n})^2 + \frac{1}{2}K_2(\underline{n} \cdot \nabla \times \underline{n})^2 + \frac{1}{2}K_3[\underline{n} \times (\nabla \times \underline{n})]^2 \qquad \text{(Equation 2)}$$

where K_1, K_2 and K_3 are the splay, twist, and bend elastic constants, respectively.

The third key concept is the topological defects. Surface-induced orientation of mesogens through continuous strain cannot always be accommodated when LC is confined in a particular geometry. In some regions, LC locally melts, and these regions correspond to singularities in the director profile (Figure 1.3C).

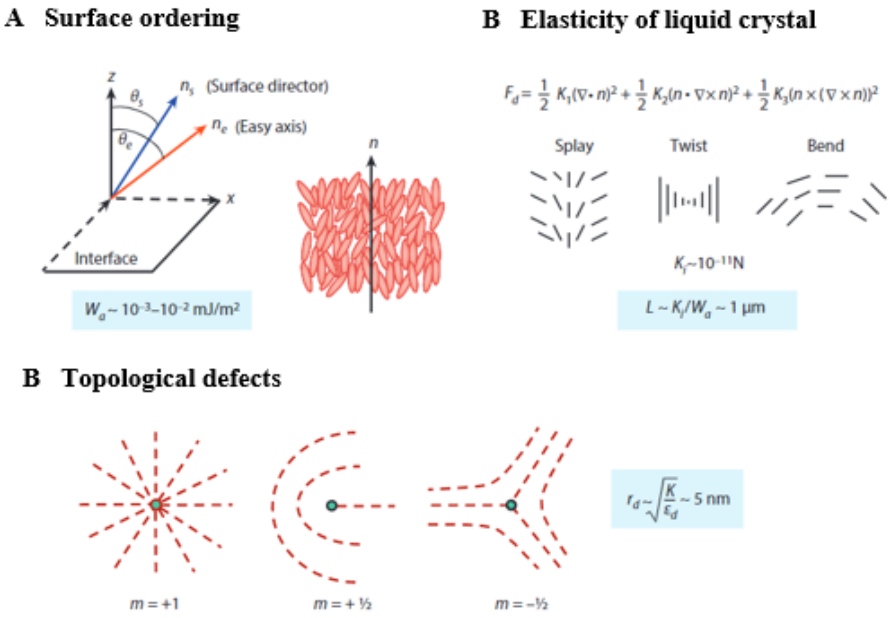

Figure 1.3 Schematic illustrations of key concepts of LC. (A) surface director and easy axis of LC on a surface, (B) basic modes of deformation of a LC, (C) types of topological defects [15].

Topological defects develop because of competition between surface anchoring and elastic energies that result from the confinement of LC in a geometry. As a result of this competition, LC droplets can take on various configurations, including bipolar, axial, preradial, escaped radial, and radial, as shown in Figure 1.4. LC droplets exhibit optical birefringence due to their anisotropic nature, which makes it possible to determine the orientation of LCs under crossed polarizers by affecting the polarization of transmitted light. Due to the long-range ordering of the LCs, the interaction of LC mesogens with chemical or biological species can result in an ordering transition of the LC phase, which can be observed using a polarized optical microscope (POM). In a medium that has strong planar anchoring conditions such as glycerol, pure water, or poly(vinyl alcohol) (PVA), LC droplets exhibit bipolar configuration, which is characterized by two boojum defects located at the poles of the droplet as shown in Figure 1.4A[17,18]. According to the interfacial anchoring condition, the equilibrium configuration of the LC droplet may change. Configuration of LC droplet change to radial when the homeotropic anchoring is

induced on LC droplets. A single point defect at the center of the droplet serves as the defining feature of the radial director configuration (Figure 1.4F). Cross-like (four-petal) pattern is observed under the polarized micrograph (crossed polarized)[17]. In between planar to homeotropic anchoring conditions, LC droplets exhibit various equilibrium states from bipolar to radial, depending on the interfacial tilting of the mesogens (Figure 1.4B-E). The first one is the axial configuration which is characterized by line disclination on the LC droplet interface (Figure 1.4B-C). Under the POM, the axial configuration is identified by a bright loop at the equator of the droplet. An increase in the anchoring strength results in the disappearance of line disclination and the appearance of one point defect on the vicinity of the LC-water interface, and this configuration is called preradial (Figure 1.4D). Preradial configuration is identified as an angle-dependent bright appearance under POM. Before the point defect is located in the center of the droplet (radial configuration), the point defect is located between the surface and center of the droplet, which is called an escaped radial configuration (Figure 1.4E)[17].

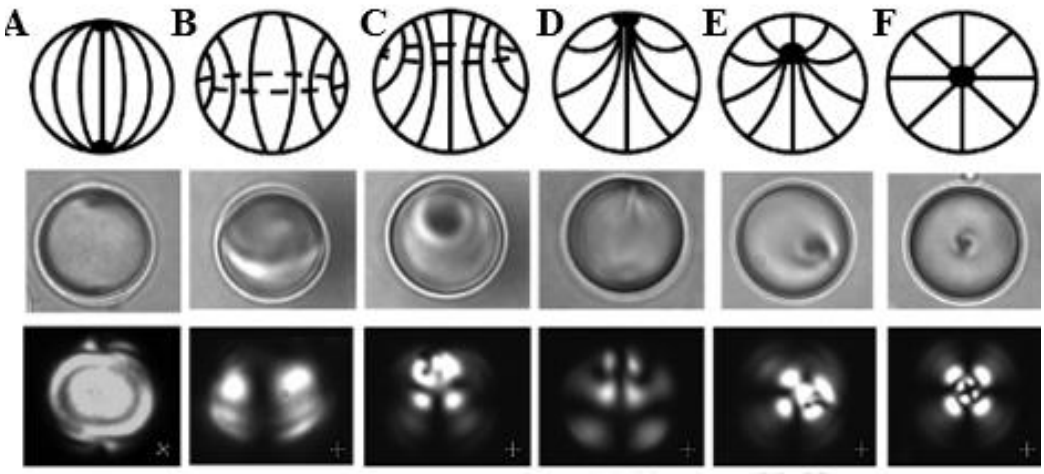

Figure 1.4 LC droplets maintained (A) bipolar, (B-C) axial, (D) preradial, (E) escaped radial, (F) radial configurations. The schematic illustrations, bright field, and polarized light micrographs are introduced from top to bottom line [17].

Theoretically, a characteristic size scale between 1-10 μm is obtained by comparing the elastic energy, which scales with KL (where K is the elastic constant with one constant approximation (~10^{-11} N) and L is the characteristic length scale), to surface

anchoring energy, which scales with~WL^2 (W is anchoring energy, typically 10^{-3}-10^{-2} mJ/m^2). While larger droplets continue to maintain configurations that satisfy the surface anchoring conditions at their interfaces, LC droplets below this range are expected to adopt a strain-free, uniform director alignment[19].

These three key concepts allow designing LCs within confined systems such as droplets in specific configurations. Mesogenic reactive molecules, such as 4-(3-acryloyoxy-propyloxy) benzoic acid 2- methyl-1,4-phenylene ester (RM257), containing diacrylate groups have been widely employed in the synthesis of aligned, structured polymeric materials using these configurations in literature[13,19–25]. The photopolymerizable diacrylate resin employed in several applications because these molecules are easily crosslinked to create structured polymeric materials when a photoinitiator is present. The RM257 shows nematic LC phase property in the temperature rate of 87-118ºC. To maintain nematic phase at room temperature, reactive mesogen RM257 can be combined with non-reactive LCs, like 5CB. For a high concentration of 5CB, RM257/5CB mixtures are entirely miscible in the nematic state at room temperature. As shown in Figure 1.5, due to their inter-miscibility, the nematic phase of 5CB at room temperature may have caused RM257 to align the direction of 5CB mesogens. The UV curing and 5CB extraction processes led to synthesizing oriented polymeric structures with different internal polymeric networks or shapes[26]. Polymerization of RM257/5CB mixtures allows for the synthesis of anisotropic polymeric particles.

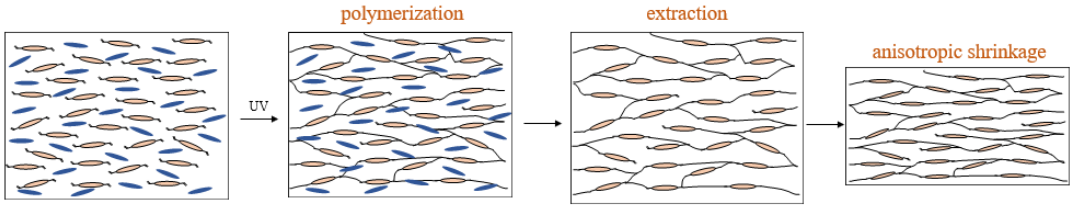

Figure 1.5 Schematic illustration of the polymerization of reactive mesogen (orange) and non-reactive mesogen (blue) mixture.

Interactions of LCs and nano and micrometer-sized particles and organization at the interface of LC-water have been studied in literature[27,28]. Especially nanoparticles-

LC interactions gain interest because of two crucial phenomena. The first phenomena are the elastic energy and surface anchoring energy competition on the size scale close to 1 μm, as mentioned above. The elastic and surface anchoring energy balance determine the particle characteristics on LC. The elastic energy of LC dominates the characteristics of particles that smaller than 1 μm (L<<K/W), and the orientation of LC is not affected, so the surrounding director mostly be uniform. The large particles (L>>K/W) cause disturbance in the liquid crystal and the molecules form a new equilibrium, providing the surface anchoring condition[29]. Furthermore, nanoparticles can be synthesized in different shapes and with different surface properties, which serves makes them a tool for specific applications such as drug delivery and sensors. In that manner, it was discovered that adsorption of surface-modified nanoparticles to the LC droplets controllably changes the configurations, which gives a unique opportunity to design sensing applications for viruses and bacteria showing similar surface characteristics[28]. This study, its findings, and unique properties of nanoparticles increase the interest in the study of the LC-nanoparticle interactions. In addition, this research revealed that designing chemically patched particles is possible with nanoparticles with different surface chemistry adsorbed to the LC-water interface. Therefore, considering these two critical phenomena, nanoparticle and LC interactions and the design of functional chemically patched polymeric composite particles should be studied in detail.

New scientific and technological developments are made possible by creating particles with either anisotropic shapes or patterned surface chemistry with nanoparticles. For instance, it has been demonstrated that particle shape affects the effectiveness of intracellular delivery of particles, colloidal interactions between particles either adsorbed at liquid–liquid interfaces (LC) or dispersed in LC solvents, the stability of particle-decorated (Pickering) emulsions, and Brownian motion[13]. Moreover, new pathways for the creation of functional colloidal materials are being opened by micrometer-sized particles having chemical surface patterns that mediate site-specific interactions.

This study aims to synthesize micrometer-sized composite particles with controlled internal and interfacial structuring using surface-modified nanoparticle-adsorbed LC droplets as templates. We carried out experiments on the adsorption of surface-modified nanoparticles to the LC-water interface in droplet confinements and investigated the response of LC droplets (for internal structuring) and preferential patterning of multiple nanoparticles at the interface (for interfacial structuring). We were motivated to control the adsorption of nanoparticles to the interface by changing the parameters of the emulsion medium, such as concentration, pH, and size of nanoparticles. Nanoparticles are known to have unique surface functionalization properties, as mentioned above, so we examined the nanoparticle surface property dependence of LC configuration upon adsorption of nanoparticles to emphasize the internal structuring control via nanoparticles. For this purpose, we used silver nanoparticles (Ag NPs), iron oxide nanoparticles (IONPs), and silica nanoparticles (Si NPs) and modified their surfaces by using thiols or silane groups which provided hydrophobic, hydrophilic, and pH-dependent surface charging. We examined the effects of nanoparticle base and surface properties on the configuration of LC droplets. To highlight the interfacial structuring control, lastly, we used surface-modified silica nanoparticles of different sizes, tuned their surface charges by changing pH, and performed the preferential positioning of nanoparticles which offered control over the interfacial structure by polymerization.

CHAPTER 2

LITERATURE REVIEW

In literature, there are several methods proposed to synthesize polymeric materials or polymer composites with emulsions[30,31], Pickering emulsion[32], in situ polymerization[33], soft lithography[34,35], photolithography[36], microfluidics[37], molecular imprinting[38] among others. Although several template materials and processes have been used to synthesize polymer composites; anisotropic templates, such as liquid crystals (LCs), are considered a step forward. Successful methodologies have offered control over the size, shape, color, and internal structuring introduced to produce LC-templated polymeric materials that can broaden the application of polymeric materials such as membranes or gas sensors[22–25,39,40]. To date, different LC phases and confinement media were studied; however, composite particles were not, although they provide a diverse use. Nanoparticles can be employed to impart a desired functional attribute into the patchy microparticle since they can be positioned on the LC droplet interface and have varied compositions and characteristics. The orientation of the LC molecules can be predetermined since the ordering of LCs in confined geometries can be modified by altering the characteristics of their surrounding environment, which enables the internal structuring of polymer composites. Besides, interfacial structuring can be introduced by tuning the interparticle interactions.

Recent studies demonstrated that the orientation of LCs molecules changed with external triggers (gas molecules[41–43] or chemical molecules-proteins[44,45]) at LC-solid interfaces. Cadwell et al. used LCs-solid interface (LCs on copper(II) and nickel(II) perchlorate salt-treated surfaces) and they obtained homeotropic anchoring condition (dark appearance of LCs) initially [43]. Upon exposure to 10 ppm dimethoxymethyl phosphine oxide (DMMP) by flowing a gas stream of nitrogen for 5 min, they

obtained a change in the optical appearance of copper(II) substrate (dark to bright image), but the optical signal did not change for nickel(II) substrate (still dark appearance). They found the ordering transition occurs upon exposure of DMMP from homeotropic to planar for copper(II) substrate (Figure 2.1).

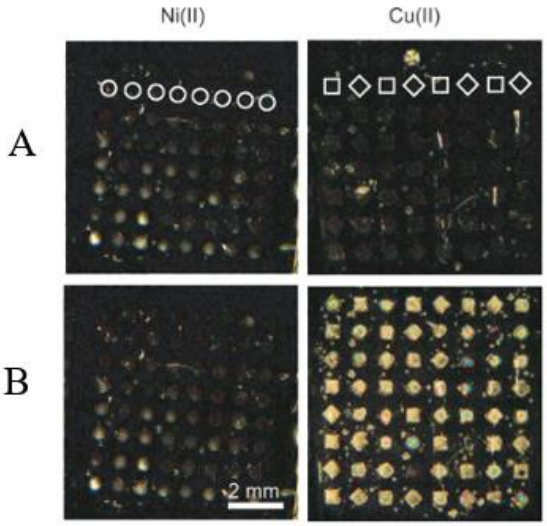

Figure 2.1 Optical images of 5CB on nickel(II) or copper(II) perchlorate salt-treated surface (A) before, (B) after the exposure of 10 ppm DMMP in nitrogen[43].

The LC-aqueous interface offers more advantages; firstly, it possesses the mobility of particles, and secondly, easy organization of molecules at the interface[46]. Brake et al. reported spontaneous assembly of phospholipids at planar LCs-aqueous interface [47]. They placed LCs on octadecyltrichlorosilane (OTS) coated glass, and the top part of the system was an aqueous phase (Figure 2.2A). OTS-coated glass caused LC to homeotropic anchoring (perpendicular orientation) at bottom and at the top water interface caused to be LC planar anchoring (parallel orientation). The initial optical appearance of the system is shown in Figure 2.2B (bright domains). When the system started to come across phospholipid (L-α-dilauroyl phosphatidylcholine (L-DLPC)) at the aqueous interface, the dark domains appeared (Figure 2.2C-D) which corresponds to the homeotropic anchoring for top and bottom part. They proposed the self-assembly of phospholipids on the LC-aqueous interface, which changes the orientation of LC molecules.

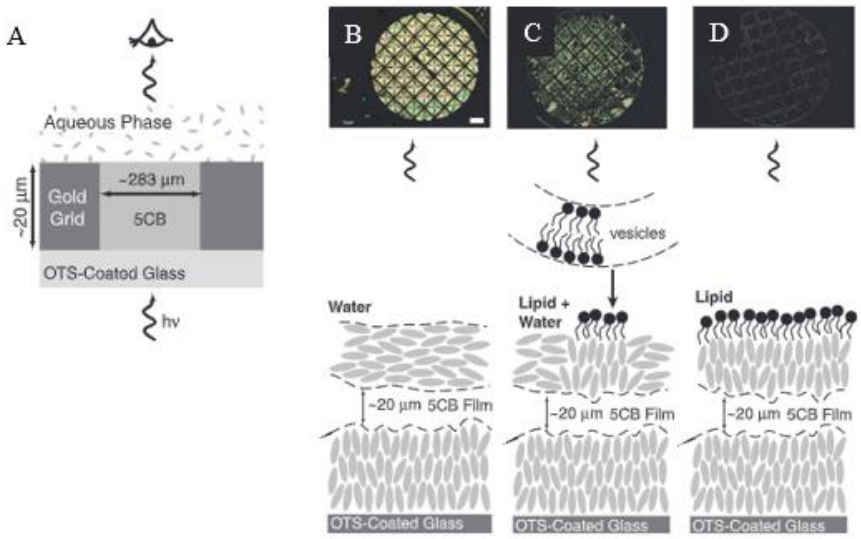

Figure 2.2 (A) Schematic illustration of the experimental system, (B) optical images and illustrations of the initial system which indicates planar anchoring at LC-aqueous interface, optical images, and illustrations of anchoring transition of 5CB after (C) 15 min L-DPLC, (D) 2h L-DPLC[47].

Brake et al. reported that reversible adsorption of amphiphiles to LC-aqueous interface changes in the orientation of LC[48]. They analyzed the optical appearance of 5CB confined in copper grids when contacting the aqueous suspensions of increasing concentration of sodium dodecyl sulfate (SDS). In the absence of SDS, the optical image showed in-plane birefringence and four dark brushes emanating from a single point related to planar anchoring. With increasing SDS concentration, the number of dark brushes decreases, and the fraction corresponding to homeotropic alignment regions increases. At concentration > 1 mM, uniformly dark regions appeared (homeotropic alignment). They added sodium chloride (NaCl) to the system, which screens the electrostatic repulsion and repeated experiments with various NaCl and SDS concentrations, as shown in Figure 2.3. For example, the addition of a NaCl concentration of 0.01 M caused an orientation transition of 5CB in the presence of 0.1 and 0.32 mM SDS; however, in the absence of NaCl, those SDS concentration was not enough to induce homeotropic alignment. They stated that the NaCl promotes the adsorption of SDS to hydrophobic interface (5CB), so change in orientation of LC by the addition of NaCl with SDS.

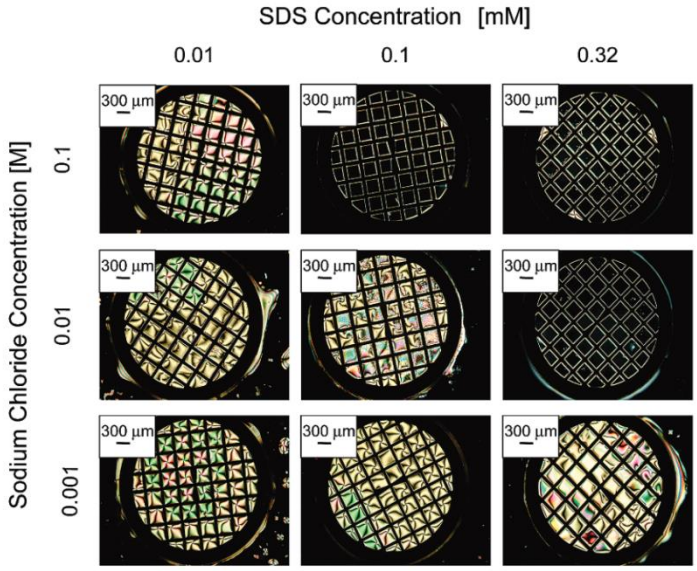

Figure 2.3 Optical images of 5CB confined in grids contacted with an aqueous solution of NaCl and SDS with different concentrations[48].

The LC-aqueous interface requires special treatment of the contacting reference interface for configuration determination. On the other hand, the initial configuration of LC emulsions can be easily determined by the surface chemistry of droplets without any treatment. The fabrication of LC droplets is easier than planar LCs films. The fabrication methods can be listed as vortexer, sonicator, homogenizer, hand shearing, polymer capsules, and microfluidics[20]. The predetermined sizes can be obtained by designing the fabrication method properly. Moreover, they have a higher degree of sensitivity due to the surface anchoring and elastic energy competition. Owing to these advantages, LC-aqueous interfaces are preferred in droplet geometry with well-defined configurations.

As in Brake et al. work, the orientation of LC can be changed with a chemical such as surfactants for droplets. Gupta et al. demonstrated that LC droplets configuration was reversibly changed from bipolar to radial upon the addition 1 mM of sodium dodecylsulfate (SDS) to the aqueous interface[17]. They reported equilibrium configuration states (preradial, escaped radial, axial) with the increasing concentration of SDS from 0 mM to 1 mM. The ordering transition of LC droplets is shown in Figure 1.4.

Micrometer sized particles-LCs interaction and colloid characteristics in LC medium were also investigated, which can be broadened to interfacial structuring for polymer composite particles. It is stated that small particles with L<<K/W do not disturb the surrounding director (Figure 2.4A), but large particles L>>K/W disturb the director to satisfy the surface anchoring condition (Figure 2.4B-C) [29]. The liquid crystal can be categorized into these two extreme cases (i) colloids with weak intrinsic anchoring and (ii) high intrinsic anchoring. The experimental study of this phenomenon was done by Loudet et al[49]. They proposed that smaller particles (silicone oil droplets) with homeotropic anchoring conditions did not induce a strong disturbance, so particles were randomly located in the LC phase (Figure 2.4D). Because of the satellite point defect, the large particles aligned with the direction of LC (Figure 2.4E)[49]. Lastly, Muševič et al. reported a change in LC orientation due to the confinement of microparticles in LCs[14]. They introduced micrometer-sized silica particles with homeotropic anchoring conditions to the glass cell containing LCs with various cell thicknesses. For the thicker parts of the cell, micrometer-sized silica particles with homeotropic anchoring conditions were found to be in dipolar order, and the direction of chains parallel to the rubbing direction (Figure 2.4F-G). However, for the thinner parts of the cell, the particles were found to be formed in quadrupolar order with kinked chains which align perpendicular to the rubbing direction (Figure 2.4H-I). The different alignment and structured order arise from the attractive-repulsion force between particles. When the particles are introduced, the topological defects forms and the free energy of the system increases. Particles share the topological defects to decrease the free energy, and these phenomena increase the attraction force in between the particles, although the repulsive force increase due to the elasticity of LC molecules.

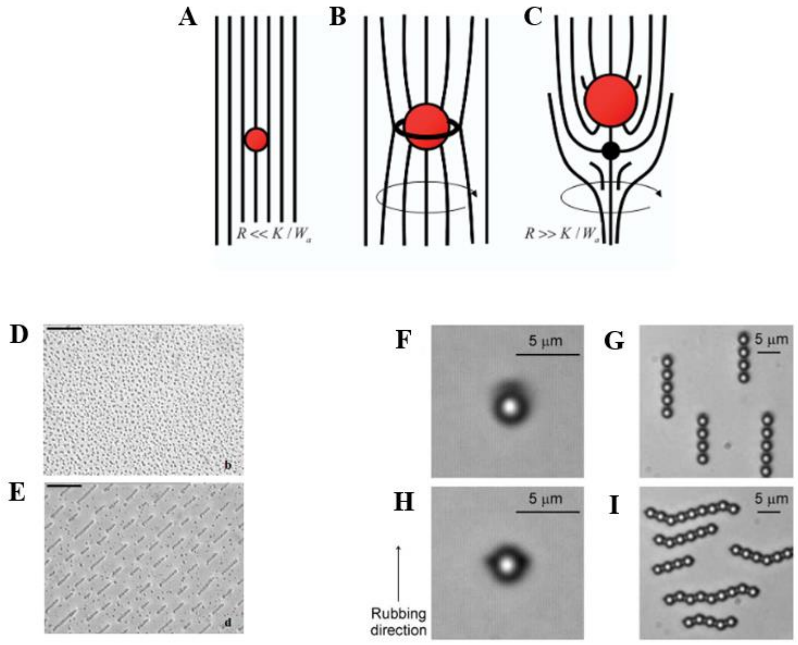

Figure 2.4 (A) Small size particle with homeotropic anchoring does not distort the director, (B-C) large particles change the director to satisfy surface anchoring, and the distorted configurations are quadrupolar (equatorial disclination loop) and dipolar (hyperbolic point defect-hedgehog) symmetries, respectively[29]. (D) Silicone-oil droplets of smaller size are randomly distributed in LC, (E) large particles form chains and are aligned parallel to LC director[49]. (F-H) Dipolar and quadrupolar silica particles in LC medium, (G-I) linear (dipolar), and kinked chains formed in LC for dipolar and quadrupolar symmetry of particles, respectively[14].

Interparticle interactions can be tuned by using surfactants in an LC medium. Koeing et al. reported that the addition of surfactant, sodium dodecylsulfate (SDS), to the system altered the ordering transitions of LC at the interface, which resulted in rotation of the topological dipole in the nematic 5CB about the microparticles at the interface[27]. As the concentration of SDS increased, there was an interparticle separation, and the chain structure of particles changed to hexagonal arrays (Figure 2.5). The interparticle separation represents a balance between a long-range attraction related to the strain of the LC and a short-range repulsion associated with the point defect. Short-range repulsion associated with the point defect is in charge of maintaining a limited separation between the surfaces of the microparticles in the absence of SDS. As a result of the topological dipole's rotation, a weakening of the attractive long-range attraction led to an increase in interparticle separation.

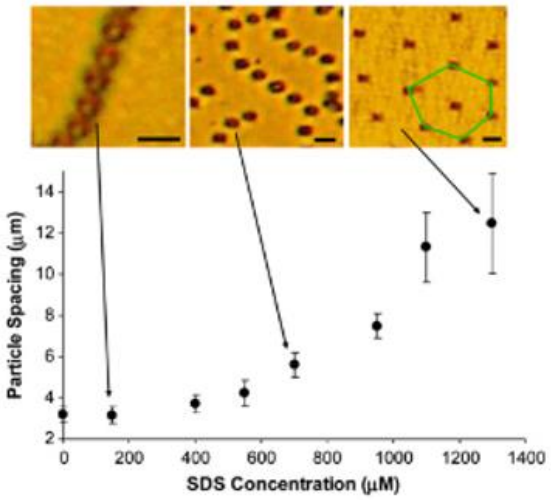

Figure 2.5 Reordering of the position of microparticles with adsorbate-induced ordering of LC[27].

Self-assembly of microparticles and packing arrangements were also investigated on LC droplets. Wang et al. investigated the organized assemblies of 1 μm sized polystyrene (PS) particles at the LC droplet, which have a diameter range of 7-20 μm[50]. They used 5CB droplet dispersed in pure water in bipolar configuration with two boojum defects. Two PS colloids adsorbed to one of the two boojums. They saw three packing patterns for droplets with three colloids adsorbed at a pole, each occurring with a distinct frequency (Figure 2.6A). The packing configurations most typically seen for droplets containing six or seven adsorbed colloids are shown in Figure 2.6B. The most typical packing configurations had a hexagonal symmetry. They saw the hexagonal array and pentamer ring pattern when multiple colloids were adsorbed on the LC droplets. They point out that the LC droplet's curved surface prevents a homogeneous hexagonal array of PS colloids from forming on its surface at full coverage. They also investigated the curvature effect on particle array formation. They sedimented particles on a planar LC-aqueous interface (20 μm thickness), and they did not observe spontaneously assembling into organized arrays as in droplet form (Figure 2.6C). They added 1 mM sodium chloride (NaCl) salt, which screened the electrostatic repulsion between PS particles, and the particles exhibited closed packed arrangement (Figure 2.6D). The organization of the particles

only developed in LC droplets due to the significant elastic energy cost associated with the splay elastic distortions. This work demonstrates the critical impact of curvature on interfacial particle structuring at the LC-aqueous interface.

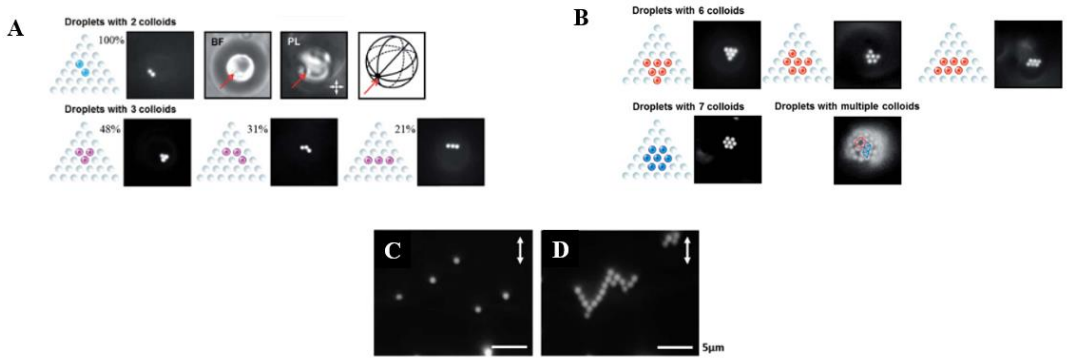

Figure 2.6 Schematic illustration, fluorescent micrograph, bright field, and polarized microscopy images of droplets with (A) two and three colloids, (B) six, seven, and multiple colloids, (C) PS colloids on planar LC-aqueous interface in pure water, (D) PS colloids on planar LC-aqueous interface in the presence of 1 mM NaCl[50].

The mixture of unreactive nematic LCs (5CB) and reactive mesogens (RM257) was used in the literature to synthesize LC-templated polymeric particles. Wang et al. reported that the templated synthesis of spherical and nonspherical polymeric micro-particles with complicated internal structure and porosity could be accomplished using aqueous dispersions of micrometer-sized liquid crystal (LC) droplets[21]. They photopolymerized reactive mesogens, removed the unreactive mesogens from polymeric particles using ethanol, and obtained specifically designed polymeric droplets with unique internal configurations. The creation of spindle-shaped, spherical, spherocylindrical, or tear-shaped polymeric microparticles was discovered to be templated by LC droplets with bipolar, radial, axial, or preradial configurations, respectively (Figure 2.7A-D). Also, extraction of 5CB from polymerized LC droplets caused shrinkage of microparticles in the orientation of LC molecules. For instance, shrinkage of microparticles for bipolar configuration was pronounced in the direction normal to the line connecting two boojums of bipolar configuration, resulting in spindle-shaped microparticles. In contrast to bipolar configuration, extraction of 5CB from polymeric particles with radial configuration led to spherical

polymeric particles. This result indicates the symmetric shrinkage for radial configuration. They highlighted that the internal structure (orientation of polymer network) depends on the initial configuration, which could broaden an approach to the synthesized pre-determined internal structure of polymeric particles. Moreover, they found pores with the size of 10-100 nm for spherical microparticles templated from radial configuration LC droplets. Each type of microparticle displays unique optical signals that point to an internal anisotropic polymer network that was LC-templated and minimum perturbation of polymerization on LC droplets.

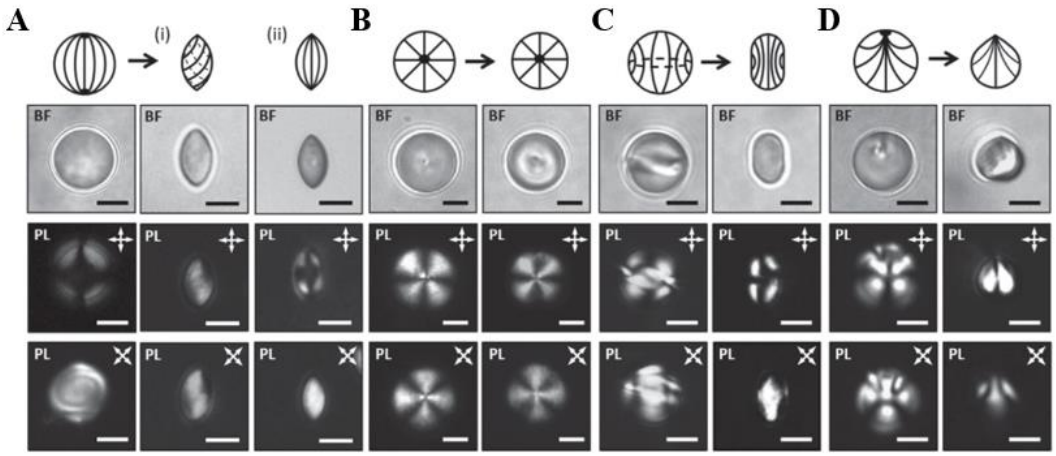

Figure 2.7 Synthesis of (A) spindle-shaped, (B) spherical, (C) spherocylindrical, or (D) tear-shaped polymeric microparticles templated from LC droplets in (A) bipolar, (B) radial, (C) axial, or (D) preradial configurations, respectively. BF indicates the bright field micrographs, whereas PL indicates the polarized light. The orientation of cross-polarized was indicated with white double-headed arrows[21].

The production of particles with either patterned surface chemistry or anisotropic form enables new scientific and technological advancements. Also, colloids with chemically modified surfaces open new routes for functional polymeric composite particles. Mondiot et al. reported that spherical and non-spherical particles with ordered chemically different domains could be built upon LC-based emulsions[13]. In particular, they demonstrated that LC droplets with two boojums might be utilized to drive the assembly of organic or inorganic colloids to the droplets' poles creating dipolar and quadrupolar droplets, which were ellipsoid-like shape particles with either one colloid located to one of the boojums or two colloids located two boojums

separately (Figure 2.8C-D). In addition, they absorbed microparticles on the interface of the pure (5CB) droplets and heated to isotropic temperature. They observed that colloids diffused toward one another (Figure 2.8A). They repeated the experiment after the polymerization, and they observed that the colloids on the interface of the polymerized droplets remained immobile after heating into the isotropic phase (Figure 2.8B). This result indicates that the microparticle position is preserved after polymerization, which enables the synthesis of durable and anisotropic particles.

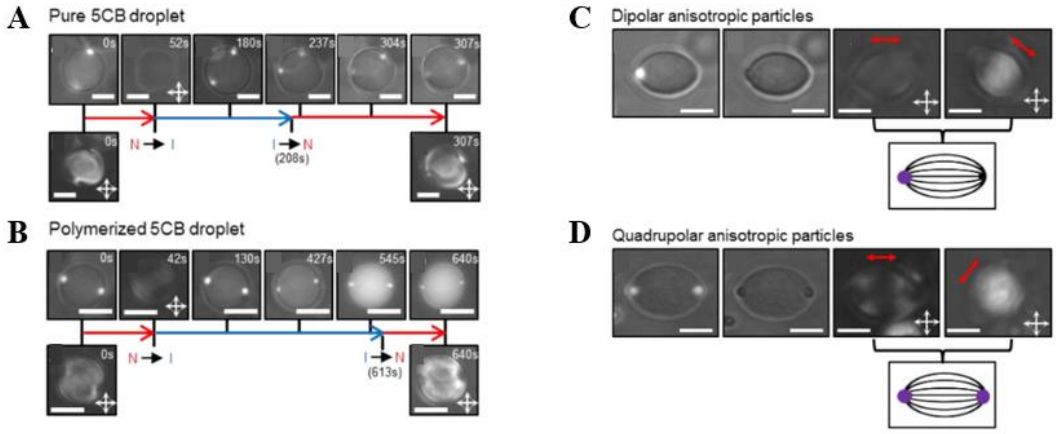

Figure 2.8 (A) Particles on the surfaces of the pure (5CB) droplets diffused toward one another after heating (isotropic phase), whereas (B) particles positioned were preserved for polymerized droplets. Typical (C) dipolar and (D) quadrupolar anisotropic particles[13].

Particle positioning on LC droplets can be tuned by an external stimulus like a magnetic field or by adsorbate-driven switching of the internal configuration of the droplet, which offers interfacial structuring. Wang et al. demonstrated that the synthesis of homogeneous populations of patchy microparticles could be achieved by using sodium dodecyl sulfate (SDS)-driven switching of the internal configurations of LC droplets to sweep colloids to a single place on the interface[51]. They initially adsorbed two microparticles (polystyrene, PS) separately to the LC droplet with bipolar configuration with two characteristic boojum defects at the poles. After introducing SDS to the system, they observed configuration changes from bipolar to preradial and simultaneously colloid movement to the one

topological defect at the interface (Figure 2.9A). After dilution of the SDS concentration and they observed reverse ordering transition (preradial to bipolar); however, they did not observe particles at LC droplets at two boojum defects of bipolar configuration. Instead, they reported LC droplets with colloids adsorbed at one of the boojums. After that, using a surfactant to change the configurations of the LC droplets makes it possible to create homogeneous populations of bipolar droplets with colloids adsorbed at a single pole. They also commented that the migration of colloids was driven by the elastic distortion of the LC induced by the colloid at the interface. They calculated the elastic forces driving the colloid to the defect in the magnitude of $E_{elastic} \sim 5 \times 10^{-18}$ J, which is close to agreement with the energy dissipated during particle movement ($E_{transport} \sim 7 \times 10^{-18}$ J) due to the drag force. Moreover, they found multiple particles located at the diametrically opposite boojums of bipolar droplets of the mixture of unreactive mesogen (5CB) and reactive mesogen (RM257). SDS-driven switching of LC droplet configuration from bipolar to preradial led to the particle replacement to the single pole of the droplet. After that, they polymerized the droplet and extracted 5CB with ethanol. They obtained spherical solid "Janus-like" microparticles with an internal polymer network oriented to preradial configuration (Figure 2.9B). In the second part, they used magnetic colloids and adsorbed to the LC droplets either bipolar or preradial configuration that was set with SDS addition. They reported that the LC droplets responded to the applied magnetic field with a uniform orientation. For instance, a preradial or bipolar LC droplet rotated in-plane 360 degrees in a clockwise direction around an axis normal to the droplets' centers. The reason for the rotation was due to the interaction between the magnetic field and LC rather than the magnetic field and LC since the applied field (10^{-4} Tesla) was smaller than the stated magnetic field in the literature (0.1-1 Tesla) that triggers the ordering transition of LC molecules. They found that the viscous forces led to the rotation of LC with applied field.

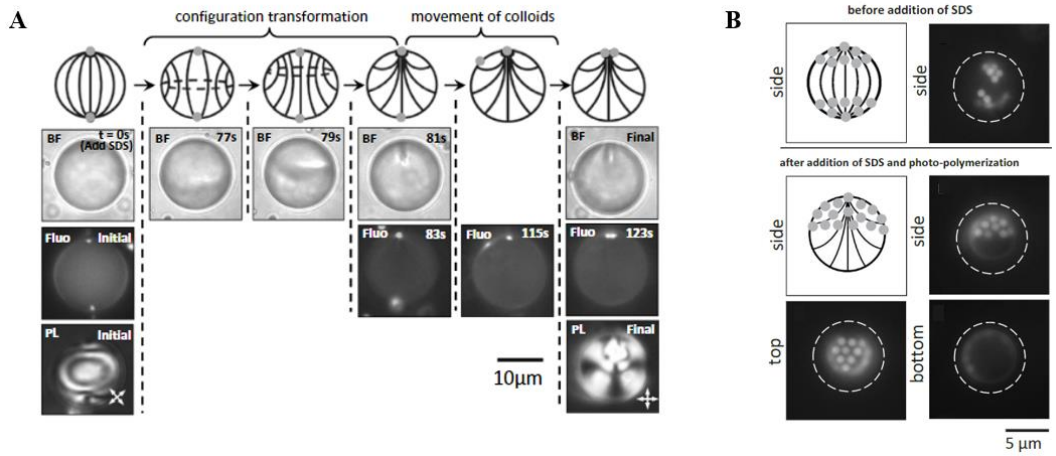

Figure 2.9 (A) Bipolar to preradial ordering transition of 5CB droplets with colloid movement, (B) Synthesis of solid "Janus-like" microparticles via switching of LC droplets ordering transition and polymerization[51].

The orientation of the nematic field affects the order of structures created by nanoparticles adsorbed at the interface of LC. Such structures were a result of a complex interaction between the orientation of the LC at the surface of the particles, the orientation at the LC-air interface, and the bulk elasticity of the underlying LC[52]. Rahimi et al. demonstrated nanoparticle self-assembly on LC droplets with a systematic study of the free energy of nanoparticle-laden LC droplets[52]. They showed that the presence of nanoparticles at the poles of the bipolar LC droplet reduces the high splay elastic energy, reducing the system's free energy. The free energy of the system was smaller when nanoparticle adsorb at the boojums compared to equator as shown in Figure 2.10A. The LC droplet exhibited a bipolar configuration with nanoparticle at the pole (Figure 2.10B). They found a critical anchoring strength for polar placement. At this point, the nematic field started to twist since anchoring strength cannot accommodate the reorientation of nematic field as shown in Figure 2.10C. Moreover, they sequentially adsorb one nanoparticle to the pole, and other one was driven to the other pole. In Figure 2.10D, the first energy minimum occurred at $\Theta=13^{o}$, corresponding to two-particle being close to each other. The second minimum ($\Theta=180^{o}$) corresponds to two particles located on opposite poles. In the central region ($\Theta<90^{o}$), another minimum observed corresponds to the

equator. Their experiments confirmed the localization of nanoparticles at the equator or poles, as their expectation (Figure 2.10E). For multiple nanoparticle adsorption, they showed that the case covering the large portion of the pole was the most stable and lowest energy state. Their model and experimental results have been shown to agree with each other.

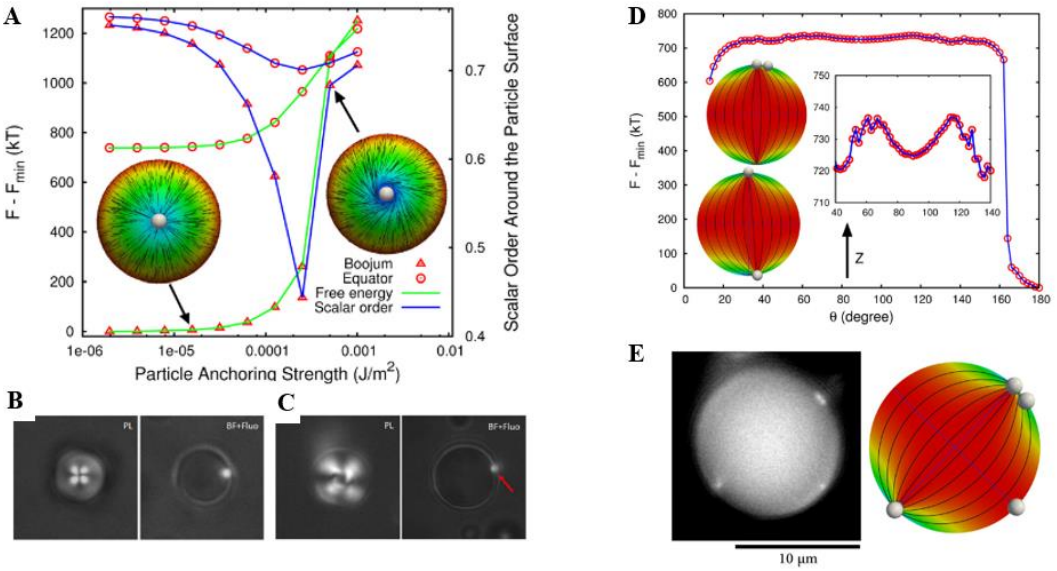

Figure 2.10 (A) Free energy of nanoparticle adsorbed at boojum and equator as a function of particle anchoring strength, insets show the top view of weak and strong anchoring (B-C) polarized light (PL), bright field (BF) and fluorescence (fluo) images of droplets with nanoparticle at boojums, (C) PL shows the twisting of nematic field near the boojum, (D) Free energy of two nanoparticles located at the poles separately, (E) Fluorescent images of the droplet with four nanoparticles and simulation of the localization of four nanoparticles that corresponds to minimum free energy[52].

LC-nanoparticle interactions may differ from LC-microparticle interactions due to the competition between elastic and surface anchoring energies, as mentioned in the Introduction part. Besides, nanoparticles are easily functionalized to obtain different surface chemistry, which offers not only different surface properties such as hydrophobicity, hydrophilicity, and charging but also proposes interparticle (or LCs-interparticle) interactions tuning without any adsorbate or triggers. Sengul et al. demonstrated that chemically modified 100 nm sized silica nanoparticles adsorption

to the LC droplet resulted in configuration change depending on the concentration of nanoparticles and surface chemistry[28]. They firstly used dimethyloctadecyl[3-(trimethoxysilyl)propyl]ammonium chloride (DMOAP) terminated silane modified nanoparticles which are well knowns to induce strong homeotropic anchoring of LCs. The resulting nanoparticles exhibited hydrophobic nature and depended on nanoparticle concentration in the medium; they obtained radial, preradial, and bipolar configurations with decreasing concentration (Figure 2.11A). They reasoned the absence of intermediate configurations (axial and escaped radial) to the chemical heterogeneity at the LC-water interface, which results in defect pinning. Below the monolayer coverage of droplets, LC droplets exhibited preradial configuration resulting from the partial coverage of the interface. The SEM images confirmed the decrease in the surface coverage with the decrease in the nanoparticle's concentration in the medium. Secondly, they used -COOH terminated silane coated nanoparticles which induce planar anchoring to the LCs with hydrophilic nature. They reported -COOH groups of weak acid provided the charging property (pH dependent) to the nanoparticles as in LC, which proposes controlled adsorption conditions via electrostatic interactions. They chose three pH values to maintain LC droplets and nanoparticles with both positive (pH=2), negative (pH=3), and both negative charges (pH=5). Even if the configuration of LC droplets did not change upon adsorption, SEM images showed that the surface coverage of LC droplets with nanoparticles depends on electrostatic interactions (Figure 2.11C). The low surface coverage was observed at pH=2 (and pH=5) since both LC droplets and nanoparticles exhibited high positive (and negative) zeta potential, resulting in repulsion force between the particle and LC droplet. However, at pH=3, the LC droplet surface was covered with a close-packed monolayer of the nanoparticles since LC droplets and nanoparticles exhibited opposite charges propose attraction force. Lastly, they used mixed monolayers of DMOAP/COOH terminated silane coated nanoparticles which induce homeotropic (or tilted) anchoring. Due to the -COOH group, this nanoparticle was pH depended on zeta potential. They have three outcomes. First, they observed that concentration depended configuration change

upon adsorption. Second, the configuration change from bipolar to preradial and radial increases with time, indicating an increase in nanoparticle adsorption (Figure 2.11B). Third, while oppositely charged LC droplets and nanoparticles offered surface coverage resulting from attraction forces, same charged LC droplets and nanoparticles lower nanoparticles' adsorption due to the repulsive forces.

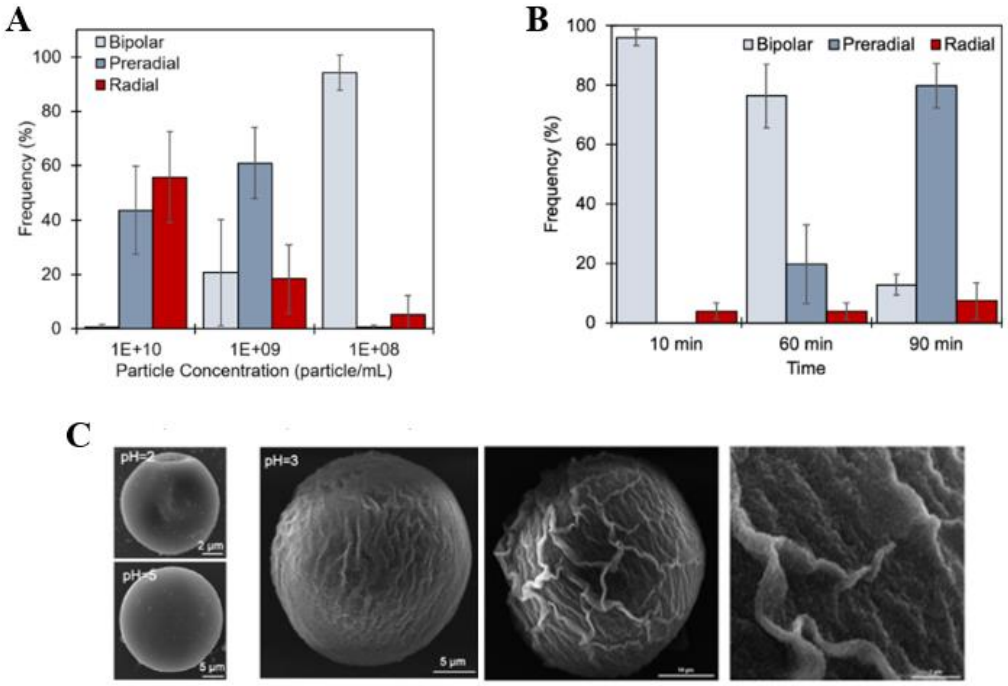

Figure 2.11 (A) Configuration distribution of LC droplets upon adsorption of DMOAP terminated nanoparticles with respect to concentration, (B) Configuration distribution of LC droplets upon adsorption of -DMOAP/COOH terminated nanoparticles with respect to time, (C) SEM micrographs of polymerized LC droplets that were exposed to -COOH terminated nanoparticles before polymerization at different pH values[28].

In the literature, there are several studies involving the interaction of LC with various molecules, micrometer, and nanometer sized particles that are mostly polymer-based (polystyrene) or ceramic-based (silica) due to easy production. However, adsorption of other types of metal-based nanoparticles that can be functionalized with thiols or mercapto derivatives offer various technological advances such as antibacterial property, susceptibility to magnetic analogue, catalytic property, conductivity, or surface plasmon resonance. Up to present, the adsorption of such nanoparticles to

the interface has not been studied in detail, and their interactions at the liquid interface should be studied. Apart from this need for elaboration, studies involving LC-nanoparticle and interparticle interactions did not exceed and detail beyond adsorbate-induce system. In these studies, the adsorption/desorption of surfactant molecules to the LC-water interface occurs, which can create different undesired thermodynamic equilibrium states in the system. Moreover, in these systems, the reordering of particles is resulted from only the ordering transition of LCs not interparticle interactions. Therefore, studies on the interactions in between nanoparticles, arises from electrostatic interactions, at LC-aqueous interface must be broadened to understand the self-assembly of the particles at the interfaces of confined elastic medium. Those future directions may make possible to reveal a synthesize method for polymer composite particles with finely tuned internal and interfacial structuring.

Herein, we offer an experimental system to carry out the adsorption of surface modified silver, iron oxide and silica nanoparticles on LC droplets and examined the configuration of LC droplet by optical to understand internal structuring. To highlight the interfacial structuring control and to understand the interparticle interaction on elastic medium, we took the advantage of surface charging property of nanoparticles and tune their surface potential by changing pH and performed the preferential repositioning of nanoparticles, which offered control over the interfacial structure. Finally, we obtained polymer composite particles templated from LC droplet with polymerization. The results serve as the knowledge for a general methodology for the synthesis of complex multifunctional polymer composite particles, which internal and interfacial structure can be pre-determined because a variety of colloidal materials can be positioned on the LC droplets using the techniques described in this thesis. Numerous possible uses for these microparticles exist, including the delivery of drugs and the self-assembly of materials.

CHAPTER 3

MATERIALS AND EXPERIMENTAL SECTION

3.1 Materials

Nematic LC mesogen, 4-cyano-4′-pentylbiphenyl (5CB), reactive monomer 4-(3-acryloyoxy-propyloxy) benzoic acid 2- methyl-1,4-phenylene ester (RM257) were purchased from Jiangsu Hecheng Chemical Materials Co., Ltd. (China). Photoinitiator, 2,2 dimethoxy-2-phenylacetophenone (DMPAP), anhydrous toluene, dimethyloctadecyl [3-(trimethoxysilyl) propyl] ammonium chloride (DMOAP), 3-Aminopropyltriethoxysilane (APTES, 99%), tetraethoxysilane (TEOS), ammonium hydroxide (25–30%), succinic anhydride, N,N-dimethylformamide (DMF), 1-decanethiol, 1-hexadecanethiol, ammonium hydroxide solution (25-30% NH_3 basis), silver nitrate, 11-mercaptoundecanoic acid (MUA, 95%), trisodium citrate dihydrate were purchased from Sigma-Aldrich (St. Louis, USA). Anhydrous ethanol, hydrogen peroxide (35%), glycerol (85%), sodium hydroxide, iron (III) chloride hexahydrate were purchased from ISOLAB (Eschau, Germany). Ethylene glycol was purchased from Merck (Darmstadt, Germany).

3.2 Synthesis of Silica Nanoparticles

100 nm of silica nanoparticles were synthesized by Stöber method[53]. Mixture of 60 mL of absolute ethanol and 3.6 mL of ammonium hydroxide were stirred for 10 min. After, 1.8 mL of TEOS was added to mixture rapidly and solution was stirred for 24 h at room temperature.

400 nm of silica nanoparticles were synthesized by following the molar ratio of TEOS:NH_3: H_2O:Ethanol = 1:2.9:53.6:58.6[54]. For approximately 47 mL mixture, 1.15 mL of ammonium hydroxide, 9.12 mL of ultrapure water and 34.21 mL of

ethanol were homogenized and 2.23 mL of TEOS was added. The final mixture was stirred at room temperature for 24 h.

50 nm of silica nanoparticles were synthesized by following the molar ratio of TEOS:Ethanol:H_2O as 5:26:9. For 86 mL of synthesis, 11.15 mL of TEOS was rapidly added to the mixture of 73.57 mL of absolute ethanol, 1.3 mL ultrapure water and 0.0237 mL ammonium hydroxide. The final mixture was stirred for 24 h at room temperature.

At the end of the silica nanoparticles synthesis, the particles were collected by centrifugation and washed with ethanol for at least four times.

3.3 Preparation of DMOAP Modified Silica Nanoparticles

DMOAP was added to the aqueous suspension of silica nanoparticles (1 vol% DMOAP) and kept in ultrasonic bath for 20 min[28]. The DMOAP modified silica nanoparticles were collected via centrifugation (10000 rpm, 15 min), supernatant was replaced with ultrapure water and particles were redispersed in ultrapure water by using vortex and ultrasonic bath. The washing step with ultrapure water was repeated (at least ten times) until unreacted DMOAP molecules were removed from the medium. To ensure the removal of unreacted DMOAP molecules from medium, LC-in-water emulsions were prepared in final supernatant and checked with cross polarized light microscopy to maintain bipolar configuration expected in the aqueous supernatant free of DMOAP.

3.4 Preparation of Amine (-NH_2) Terminated Silane Groups Modified Silica Nanoparticles

Silica nanoparticles were functionalized with amine-terminated groups by adding 0.138 mL APTES to the 25 mL of silica nanoparticles in ethanol and stirred overnight. Then, amine-terminated nanoparticles were separated with centrifugation

(10000 rpm, 15 min), supernatant was replaced with ethanol at least four times, and nanoparticles were redispersed in water[28].

3.5 Preparation of Carboxylic Acid (-COOH) Terminated Silane Groups Modified Silica Nanoparticles

Silica nanoparticles in aqueous medium were first modified with amine-terminated groups by adding 0.138 mL APTES to the 25 mL of silica nanoparticles in ethanol and stirred overnight[28]. Then, amine-terminated nanoparticles were separated with centrifugation (10000 rpm, 15 min), supernatant was replaced with ethanol at least four times, and nanoparticles were redispersed in DMF. 20 mL of final solution was added dropwise into 20 mL of 0.1 M succinic anhydride DMF solution. The final mixture was stirred for 24 h at room temperature. The final carboxylic acid terminated silica nanoparticles were rinsed with DMF and water for three times for each medium.

3.6 Preparation of Mixed Monolayer of DMOAP and -COOH Terminated Silane Groups Modified Silica Nanoparticles

20 mg of silica nanoparticles were dispersed in 1 mL of ethanol and sonicated until clear solution was obtained. Dispersed silica nanoparticles were added to the mixture of 19 mL of ethanol, 1 mL of APTES and 200 μL of DMOAP. The solution was stirred for 1 h at 80ºC. Then, mixture was cooled down to room temperature and washed with ethanol three times and redispersed in DMF. 20 mL of this solution was added dropwise to the flask containing 20 mL of 0.1 M succinic anhydride in DMF. The mixture was stirred at room temperature for 24 h. Mixed monolayer terminated silica nanoparticles were rinsed with DMF and water for three times[28].

3.7 Synthesis of Magnetic Nanoparticles

Magnetic nanoparticles were synthesized by using modified solvothermal method[55]. Iron (III) chloride hexahydrate was used for iron source and trisodium citrate as a stabilizer in ethylene glycol solution. Typically, 0.72 grams of trisodium citrate, and 3.60 grams of sodium acetate were dissolved in 60 mL of ethylene glycol. Then, 3.25 grams of iron (III) chloride hexahydrate were added, and mixture was stirred until a clear solution was obtained. After, the solution was distributed into two 30-mL Teflon-sealed autoclaves and solvothermally treated at 200°C for 10 h. The resulting black products were cooled to room temperature and washed with ethanol and ultrapure water at least three times. During the washing steps, particles were collected by magnet.

3.8 Synthesis of Silver Nanoparticles

Silver nanoparticles (approximately 20 nm) were synthesized with modified Lee and Meisel method[56]. A 50 mL glycerol and water mixture (40 vol% glycerol) were stirred in water bath and heated up to 95ºC. After desired inner temperature was reached 9 mg silver nitrate and 1 min later 1 mL of sodium citrate (3%) were added. The mixture was stirred at 95ºC for 1h. The color change was observed from yellow to brown. The nanoparticles were collected by centrifugation and washed with glycerol and ultrapure water at least 3 times for each medium.

3.9 Preparation of 1-Decanethiol (-C10) Terminated Silver Nanoparticles

4 mL of silver nanoparticles in water were mixed with 16 mL of ethanol. 17 μL 1-decanethiol (4 mM thiol concentration) was added to mixture and waited overnight. The 1-decanethiol terminated silver nanoparticles were collected by centrifugation and rinsed with ethanol and water for three times (7500 rpm, 30 min).

3.10 Preparation of Mixed Monolayer of 1-Decanethiol (-C10) and 1-Hexadecanethiol (-C16) Terminated Silver and Magnetic Nanoparticles

Silver and magnetic nanoparticles were terminated with -C10 and -C16 groups. Total thiol concentration was 4 mM where 1-decanethiol and 1-hexadecanethiol ratio was 4:1[57]. For 20 mL solution, 16 mL ethanol were mixed with 4 mL of silver or magnetic nanoparticles in water and then 13.5 μL of 1-decanethiol and 2.3 μL of 1-hexadecanethiol were added to the mixture and waited overnight at room temperature. The particles were rinsed with ethanol and water for three times and particles were collected via centrifugation (7500 rpm, 30 min).

3.11 Preparation of Mixed Monolayer of MUA (-COOH) and 1-Hexadecanethiol (-C16) Terminated Thiols Modified Silver and Magnetic Nanoparticles

Silver and magnetic nanoparticles were terminated with the same method[57]. Total thiol concentration was arranged as 4 mM where MUA and 1-hexadecanethiol ratio was 4:1, 1:1, or 1:4. For 20 mL solution and 4:1 ratio of thiol and mercapto derivatives, 16 mL ethanol were mixed with aqueous suspensions of 4 mL of silver or magnetic nanoparticles and 14 mg of MUA and 4.9 μL of 1-hexadecanethiol were homogenized in the mixture. The solution was waited overnight and rinsed with ethanol and water for three times.

3.12 Preparation of LC Droplets in Water and Nanoparticles Adsorption on LC Droplets

LC emulsions in water were prepared by adding 3 μL of 5CB to the 1 mL of aqueous suspensions of either functionalized silica, silver, or magnetic nanoparticles. The mixture was mixed with vortex for 30-45 s at 3000 rpm and waited until desired adsorption occurred.

3.13 Sequential Nanoparticles Adsorption

LC droplets were prepared by adding 3 μL of 5CB to the water containing desired concentration of -NH_2 terminated silica nanoparticles. After the time required for adsorption has elapsed, the supernatant of liquid crystal droplets that naturally sediment replaced with water at least three times to prevent additional adsorption to the droplets. Then, -COOH terminated silica nanoparticles with a desired concentration were added to the LC droplets medium and equilibrated time required for adsorption.

3.14 Changing the pH of Medium After Nanoparticles Adsorption

After adsorption of nanoparticles, LC droplets were waited to sediment naturally and the 800 μL supernatant were replaced with desired a pH medium (for acidic pH HCl (1M) and for basic pH NaOH (1M) were used). The process was repeated until the pH of the medium was changed.

3.15 Preparation of Polymerized LC Droplets

For preparation of polymerizable LC droplets, a mixture of reactive monomer (RM257) and unreactive 5CB LC mesogens were used. Photoinitiator was used to UV-polymerization. The composition of the LC was held constant in the studies where the mass ratio was 25 wt% RM257, 75 wt% 5CB and 1 wt% photoinitiator. The mixture of RM257, 5CB and photoinitiator were homogenized with toluene using and obtained transparent mixture. Then, toluene was evaporated for overnight and obtained milky white mixture. To prepared LC droplets, 3 μL of RM257-5CB mixture were mixed with 1 mL of aqueous suspensions of either surface modified silver, silica, or magnetic nanoparticles by using vortex for 7-10 min at 3000 rpm. LC droplets were polymerized under 365 nm of UV light for 20 min. After curing, polymerized LC droplets were rinsed with water to ensure that additional adsorption

was not occur. Then, unreacted 5CB were extracted from the polymerized LC droplets by using a solvent (ethanol). During the rinsing step with water and ethanol, polymerized LC droplets were sediment naturally and supernatant was changed with fresh water or ethanol.

3.16 Sample Preparation for Optical Characterization

Two spacers were placed on opposite edges of a glass slide and 80 μL of the LC-in-water emulsion sample (Chapter 3.12) was placed in the middle of the glass slide. After that, the top of the system was covered with a glass slide.

3.17 Sample Preparation for Scanning Electron Microscope (SEM)

After preparation of polymerized LC droplets (Chapter 3.15), the polymerized LC droplets were dispersed in ethanol. The sample was dripped to glass slide (1 x 1 cm). The glass slide was positioned on SEM holder and waited until ethanol evaporated.

3.18 Optical Characterization of LC Droplets and Size Analysis

After sample preparation for optical characterization (Chapter 3.16), optical characterizations were obtained using cross polarized optical microscope (Olympus, BX50 Model) and bright field/polarized optical micrographs were collected with 50x objective. LC droplet size analysis were done by Fiji, ImageJ.

3.19 Characterization of Nanoparticles and LC Droplets

The analysis of size, concentration and zeta potential of nanoparticles were performed by using Dynamic Light Scattering and Zetasizer Ultra (Malvern Instruments Ltd., US). The morphology of polymerized LC droplets was examined by Scanning Electron Microscope (SEM, QUANTA 400F Field Emissions). The

morphology of nanoparticles was examined by X-Ray Diffraction Analysis (XRD, Rigaku Miniflex 600). XRD analysis was done with 2Ɵ angles ranging from 10º to 80º degree with 0.02 step and 2/min rate.

3.20 Zeta Potential Measurements of Nanoparticles

The nanoparticles were dispersed in water with different pH ranging between 2-10. Zeta potential measurements were carried out using Zetasizer Ultra (Malvern Instruments Ltd., US).

3.21 Zeta Potential Measurements of LC Droplets

A stock solution of LC droplets was prepared by emulsifying 10 μL of 5CB in 1 mL water using tip sonicator (AM:60%, 60 s). Then 9 mL of stock solution of 5CB droplets was dispersed in 1 mL of water at desired pH values (for acidic pH HCl (1M) and for basic pH NaOH (1M) were used). The zeta potential values were measured within 2 hours. pH changing of 5CB droplets to a desired pH, 700 μL of 5CB containing medium was replaced with desired pH and zeta potential was measured within 2 hours.

CHAPTER 4

RESULTS AND DISCUSSION

This thesis work has two main parts. The first part is the synthesis and surface modifications of silver nanoparticles (Ag NPs), magnetic iron oxide nanoparticles (IONPs), and silica nanoparticles (Si NPs) and their characterizations. The second part is the adsorption of surface-modified nanoparticles onto LC droplets/water interface, determining the configuration of LC droplets and controlling the interfacial structure of surface-modified nanoparticles that are adsorbed on LC droplets. Figure 4.1 shows the schematic illustration of the work that was followed in this work.

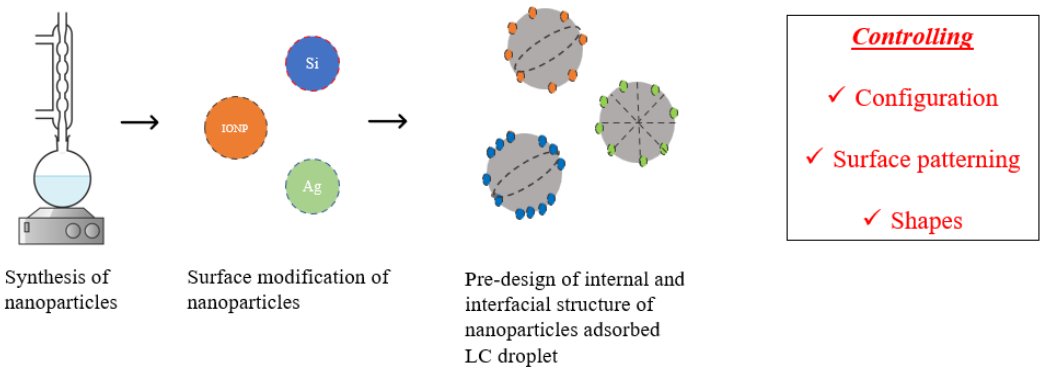

Figure 4.1 Schematic illustration of the steps that followed in this thesis work

4.1 Characterization of Nanoparticles

We synthesized three different sizes of silica nanoparticles by using Stöber method[53,54,58]. We aimed to obtain small, medium, and large sizes of silica nanoparticles (Si NPs). The hydrodynamic diameters of bare silica nanoparticles were measured as 51.2 nm ± 9.0 nm, 87.5 nm ± 7.2 nm, and 417.1 nm ± 22.1 nm using dynamic light scattering (DLS) (Figure 4.2A-C). Sizes measured from scanning electron microscopes (SEM) micrographs were 62.5 nm ± 9.6 nm, 102.6

nm ± 11.5 nm, and 387.5 nm ± 24.3 nm (Figure 4.2D-F), which consistent with the average sizes on bare silica nanoparticles measured from the DLS.

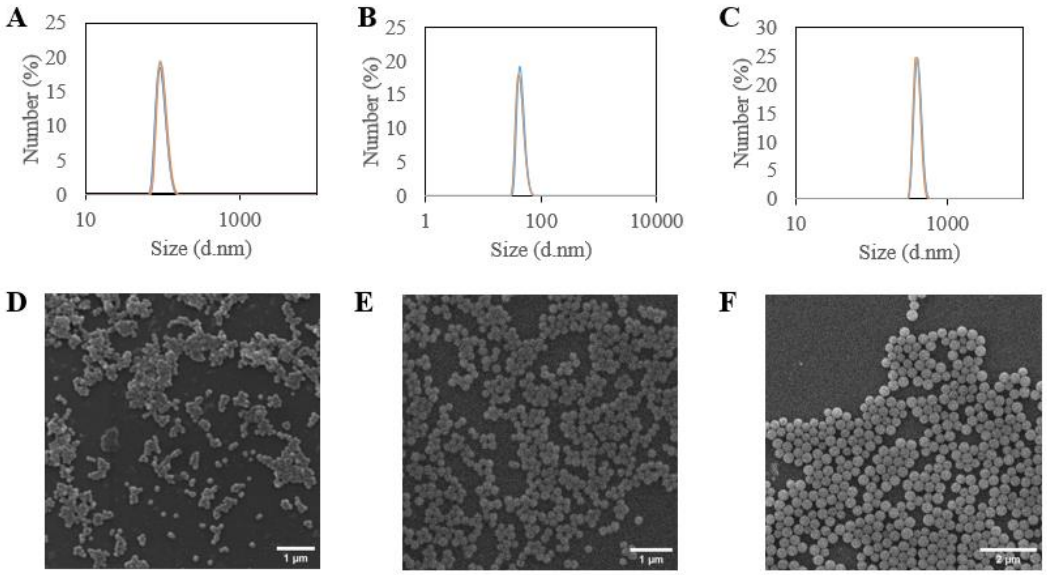

Figure 4.2 Size characterization of silica nanoparticles. (A-C) size distribution of small (51.2 nm ± 9.0 nm), medium (87.5 nm ± 7.2 nm) and large (417.1 nm ± 22.1 nm) sizes of bare silica nanoparticles obtained from DLS, (D-F) SEM micrographs of small (62.5 nm ± 9.6 nm), medium (102.6 nm ± 11.5 nm) and large (387.5 nm ± 24.3 nm) sizes of bare silica nanoparticles.

After synthesis of silica nanoparticles, we modified their surfaces with silanes by using either DMOAP, -COOH, their mixed monolayers of -COOH and DMOAP terminated silanes or -NH_2 terminated silane groups. With those surface modifications, we obtained different surface properties (hydrophobic, hydrophilic, charging), and anchoring conditions for LC droplets (homeotropic, planar or tilted)[28,59].

The first surface modification was done with DMOAP which are known to change LC anchoring condition to homeotropic[60]. After surface modification with DMOAP, 87.5 nm ± 7.2 nm-average-sized bare silica nanoparticles (Bare Si) procure hydrophobic nature due to the long hydrocarbon tail of DMOAP. The DMOAP-modified silica nanoparticles (Si-DMOAP) sizes were measured as 138 nm ± 14 nm with DLS (Figure 4.3A). After modification, the surface charge of silica

nanoparticles was changed, and zeta potential was measured as 49.9 mV ± 5.8 mV (Figure 4.3B). Finally, concentration of aqueous suspensions of DMOAP-modified silica nanoparticles were measured to be in the order of 10^{10} particles/mL (Figure 4.3C).

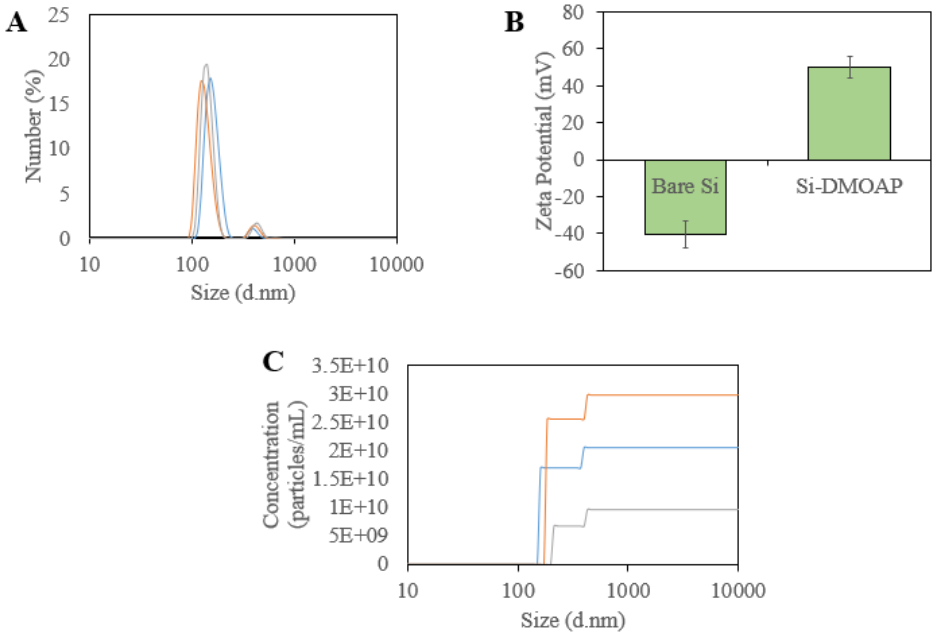

Figure 4.3 Characterization of DMOAP-modified silica nanoparticles. (A) Size distribution of DMOAP-modified silica nanoparticles obtained from DLS, (B) zeta potential measurements for bare and DMOAP-modified silica nanoparticles in pure water, (C) particle concentration measurement of aqueous suspensions of DMOAP-modified silica nanoparticles. For the DMOAP modification, medium size silica nanoparticles (87.5 nm ± 7.2 nm) were used.

The second and third surface modification was done with amine and carboxyl terminated silane molecules. Amine and carboxyl groups provide pH-dependent charging to silica nanoparticles and hydrophilic nature. The amine termination was carried out with the treatment of APTES, and we obtained -NH_2 groups on the surface of silica nanoparticles. To maintain carboxyl groups on the surface of silica nanoparticles, we introduced a succinic anhydrate treatment, so a ring opening linker elongation reaction of the -NH_2 terminated silane group occurred, and -COOH terminated silane groups are formed[59]. The 87.5 nm ± 7.2 nm-average-sized bare silica nanoparticles (Bare Si) with single monolayer of the -NH_2 and -COOH

terminated silane groups were measured as 139 nm ± 42 nm and 120 nm ± 4 nm, respectively (Figure 4.4A). The silica nanoparticles functionalized with single monolayer of -NH_2 (Si-NH_2) and -COOH (Si-COOH) terminated group were of similar sizes because the additional carboxylic group did not increase the sizes of nanoparticles[59]. Due to the lower surface charge, the nanoparticles functionalized with -NH_2 terminated group tended to aggregate more than nanoparticles with -COOH terminated group in a short time. The literature stated that they are more hydrophobic than -COOH terminated silica nanoparticles[59]. These agglomerates can be realized from the size increase after the surface modification (Figure 4.4A). To confirm the surface modification, we measured the zeta potentials of surface-modified silica nanoparticles. The aqueous suspensions of bare silica nanoparticles' zeta potential were measured as -40.5 mV ± 7.5 mV, and after surface modification, we expected to observe zeta potential change (Figure 4.4B). The zeta potential of aqueous suspensions of single monolayer of -NH_2 and -COOH terminated groups functionalized silica nanoparticles were measured as 27.8 mV ± 3.7 mV and -31.4 mV ± 5.8 mV, respectively, changes confirmed the surface modification (Figure 4.4B). The concentration of aqueous suspensions of nanoparticles was measured as 10^{10} particles per mL (Figure 4.4D-E).

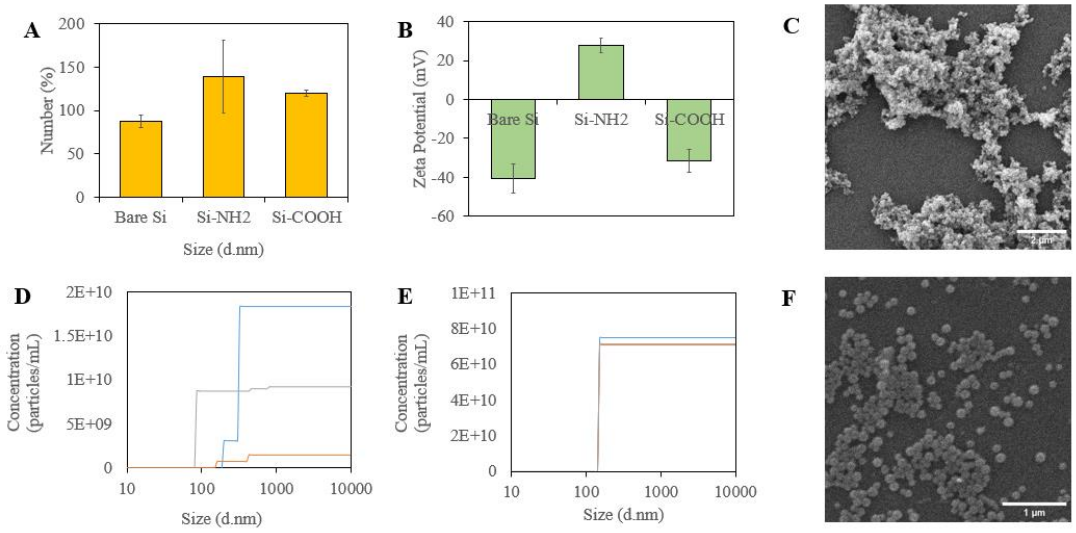

Figure 4.4 Characterizations of single monolayer of -NH_2 and -COOH terminated silica nanoparticles. (A) Size distributions of bare, single monolayer of -NH_2 and -COOH terminated silica nanoparticles, (B) zeta potential measurements of aqueous suspensions of bare, single monolayer of -NH_2 and -COOH terminated silica nanoparticles, (C) SEM micrographs of -NH_2 terminated silica nanoparticles, (D-E) concentration measurements of single monolayer of -NH_2 and -COOH terminated silica nanoparticles in pure water, respectively, (F) SEM micrographs of -COOH terminated silica nanoparticles. For the surface modification, medium size silica nanoparticles (87.5 nm ± 7.2 nm) were used.

The fourth surface modification was obtained using the combination of -COOH terminated silane group and DMOAP, and we obtained their mixed monolayer surface termination[28]. We aimed to maintain a nanoparticle surface with pH-dependent charging, and LC droplet responses upon adsorption of the nanoparticles with mixed monolayers of DMOAP and -COOH terminated silane groups (-COOH/DMOAP mixed monolayer terminated silica nanoparticles (Si-COOH/DMOAP)). The size of the -COOH/DMOAP mixed monolayer terminated silica nanoparticles was measured as 122.3 nm ± 25 nm with DLS (Figure 4.5A). To obtain -COOH/DMOAP mixed monolayer terminated silica nanoparticles, firstly, we exposed silica nanoparticles to APTES (-NH_2 terminated silane molecule) and DMOAP. The zeta potential of 87.5 nm ± 7.2 nm-average-sized bare silica nanoparticles changed from -40.5 mV ± 7.5 mV to +42 mv after -NH_2/DMOAP mixed monolayer termination (Si-NH_2/DMOAP). As described before, we used

succinic anhydrate to obtain -COOH groups. After introducing succinic anhydrate, the zeta potential of -NH_2/DMOAP mixed monolayer terminated silica nanoparticles changed from +42 mV to -11.2 mV ± 3.8 mV (Figure 4.5B). Our zeta potential measurements confirmed -COOH/DMOAP monolayer termination. At the end of the modification procedure with mixed monolayers of DMOAP and -COOH terminated silanes, the concentration of aqueous suspensions of silica nanoparticles was measured to be in the order of 10^{10} particles/mL (Figure 4.5C).

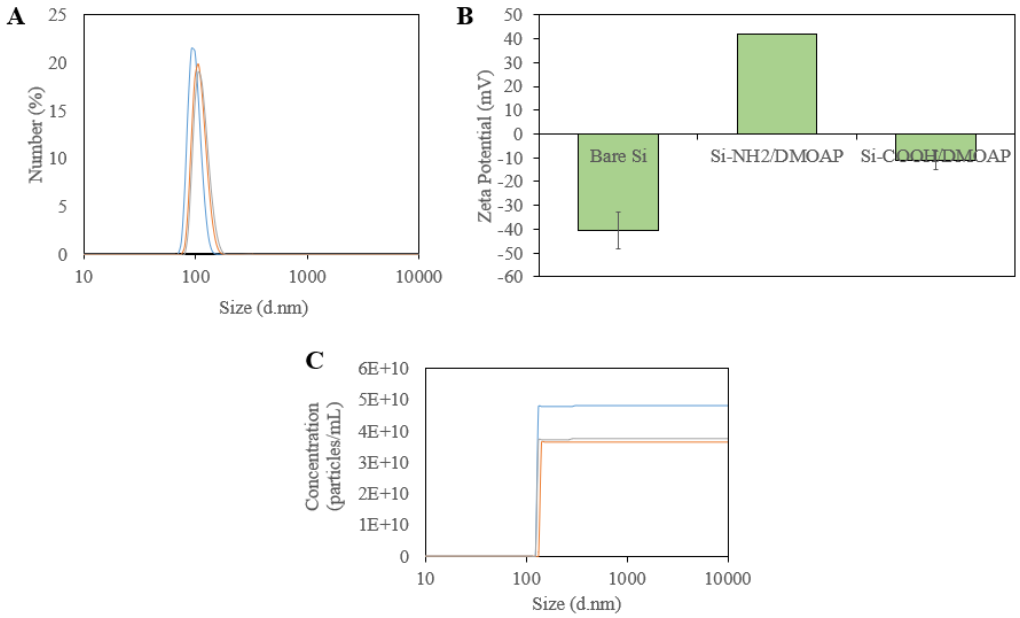

Figure 4.5 Characterization of surface modified silica nanoparticles with mixed monolayer of -COOH and DMOAP terminated silanes. (A) Size distribution of silica nanoparticles with mixed monolayer of -COOH and DMOAP terminated silanes obtained from DLS, (B) zeta potential measurements of bare nanoparticles, surface modified silica nanoparticles with mixed monolayer of -NH_2 and DMOAP terminated silanes, and surface modified silica nanoparticles with mixed monolayer of -COOH and DMOAP terminated silanes in pure water, (C) particle concentration measurement of aqueous suspensions of silica nanoparticles with mixed monolayer of -COOH and DMOAP terminated silanes. For the -COOH and DMOAP mixed monolayer termination, medium size silica nanoparticles (87.5 nm ± 7.2 nm) were used.

We performed surface modification to the 51.2 nm ± 9.0 nm, and 417.1 nm ± 22.1 nm-average-sized bare silica nanoparticles with single monolayer of -NH_2 and -COOH terminated silane groups. The size was measured as 524 nm ± 90.2 nm for -

NH_2 terminated silica nanoparticles, where the initial size was 417.1 nm ± 22.1 nm (Figure 4.6A). After termination with the -NH_2 groups to 417.1 nm ± 22.2 nm-average-sized bare silica nanoparticles, the zeta potential of the bare silica was changed from -49.9 mV ± 8.9 mV to 18.7 mV ± 9.7 mV (Figure 4.6B). For 51.2 nm ± 9.0 nm-average-sized bare silica nanoparticles, we used -COOH termination, measured size and zeta potential. Due to the aggregation, the size was measured as 114.1 nm after -COOH termination (Figure 4.6D). The bare silica nanoparticles' zeta potential changed from -51.7 mV ± 11.5 mV to -26.3 mV (Figure 4.6E). The concentration of surface modified silica nanoparticles was measured to be the order of 10^9 particles per mL (Figure 4.6C and Figure 4.6F).

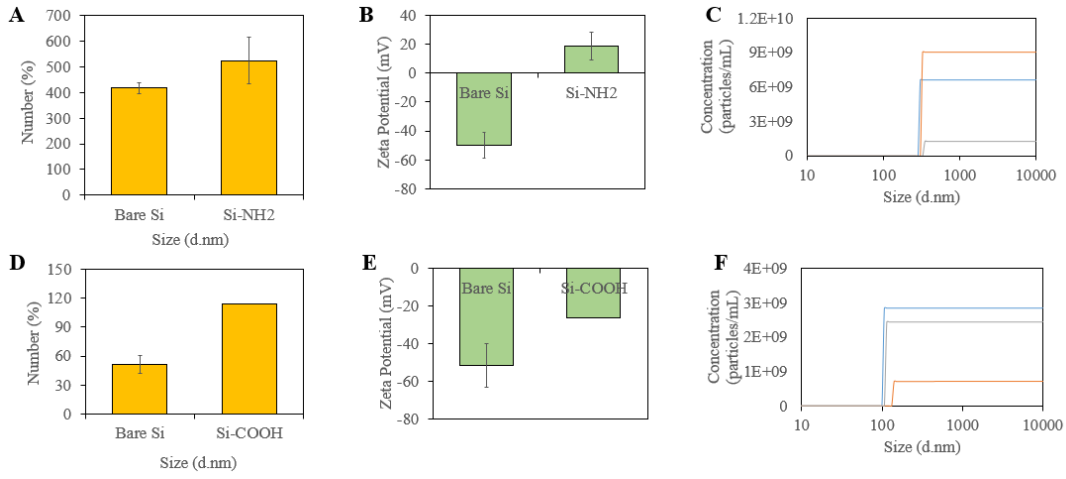

Figure 4.6 Characterizations of surface-modified 51.2 nm ± 9.0 nm and 417.1 nm ± 22.1 nm-average-sized silica nanoparticles. (A) size measurements of 417.1 nm ± 22.1 nm-average-sized bare and -NH_2 terminated silica nanoparticles, (B) zeta potential measurements of aqueous suspensions of 417.1 nm ± 22.1 nm-average-sized bare and -NH_2 terminated silica nanoparticles, (C) particle concentration measurements of -NH_2 terminated silica nanoparticles in pure water, (D) size measurements of 51.2 nm ± 9.0 nm-average-sized bare and -COOH terminated silica nanoparticles, (E) zeta potential measurements of aqueous suspensions of 51.2 nm ± 9.0 nm-average-sized bare and -COOH terminated silica nanoparticles, (F) particle concentration measurements for -COOH terminated silica nanoparticles in pure water.

Zeta potential of surface-modified silica nanoparticles with -COOH, DMOAP, mixed monolayer of -COOH and DMOAP, and -NH_2 terminated silane groups with different sizes of silica nanoparticles were summarized in Table 1.

Table 1 Zeta potential measurements of surface-modified silica nanoparticles (Si NPs) according to bare silica nanoparticles sizes.

	Zeta potential		
	Size of bare Si Nanoparticles (NPs)		
Types of Si NPs	**51.2 nm ± 9.0 nm**	**87.5 nm ± 7.2 nm**	**417.1 nm ± 22.1 nm**
Bare Si NPs	-51.7 mV ± 11.5 mV	-40.5 mV ± 7.5 mV	-49.9 mV ± 8.9 mV
Si-COOH NPs	-26.3 mV	-31.4 mV ± 5.8 mV	
Si-DMOAP NPs		49.9 mV ± 5.8 mV	
Si-COOH/DMOAP NPs		-11.2 mV ± 3.8 mV	
Si-NH_2 NPs		27.8 mV ± 3.7 mV	18.7 mV ± 9.7 mV

Besides silica nanoparticles, we synthesized silver nanoparticles (Ag NPs) and magnetic iron oxide nanoparticles (IONPs)[55,56]. For the characterization of sizes of bare silver nanoparticles, we used DLS and measured 15.7 nm ± 1.9 nm (Figure 4.7A). We did energy dispersive X-Ray (EDX) elemental analysis to confirm the silver nanoparticles, and elemental mapping results indicated the distribution of silver and oxygen elements (Figure 4.7B).

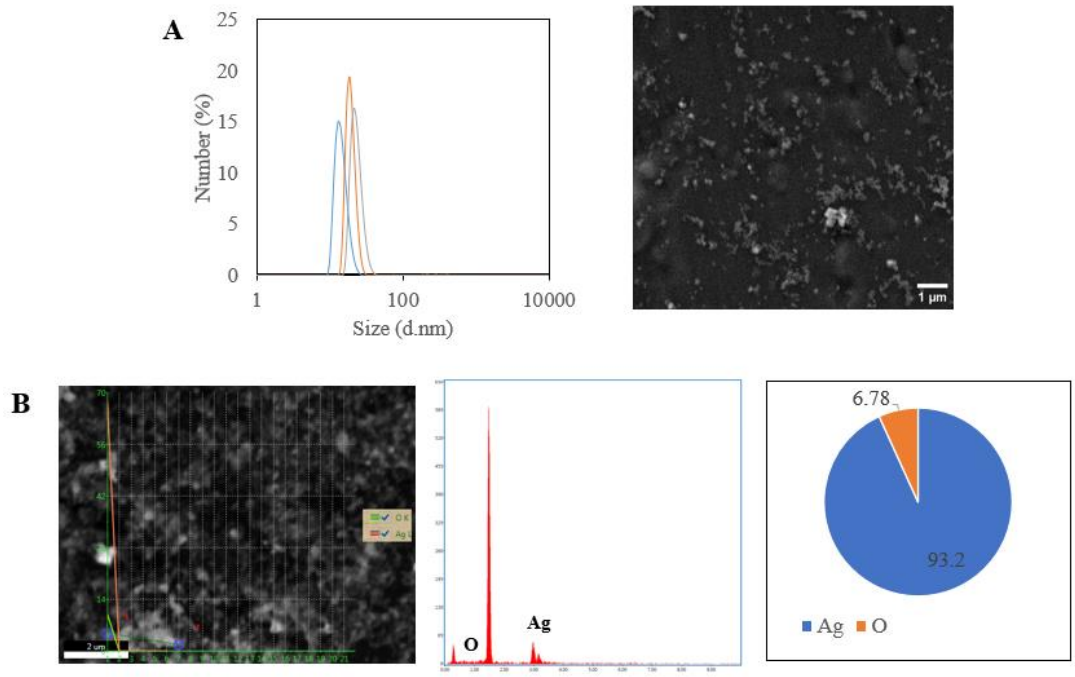

Figure 4.7 Characterizations of silver nanoparticles. (A) size distribution of bare silver nanoparticles and SEM micrographs, (B) EDX elemental analysis spectrum for silver nanoparticles.

The size of iron oxide nanoparticles (IONPs) was measured as 544.7 nm ± 42.9 nm with DLS, which consisted of 672 nm ± 72 nm obtained from SEM micrograph (Figure 4.8A-B). The difference between DLS and SEM micrographs resulted from the principle of underlaying the applied methods. For the SEM imaging, we used dry and diluted samples that may not reflect the particle distribution in the aqueous suspension, but the DLS technique aqueous suspensions were used for measurements. We used vibrating sample magnetometer (VSM) to measure the magnetic properties of IONPs as a function of magnetic field and obtained the magnetization versus magnetic field curves. The IONPs did not show hysteresis, which indicated superparamagnetic properties[61]. The saturation magnetization of nanoparticles was measured 41.1 emu/g (Figure 4.8D). The X-Ray diffraction analysis (XRD) patterns were collected. The peaks of IONPs with the maximum intensity were at approximately 30º and 35º, indicating the magnetite phase of iron oxide nanoparticles. Also, the third and fourth peak was observed at approximately

65º and 70º, which could be the reflection of magnetite phase[61,62] (Figure 4.8E). The remaining peaks could be due to the other phases, such as maghemite in the samples[62].

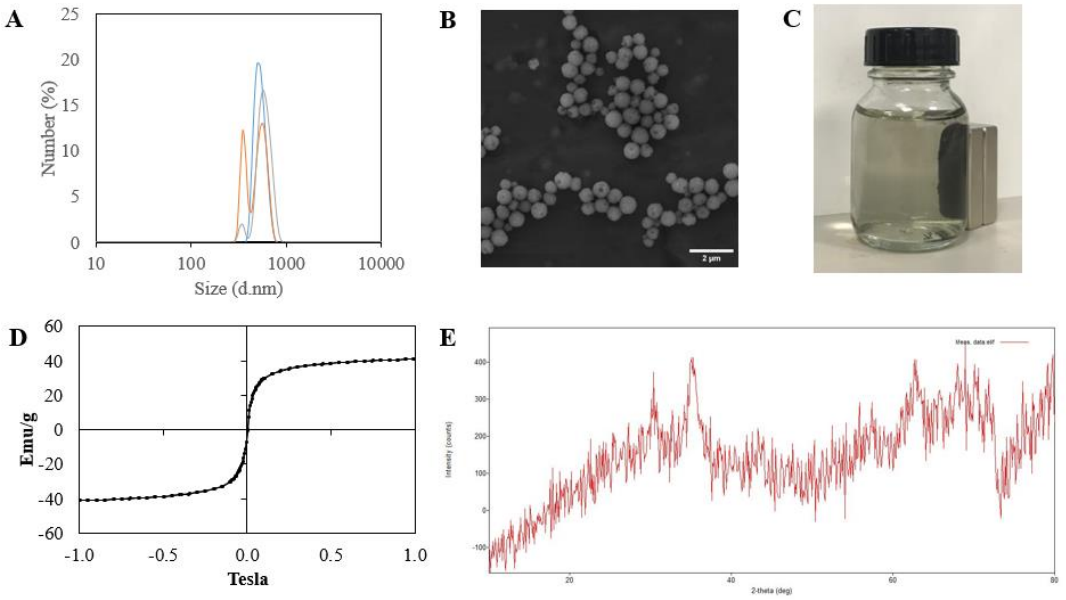

Figure 4.8 Characterizations of iron oxide nanoparticles (IONPs). (A) Size distribution of IONPs obtained from DLS, (B) SEM micrographs of IONPs, (C) collection of IONPs with magnet, (D) magnetization property of IONPs against the applied magnetic field, (E) XRD patterns of iron oxide nanoparticles.

The surface of silver nanoparticles (Ag NPs) and iron oxide nanoparticles (IONPs) were modified using either single monolayer of 1-decanethiol (-C10), and a mixed monolayer of 1-decanethiol and 1-hexadecanethiol (-C16) terminated thiol groups (-C10/C16 mixed monolayer). While 1-decanethiol has 10 hydrocarbon tails, 1-hexadecanethiol has 16 hydrocarbon tails. Firstly, the surface of silver nanoparticles was modified with single monolayer of -C10 terminated thiol group (Ag-C10). After modification of the surface, we measured the zeta potential of -C10 terminated silver nanoparticles in an aqueous medium, and the zeta potential of bare silver nanoparticles changed from -27.2 mV ± 5.3 mV to -21.8 mV ± 4.4 mV (Figure 4.9A). The surface modification of silver nanoparticles with -C10/C16 mixed monolayer (Ag-C10/C16) caused to change in the zeta potential of bare silver nanoparticles to -4.0 mV ± 4.8 mV (Figure 4.9A). Also, we noted that heterogeneity on the surface

modification, long hydrocarbon tail and thiols[63–67] increased the hydrophobicity and resulted in the accumulation of -C10/C16 mixed monolayer terminated silver nanoparticles on the water-air interface (Figure 4.9A intext picture). Similarly, we used surface modification with -C10/C16 mixed monolayer for IONPs (IONP-C10/C16) with different C10:C16 ratios (4:1 or 1:4). Zeta potential of bare IONPs changed from -31.2 mV ± 0.7 mV to -21.2 mV ± 3.9 mV and -24.7 mV ± 2.0 mV for 4:1 and 1:4 thiols ratio, respectively (Figure 4.9B). After surface modifications, concentrations of the suspended nanoparticles in an aqueous solution were measured and found to be in the range of 10^6 to 10^{12} particles per mL (Figure 4.9C-E).

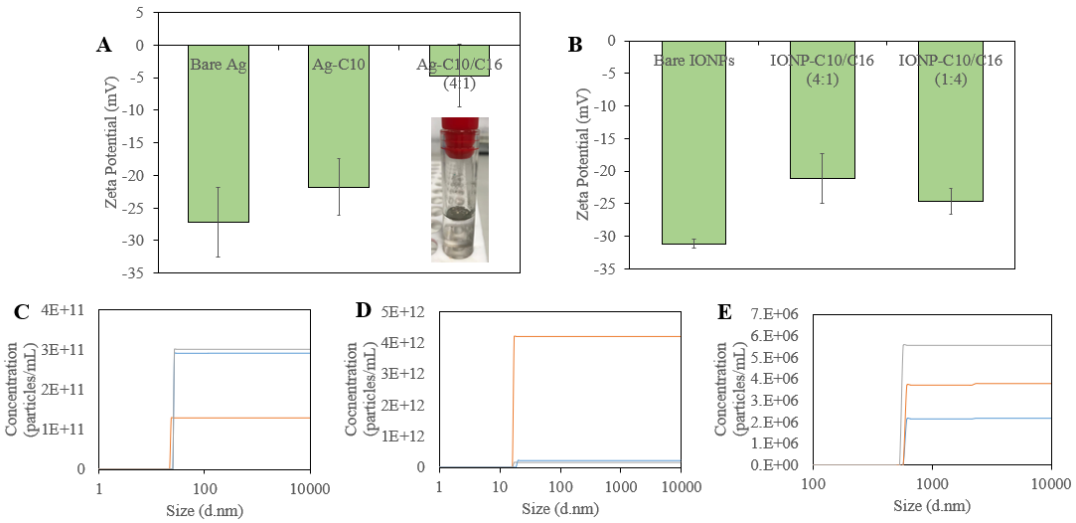

Figure 4.9 Characterizations of surface-modified silver and IONPs. (A) zeta potential measurements of bare, single monolayer of -C10 terminated, and -C10/C16 mixed monolayers terminated silver nanoparticles, intext picture shows hydrophobic nature of -C10/C16 mixed monolayer terminated silver nanoparticles, (B) zeta potential measurements of bare, and -C10/C16 mixed monolayer terminated IONPs, (C-E) particle concentration measurements of -C10 terminated silver nanoparticles, -C10/C16 mixed monolayer terminated silver nanoparticles, and -C10/C16 mixed monolayer terminated IONPs, respectively.

Finally, we used mixed monolayer of 11-mercaptoundecanoic acid (-COOH) and 1-hexadecanethiol (-C16) terminated thiols groups (-COOH/C16 mixed monolayer) with different -COOH:C16 ratios (4:1 or 1:1) for silver and iron oxide nanoparticles. The zeta potential of bare silver nanoparticles changed from -27.2 mV ± 5.3 mV to -23.5 mV ± 6.1 mV and -24.9 mV ± 8.7 mV for 4:1 and 1:1 thiol ratio, respectively

(Figure 4.10A) after surface modification. Similarly, the zeta potential of surface-modified IONPs was measured as -16.3 mV ± 7.8 mV and -24.4 mV ± 8.2 mV for -COOH:C16 ratios are 4:1 or 1:4, respectively (Figure 4.10B). After surface modification, the concentration of aqueous suspensions was measured to be in the order of 10^6 - 10^9 particles per mL (Figure 4.10C-D).

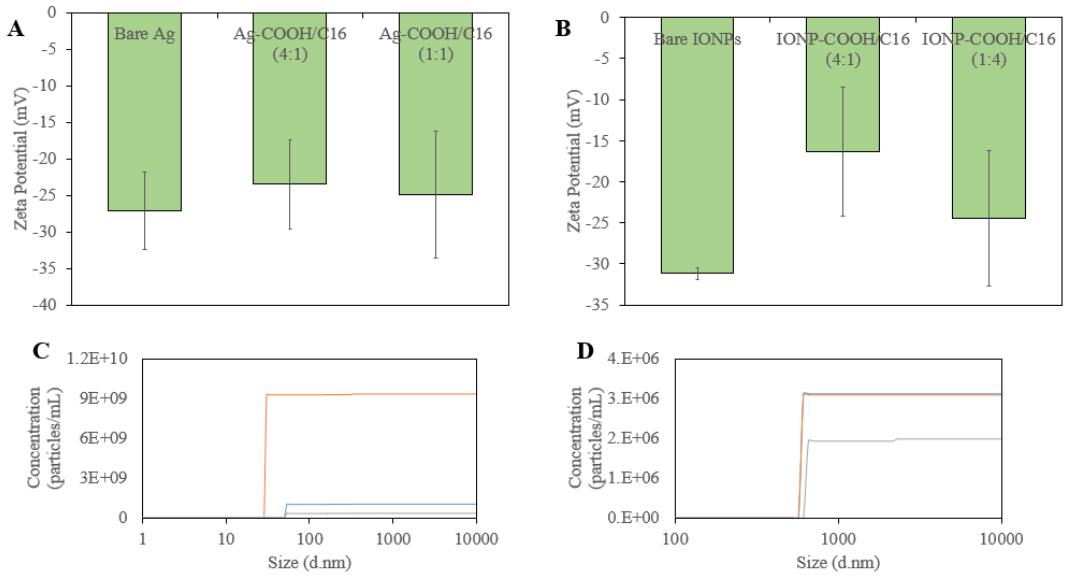

Figure 4.10 Characterizations of mixed monolayer of 11-mercaptoundecanoic acid (-COOH) and 1-hexadecanethiol (-C16) terminated thiols groups (-COOH/C16 monolayer) functionalized silver and IONPs. (A) zeta potential measurements of bare, -COOH/C16 mixed monolayer terminated silver nanoparticles for ratios of -COOH:C16 is 4:1 or 1:1, (B) zeta potential measurements of bare, -COOH/C16 mixed monolayer terminated IONPs for ratios of -COOH:C16 is 4:1 or 1:4, (C-E) particle concentration measurements of -COOH/C16 mixed monolayer terminated silver and IONPs.

4.2 Internal and Interfacial Structuring of Surface-Modified Nanoparticle-Adsorbed LC Droplets

Our main goal in this study is to synthesize chemically patched, micrometer-sized polymeric LC composite particles in which internal and interfacial structures can be tuned via elastic interactions. Also, we aimed to control surface heterogeneity of the nanoparticles on the LC droplet/water interface and investigate the interparticle

interactions in order to tune the self-assembly of the particles to the elastic medium confined in droplet.

The literature indicates that adsorbates and surface-modified nanoparticles can change the configuration (internal structure) of LC droplets to bipolar, axial, preradial, or radial, as briefly summarized in the Literature Review section above[17,28]. These configurations allow the synthesis of different shapes of polymeric particles due to the anisotropic shrinkage. In the literature, spherical or non-spherical polymeric particles with different initial configurations, which configurations induced by surfactants as mentioned in the Literature Review section, were synthesized by polymerizing the mixture of reactive (RM257) and nonreactive mesogens (5CB) and extraction[20,21,51]. Our first goal in this study is to analyze the shapes of micron-sized polymeric LC droplets upon adsorption of surface modified silica nanoparticles. For the interest of the imaging of LC droplets, we performed experiments with mixtures of the reactive mesogen RM257 in 5CB (25% by weight) and polymerized the reactive mesogens after the adsorption of nanoparticles. Firstly, we made LC droplets (composed of reactive mesogen RM257 in 5CB (25% by weight)) in pure water from that nematic mixture. In pure water, lemon-shaped and spherical polymeric LC droplets which templated from LC droplets in bipolar configuration were obtained (Figure 4.11A). However, in literature, it was shown that dispersing the LC droplet in glycerol or adsorbing the polymers that caused strong planar anchoring such as PVA leads to lemon-shaped polymeric LC droplets that are templated from LC droplets in bipolar configuration[20]. The different shapes of polymeric LC droplets in our experiments resulted in reactive mesogen RM257, which has tilted anchoring in pure water and is used for polymerization[20]. The surface roughness of the bare LC droplet was consistent with literature[20].

We performed experiments with -COOH terminated 87.5 nm ± 7.2 nm-average-sized silica nanoparticles (Si-COOH) with different nanoparticle concentrations. We made LC droplets (composed of reactive mesogen RM257 in 5CB (25% by weight)) in aqueous suspensions of -COOH terminated silica nanoparticles to facilitate their adsorption on LC droplets. After adsorption, we naturally sedimented the LC

droplets and replaced the supernatant with fresh pure water to prevent additional adsorption during the next steps of the synthesis procedures. The literature indicates the irreversible adsorption of nanoparticles to the LC-water interface due to the high energy barrier (adsorption energy~10^5 k_BT); therefore, we did not expect a significant desorption of nanoparticles from the LC droplet-water interface during the supernatant replacement[28]. Finally, we polymerized the LC droplet with UV light and extracted unreactive mesogens with ethanol. When we regarded the configuration distribution of LC droplets exposed to aqueous suspension of -COOH terminated silica nanoparticle with the concentration of 10^7 and 10^{10} particles/mL, we expected the polymerized droplets to be tear-shaped and spherical, respectively, confirmed with SEM images. (Figure 4.11B-C). Although LC droplets in the suspensions of -COOH terminated silica nanoparticles with concentrations of 10^7 and 10^{10} particles/mL had bipolar configuration (Figure 4.11D), we obtained only spherical polymeric for the concentration of 10^{10} particles/mL because the high density of nanoparticles on LC droplets prevented nonuniform shrinkage during extraction of unreactive mesogens[20].

This study was not performed with other surface-modified silica nanoparticles because Sengul et al. has studied them in detail, and the results are available[28]. Besides, Sengul et al. noted that the surface-modified silica nanoparticles with different sizes do not demonstrate the anchoring transition; this study was not repeated with other sizes of silica nanoparticles.

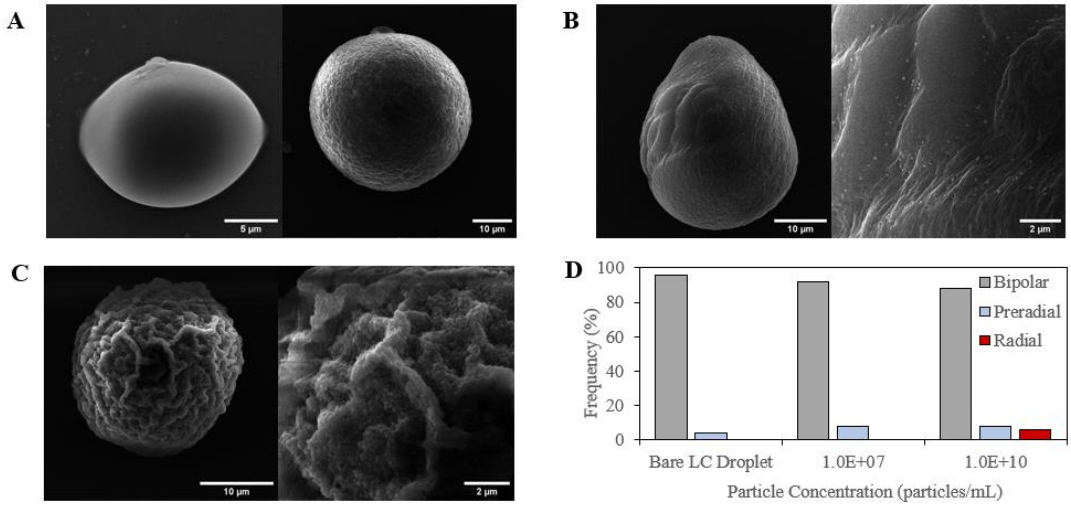

Figure 4.11 SEM micrographs of polymerized LC droplets that were exposed to (A) pure water, (B) aqueous suspensions of -COOH terminated silica nanoparticles with concentration of 10^7 particles/mL, (C) aqueous suspensions of -COOH terminated silica nanoparticles with concentration of 10^{10} particles/mL, (D) configuration distribution of LC droplet in the aqueous suspensions of -COOH terminated silica nanoparticles with different concentrations.

Our second goal in this thesis work is to understand the effects of surface modification (thiols or silanes) and the concentration of surface-modified silica nanoparticles (Si NPs), silver nanoparticles (Ag NPs), or iron oxide nanoparticles (IONPs) to the LC droplets' configuration (internal structure). The literature indicates that different end groups of modification on nanoparticles may change the configuration upon adsorption[28]. For this purpose, first, we performed experiments with aqueous suspensions of mixed monolayer of -COOH and DMOAP terminated silanes functionalized 87.5 nm ± 7.2 nm-average-sized-silica nanoparticles (-COOH/DMOAP mixed monolayer terminated silica nanoparticles (Si-COOH/DMOAP)) which caused titled anchoring condition for LC droplets upon adsorption[28]. LC droplets maintained bipolar configuration with an average of 53.4 ± 5.1% and preradial configuration with an average of 44.5 ± 6.1% frequency when the concentration of surface-modified nanoparticles was 10^7 particles/mL. When the concentration of nanoparticles increased to 10^9 particles/mL, the frequency of bipolar configuration decreased to 33.7 ± 5.0%, whereas preradial configuration increased to 66.3 ± 5.0% (Figure 4.12A). From the SEM images, we realized that the

number of adsorbed nanoparticles on the LC droplets also increased when we increased the concentration of the -COOH/DMOAP mixed monolayer terminated silica nanoparticles in the aqueous suspensions (Figure 4.12B-C). We note that increasing the concentration of nanoparticles leads to near-monolayer coverage of nanoparticles on LC droplets (calculated), which confirms the preradial configuration (tilted anchoring) of -COOH/DMOAP mixed monolayer terminated silica nanoparticles. Below the closed packing (near-monolayer coverage) concentration, the bipolar configuration was more dominant, supporting the partial coverage of nanoparticles.

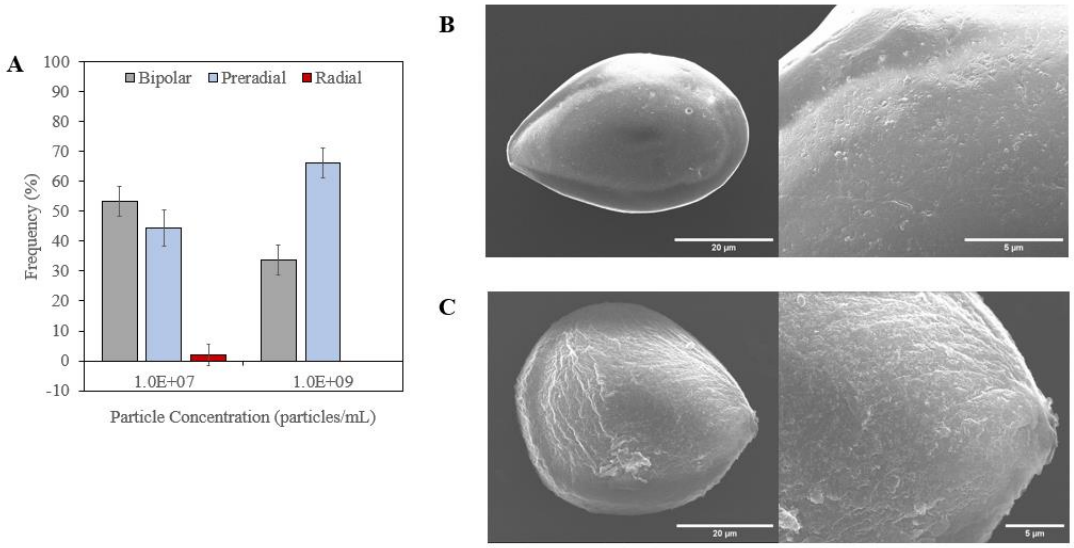

Figure 4.12 (A) Configuration distribution of LC droplets in the suspensions of different concentrations of -COOH/DMOAP mixed monolayer terminated silica nanoparticles, SEM micrographs of polymerized LC droplets that were exposed to -COOH/DMOAP mixed monolayer terminated silica nanoparticles in the concentration of (B) 10^7 particles/mL (C) 10^9 particles/mL before polymerization.

We performed experiments with the surface-modified silver nanoparticles (Ag NPs) to investigate the effects of thiols termination on LC droplets configuration according to the concentration of nanoparticles in the aqueous suspensions. We firstly used aqueous suspensions of -C10 terminated silver nanoparticles (Ag-C10), which introduced planar anchoring to the LC[60]. In this case, we obtained bipolar configuration for LC droplets with 94.7 ± 5.3% frequency for the concentration of

10^{11} particles/mL, as expected (Figure 4.13A). Secondly, we used mixed monolayers of -C10 and -C16 terminated thiols for surface modification of silver nanoparticles (-C10/C16 mixed monolayer terminated silver nanoparticles (Ag-C10/C16)), and in the literature, this termination introduces homeotropic (or tilted) anchoring condition to LC in the gold film form [60]. We used 3 μL of 5CB to make LC droplets in 1 mL suspension for experiments below until the opposite is stated. We found that with the increasing concentration of mixed monolayers of -C10/C16 (4:1) mixed monolayer terminated silver nanoparticles in the aqueous suspensions, radial and preradial configurations were dominant. The LC droplets exhibited in the average of 36.0 ± 15.1%, 37.2 ± 15.8%, and 26.8 ± 10.1% bipolar, preradial and radial configurations frequency, respectively, for nanoparticle concentrations of 3 x 10^{14} particles/mL, whereas the frequency of the bipolar, preradial and radial configurations changed to 58.8 ± 5.0%, 39.2 ± 12.4%, and 2.0 ± 7.0% for the concentration of 5.8 x 10^{7} particles/mL. For the concentration of 5.5 x 10^{10} particles/mL, we obtained preradial configuration more dominantly with the 86.4 ± 10.5% frequency (Figure 4.13B). We made two observations from these results. First, we observed configuration distribution upon adsorption of -C10/C16 (4:1) mixed monolayer terminated silver nanoparticles on LC droplets, but we observed only bipolar configuration for -C10 terminated silver nanoparticles. The reasons of the configuration distribution for -C10/C16 (4:1) mixed monolayer terminated silver nanoparticles were the surface heterogeneity of silver nanoparticles[66]. Second, we observed that preradial configuration was more dominant in the medium with nanoparticle concentration of 5.5 x 10^{10} particles/mL. Equilibrating the LC droplets with the medium of nanoparticle concentration that is less than near-monolayer coverage could result in partial coverage of the LC droplet, which is expected to decrease in radial configuration frequency and increase in preradial and bipolar configuration frequency. Our experiments proved this expectation, which indicates that partial coverage of -C10/C16 (4:1) mixed monolayer terminated silver nanoparticles on LC droplets exhibits a high frequency of the preradial and bipolar configurations at the medium nanoparticle concentrations. Moreover, for the interest

of the controlling configuration distribution of LC droplets, we performed experiments with -C10/C16 (4:1) mixed monolayer terminated silver nanoparticles for the concentration of 3.2 x 10^{10} particles/mL and changed the volume of 5CB (1 or 3 μL of 5CB). First, we used 1 μL of 5CB to make LC droplets in 1 mL suspension, and we obtained bipolar, preradial, and radial configurations in an average of 32.9 ± 6.9% and 56.4 ± 8.8%, and 10.7 ± 4.2% frequency, respectively. Second, we used 3 μL of 5CB, and we observed that while the frequency average of radial configuration decreased to 1.9 ± 1.3%, bipolar and preradial configurations increased to 37.3 ± 2.2%, 60.8 ± 2.6%, respectively (Figure 4.13C). The reason for the change in the frequencies of configurations is the variation in the number of particles per surface area. A decrease in the volume of 5CB also decreases the total surface area, which may increase the interfacial adsorbed-nanoparticles concentration on a droplet. Approximate values for number of nanoparticles/surface area were calculated as 35 particles/μm^2 and 106 particles/μm^2 for the 3 and 1 μL 5CB addition, respectively (diameter of LC droplet assumed as 20 μm for both cases). The closest packing fraction of solid spherical particles on a spherical surface is 74%[68], and this ratio requires at least 7.1 x 10^{11} and 2.15 x 10^{12} particles/mL for LC droplets formed from 1 and 3 μL 5CB. The fractions of 35 particles/μm^2 and 106 particles/μm^2 corresponds to 1.5% and 4.5% of the closest packing fraction. The increase in the number of particles per surface area leads to the increase in droplet coverage, which explains the increase in radial configuration.

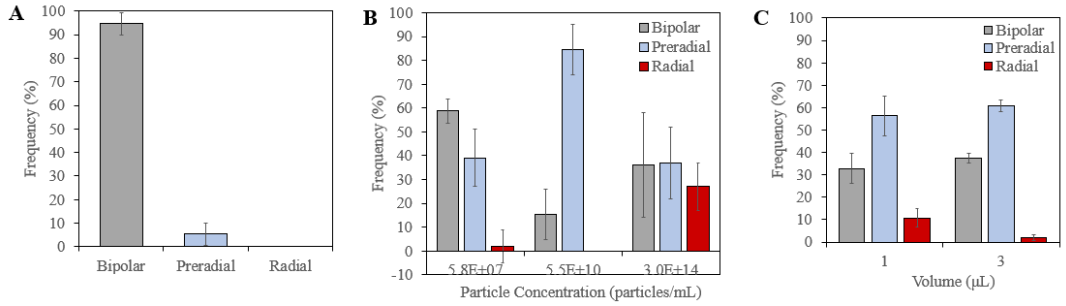

Figure 4.13 Configuration distribution of LC droplets in the aqueous suspensions of (A) -C10 terminated silver nanoparticles, (B) -C10/C16 (4:1) mixed monolayer terminated silver nanoparticles in different nanoparticles concentration, (C) -C10/C16 (4:1) mixed monolayer terminated silver nanoparticles when different volume of 5CB was used.

Representative SEM images of the mixed monolayer of -C10 and -C16 terminated thiols functionalized silver nanoparticles (-C10/C16 mixed monolayer terminated silver nanoparticles (Ag-C10/C16)) adsorbed polymerized LC droplets and backscattering mode micrograph were shown in Figure 4.14A. We analyzed the configuration distribution of -C10/C16 mixed monolayer terminated silver nanoparticles adsorbed LC droplets according to droplet size. We observed that while radial configuration was only exhibited below 12 μm diameter, bipolar and preradial configuration was distributed in a wide range (5-30 μm) Figure 4.14B. Similarly, radial configuration reached the highest frequency of 36% for droplet diameter range 8-10 μm; however, bipolar and preradial configuration were in averages of 15% (Figure 4.14C). We note that smaller-sized droplets could have enough nanoparticles to nearly cover the droplet surface, so radial configuration reaches the highest frequency for the smaller diameter. The Introduction section of this thesis discussed the characteristic size scale of 1-10 μm. As a reminder, the ratio of elastic energy to the surface anchoring energy gives a characteristic length between 1-10 μm. Below this range, LC droplets are dominated by elasticity, where droplets have a uniform director configuration with no strain. Above this range, the droplets have a configuration that satisfies surface anchoring condition[15,19,69]. In the literature, the configuration of bare LC droplets in pure water according to droplet size was investigated, and it was indicated that decreasing the droplet size leads to

bipolar to preradial to radial configurations, which contrast to the theoretical predictions[69]. In our experiments, we analyzed the droplet sizes between 5-35 μm, which includes the characteristic length range (1-10 μm) and above. Therefore, we did not expect to observe size-dependent bare LC droplet configuration transition as described above in the Literature section. The radial configuration below 12 μm in our experiment could result from the near-monolayer coverage of -C10/C16 mixed monolayer terminated silver nanoparticles on LC droplets. These results allow to the synthesis of polymeric micrometer-sized particles with desired internal polymer structure that can be arranged not only with the concentration of aqueous suspension but also with droplet size.

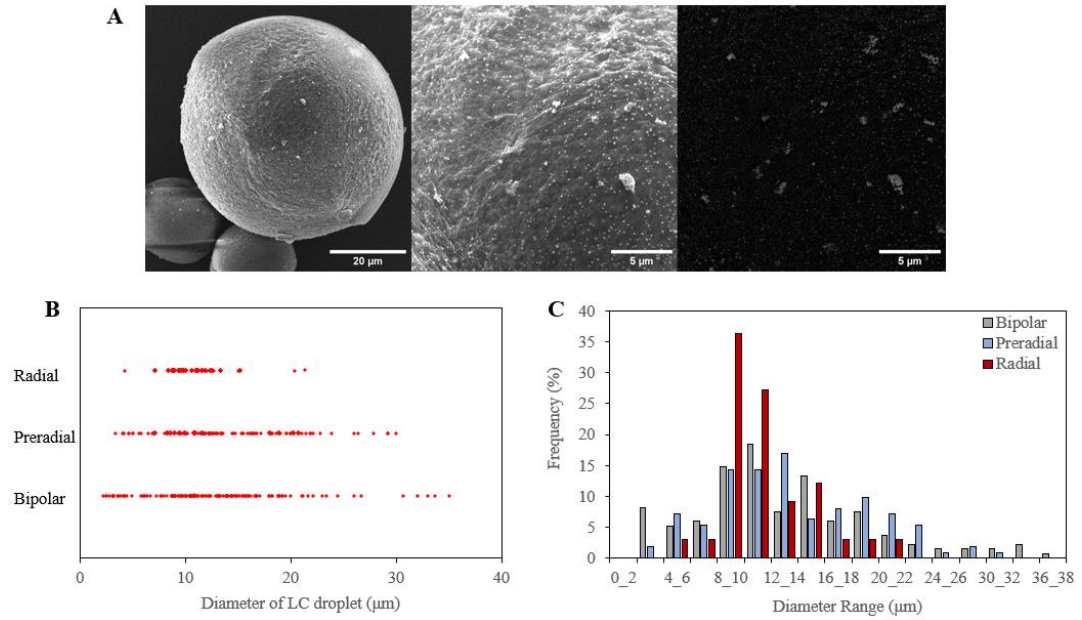

Figure 4.14 (A) SEM micrographs of nanoparticles adsorbed-polymerized LC droplets, (B) Configuration distribution of LC droplets according to droplet size, (C) Configuration distribution of LC droplets according to the size range of droplet. Before polymerization, the LC droplets were exposed to -C10/C16 mixed monolayer terminated silver nanoparticles.

We performed experiments with the aqueous suspension of iron oxide nanoparticles (IONPs) functionalized with mixed monolayer of -C10 and -C16 terminated thiols (-C10/C16 mixed monolayer terminated IONPs (IONP-C10/C16)) and quantified the configuration distribution of LC droplets upon adsorption of these nanoparticles. In

these experiments, we examined the effects of thiols ratios on the response of LC droplets with different nanoparticles concentration. We modified the surface of the nanoparticles with mixed monolayers of -C10/C16 with the thiol's ratio of either 4:1 or 1:4. Similarly, with -C10/C16 mixed monolayer terminated silver nanoparticles, LC droplets exhibited in preradial configuration more as the concentration of nanoparticles increased. When we used aqueous suspension of -C10/C16 (1:4) mixed monolayer terminated iron oxide nanoparticles with 1.5×10^7 and 1.5×10^9 particles/mL, the bipolar configuration frequency decreased from $39.2 \pm 22\%$ to $33.2 \pm 17\%$, the preradial configuration increased from $47.3 \pm 5.1\%$ to $54.2 \pm 9.3\%$, and radial configuration increased from $13.4 \pm 17.6\%$ to $19.9 \pm 21.3\%$ (Figure 4.15A). Similarly, for -C10/C16 (4:1) mixed monolayer terminated iron oxide nanoparticles with 1.5×10^7 and 1.5×10^9 particles/mL, the bipolar configuration frequency decreased from $42.5 \pm 20.1\%$ to $27.2 \pm 13.3\%$, the preradial configuration increased from $43.8 \pm 8.1\%$ to $52.9 \pm 12.7\%$ and radial configuration increased from $13.7 \pm 23.8\%$ to $19.9 \pm 21.3\%$ (Figure 4.15A). We observed approximately the same frequencies of configuration for thiol concentration as 1:4 or 4:1, so we note that there was no significant dependence of the thiol concentration on the configuration of LC droplet upon adsorption (Figure 4.15A). To examine the density of -C10/C16 (4:1) mixed monolayer terminated iron oxide nanoparticles on the LC droplet as a function of concentration in the aqueous suspensions, we used aqueous suspension with a concentration of 2.1×10^7 particles/mL and 2.1×10^9 particles/mL. The proportion of nanoparticles on the LC droplet was denser for the higher concentration (2.1×10^9 particles/mL), which explains the higher frequency of radial and preradial configuration (Figure 4.15B-C).

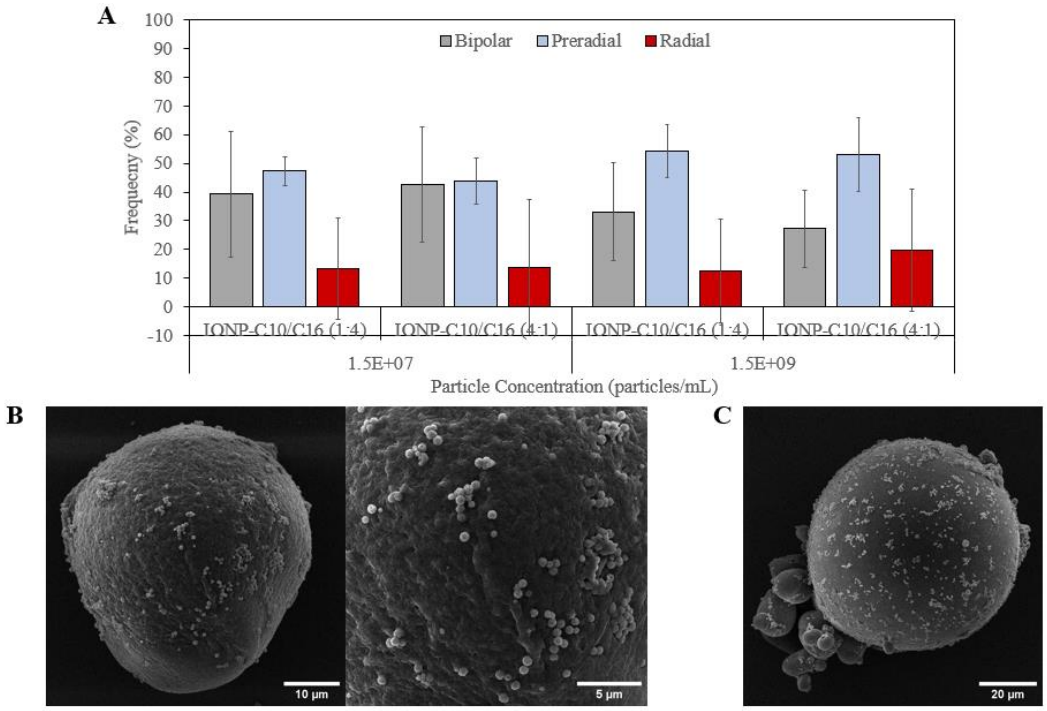

Figure 4.15 (A) Configuration distribution of LC droplets upon adsorption of -C10/C16 mixed monolayer terminated IONPs with different thiol concentrations, SEM micrographs of -C10/C16 mixed monolayer terminated IONPs adsorbed-polymerized LC droplet with the concentration of (B) 2.1 x 10^7, (C) 2.1 x 10^9 particles/mL.

We exposed the LC droplet decorated with iron oxide nanoparticles (IONPs) to an external magnetic field to examine the effect of magnetic particles adsorbed on the LC droplet to the movement. The optical observation was carried out using a polarized optical microscope at bright field mode. Initially, nanoparticle adsorbed-LC droplet and free nanoparticles in the medium had Brownian motion at rest (Figure 4.16A). When the sample was exposed to an external magnetic field, the nanoparticle adsorbed-LC droplet started to rotate immediately according to the direction of the magnetic field (Figure 4.16B-C). We also note that the free nanoparticles were oriented with respect to the direction of the magnetic field (Figure 4.16B-C). When we removed the external magnetic field, free nanoparticles and nanoparticles adsorbed-LC droplets resumed Brownian motion with no specific direction (Figure 4.16D). These results provide basic knowledge for the movement of polymeric

particles in the desired direction, allowing the synthesis of mobile micrometer-sized polymeric particles.

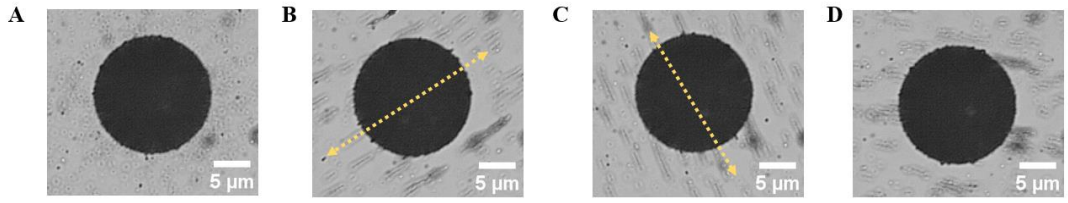

Figure 4.16 Brightfield micrographs of the nanoparticles-adsorbed-LC droplet and free nanoparticles (A) in the absence of external magnetic field at the initial state, (B-C) with the magnetic field from left and right, respectively, (D) in the absence of external magnetic field at the end of the experiment.

We performed adsorption experiments with the silver and iron oxide nanoparticles functionalized with the mixed monolayer of -COOH and -C16 terminated thiols (-COOH/C16 mixed monolayer terminated silver or iron oxide nanoparticles (Ag-COOH/C16 or IONP-COOH/C16)). We investigated nanoparticle concentration dependence on the configuration distribution of LC droplets. When we used the aqueous suspension of -COOH/C16 (1:4) mixed monolayer terminated iron oxide nanoparticles with 1.5 x 10^8 and 1.5 x 10^{10} particles/mL, the bipolar configuration frequency decreased from 63.3 ± 6.6% to 34.8 ± 11.1%, the preradial configuration increased from 33.4 ± 6.6% to 60.7 ± 17.4%, and radial configuration increased from 3.3 ± 5.8% to 5.9 ± 5.2% (Figure 4.17A). Also, for -COOH/C16 (4:1) mixed monolayer terminated iron oxide nanoparticles with 1.5 x 10^8 and 1.5 x 10^{10} particles/mL, the bipolar configuration frequency decreased from 67.7 ± 11.1% to 29.7 ± 20%, the preradial configuration increased from 32.3 ± 11.1% to 62.3 ± 19.4%, and radial configuration increased from 0% to 7.9 ± 3.6% (Figure 4.17A). Similarly, with mentioned results, preradial and radial configuration frequency increased when the concentration of nanoparticles increased, and no thiol concentration dependence was observed for -COOH/C16 mixed monolayer terminated iron oxide nanoparticles (Figure 4.17A). We investigated the configuration distribution of LC droplets upon adsorption of -COOH/C16 mixed monolayer terminated silver nanoparticles. As expected, an increase in the

concentration of nanoparticles led the most probable configuration distribution to change to preradial configuration. Frequency of bipolar configuration decreased from 70.4 ± 16.1% to 36.7 ± 6.8%, preradial configuration increased from 28.7 ± 15.5% to 59.6 ± 8.8% and radial configuration increased from 1 ± 1.5% to 3.6 ± 3.8% as the concentration of nanoparticles increased from 2 x 10^7 to 3.5 x 10^9 particles/mL (Figure 4.17B). These results revealed that the adsorption of surface-modified silver and iron oxide nanoparticles on LC droplets led configuration changes of LC droplets, which depended on the concentration of nanoparticles and surface modification type. When we compared the adsorption experiments results of approximately 10^9 and 10^{10} particles/mL of -C10/C16 mixed monolayer terminated silver nanoparticles and -COOH/C16 mixed monolayer terminated silver nanoparticles, we realized preradial configuration were more dominant for -C10/C16 mixed monolayer terminated silver nanoparticles, which highlight the surface-modification type effect.

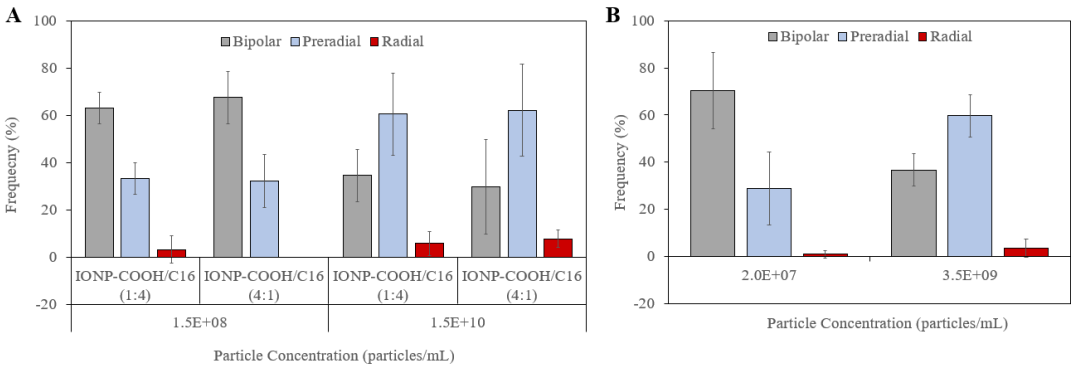

Figure 4.17 Configuration distribution of LC droplets according to nanoparticle concentration upon adsorption of (A) -COOH/C16 mixed monolayer terminated IONPs with 1:4 and 4:1 thiol concentration, (B) -COOH/C16 mixed monolayer terminated silver nanoparticles.

Our third goal in this thesis work is to determine the controlled adsorption mechanism of charged nanoparticles. The literature indicates that, firstly, LC and surface terminated nanoparticles' surface charges can be altered via pH[59,70–74]. Secondly, adsorption of nanoparticles to the LC droplet-water interfaces highly depends on surface charge of nanoparticles[28]. In the literature, 5CB emulsions in

pure water stated negatively charged[28,70]. First, we measured 5CB droplets in various pH of 2-6 and we found a range 23.1 mV ± 5.3 mV to -28.2 mV ± 1.5 mV, respectively. Second, we measured the zeta potential of -C10/C16 and -COOH/C16 mixed monolayer terminated iron oxide nanoparticles (IONP) and silver nanoparticles (Ag NPs) as shown in Figure 4.18. We selected two different pH to investigate the adsorption rate and response of LC droplets (pH of 3 and 6). At pH of 3, LC droplets and nanoparticles were oppositely charged, but at pH of 6, those were negatively charged. The zeta potential values were summarized in Table 2.

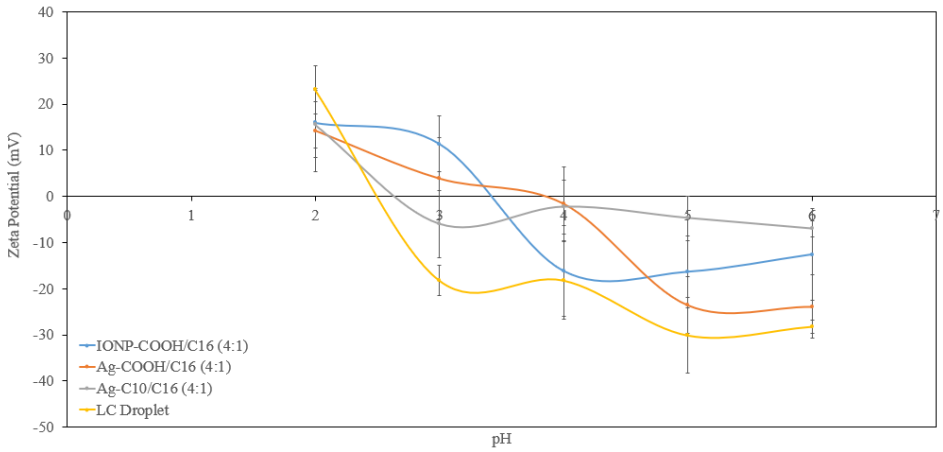

Figure 4.18 Zeta potential of the LC droplets and surface modified iron oxide and silver nanoparticles as a function of pH.

Table 2 Zeta potential values of surface-modified silver and iron oxide nanoparticles and LC droplets at pH of 3 and 6.

	Zeta potential	
	pH	
	3	6
LC droplet	-18.2 mV ± 3.3 mV	-28.2 mV ± 1.5 mV
Ag-C10/C16 NPs		-7.0 mV ± 1.8 mV
Ag-COOH/C16 NPs	3.9 mV ± 8.8 mV	-23.8 mV ± 6.8 mV
IONP-COOH/C16	11.4 mV ± 5.9 mV	-12.6 mV ± 9.9 mV

First, we examined the zeta potential of silver nanoparticles modified with -C10 and -C16 terminated thiols (-C10/C16 mixed monolayer terminated silver nanoparticles (Ag-C10/C16)) at pH of 6. The -C10/C16 mixed monolayer terminated silver nanoparticles were found to be negatively charged (-7.0 mV ± 1.8 mV) at pH=6 (Figure 4.19B and Table 2). In the literature, surface modification of nanoparticles with a single monolayer of -C10 is stated as negative zeta potential, consistent with our measurements of -21.8 mV ± 4.4 mV (Figure 4.9A)[75]. We performed adsorption experiments to analyze the configuration distribution of the LC droplets present in suspensions of -C10/C16 mixed monolayer terminated silver nanoparticles at pH ≈ 5.7 (pure water) with respect to time. We observed the preradial and radial configuration frequency increase with respect to time. After 5 min adsorption, the LC droplets exhibited mostly bipolar configuration at an average of 58.9 ± 6.1%, whereas after 60 min adsorption, bipolar configuration frequency decreased to 32.4 ± 4.5%. Preradial and radial configuration increases from 41.1 ± 6.1% and 0% to 59 ± 5.4% and 8.5 ± 1.5%, respectively. After 95 min adsorption, we did not observe a dramatic change in the configuration frequencies (Figure 4.19A). The increase in the

preradial and radial configurations resulted from the increase in the adsorption of nanoparticles to the LC droplet-water interface. The increase in the adsorption of nanoparticles to the LC droplet interface as time proceeds is the electrostatic repulsion between negatively charged LC droplets and surface-modified silver nanoparticles, shown in Figure 4.19B, lowers the adsorption rate of nanoparticles, which is consistent with literature[28]. Figure 4.19C is the schematic illustration of nanoparticles adsorption on LC droplets as time proceeded.

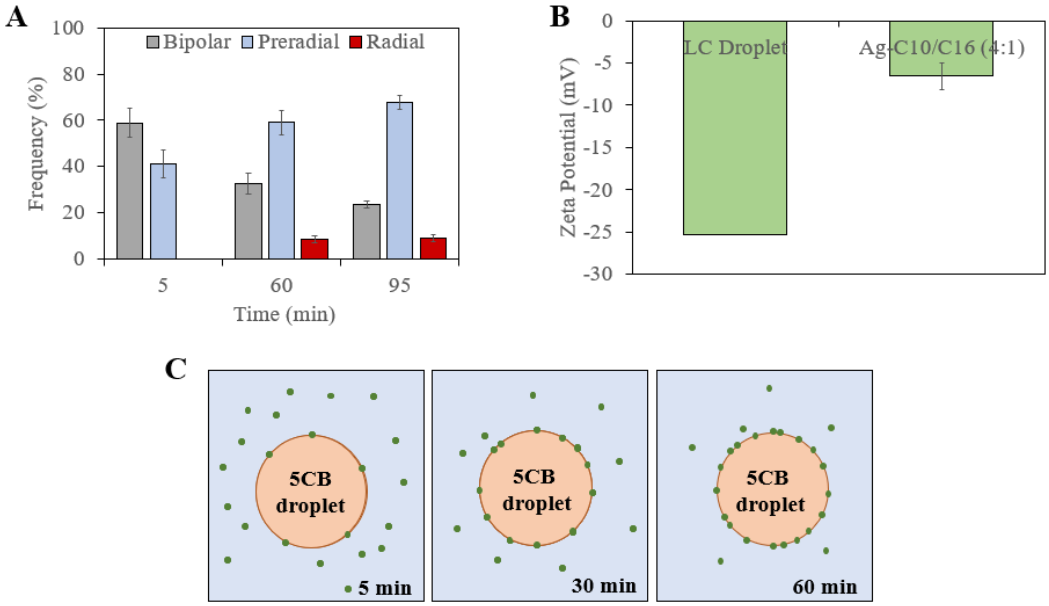

Figure 4.19 (A) Configuration distribution of LC droplets upon absorption of -C10/C16 mixed monolayer terminated silver nanoparticles with respect to time in pure water, (B) zeta potential measurements of LC droplet and -C10/C16 mixed monolayer terminated silver nanoparticles in pure water (pH=5.7), (C) schematic illustration of nanoparticles adsorption rate on LC droplet w.r.t. time.

Second, we investigated the configuration distribution of LC droplets upon adsorption of silver and iron oxide nanoparticles modified with mixed monolayer of -COOH and -C16 (4:1) terminated thiols (-COOH/C16 mixed monolayer terminated silver (Ag-COOH/C16) and iron oxide nanoparticles (IONP-COOH/C16)) with respect to time. For -COOH/C16 mixed monolayer termination, 11-mercaptoundecanoic acid (MUA) and 1-hexadecanethiol was used. The isoelectric point of -COOH/C16 (4:1) mixed monolayer terminated silver and iron oxide

nanoparticles were found to be pH~3.7 and pH~3.5, respectively. In the literature, the isoelectric point of only MUA-modified nanoparticles was recorded as 3.58[72]. Our measurements were reasonably consistent with the literature since adding -C16 alkyl chain may change the isoelectric point. The pK_a for MUA in solution is 4.8, but literature reported that MUA-modified nanoparticles might differ from pK_a in solution, which is consistent with our experiments[71]. LC droplets exhibited time-dependent configuration distribution upon adsorption of -COOH/C16 (1:1) mixed monolayer terminated silver nanoparticles with the concentration of 10^9 particles/mL. In 5 min adsorption time interval, LC droplets maintained bipolar configuration with an average of 74.5 ± 5.5% frequency and preradial configuration with 25.5 ± 5.5% frequency. After 30 min adsorption, the average frequency of bipolar configuration decreased to 51.3 ± 8.9%, while preradial and radial configuration increased to 46.1 ± 8.5 and 2.1 ± 1.9%, respectively. Lastly, after 1 h adsorption, LC droplets exhibited bipolar configuration in average of 43.7 ± 22.7%, preradial configuration in average of 47.3 ± 27.1%, and radial configuration in average of 9.0 ± 5.0% frequencies (Figure 4.20A). Similarly, as time proceeded, we observed higher frequencies for preradial and radial configurations for -COOH/C16 (4:1) mixed monolayer terminated iron oxide nanoparticles with a concentration of 1.5 x 10^9 particles/mL. As time proceeded, the frequencies for preradial and radial configuration increases, which resulted from increase in adsorption of nanoparticles (Figure 4.20B). For both nanoparticles, we observed the same phenomena with -C10/C16 mixed monolayer terminated silver nanoparticles, as mentioned above. Due to the negative charge of both LC droplets and -COOH/C16 mixed monolayer terminated silver and iron oxide nanoparticles, there was an electrostatic repulsion that decelerate the adsorption rate of nanoparticles to the LC-water interface. At pH=6 LC droplets, -COOH/C16 mixed monolayer terminated silver and iron oxide nanoparticles exhibited negative zeta potentials, which are -28.2 mV ± 1.5 mV, -23.8 mV ± 6.8 mV, and -12.6 mV ± 9.9 mV as shown in Table 2. All zeta potential and corresponding pH values can be found in Figure 4.18.

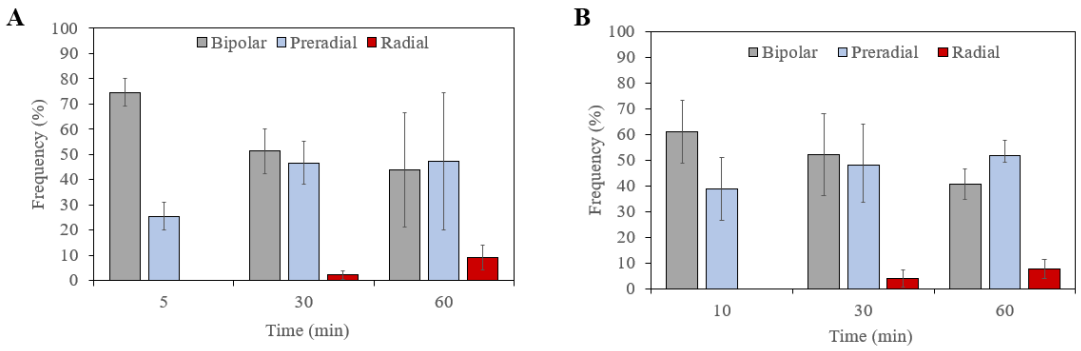

Figure 4.20 Configuration distribution of LC droplets upon adsorption of (A) -COOH/C16 (1:1) mixed monolayer terminated silver nanoparticles, (B) -COOH/C16 (4:1) mixed monolayer terminated IONPs with respect to time.

To investigate the difference between the adsorption of nanoparticles at different pH, we used nanoparticles modified with mixed monolayer of -COOH and C16 terminated thiols (-COOH/C16 (4:1) mixed monolayer terminated) pH of either 3 or 6. We arranged LC droplets and nanoparticles with negative and opposite charges for the adsorption experiments. At pH=3 and pH=6, zeta potential of LC droplets was measured as -18.2 mV ± 3.3 mV and -28.2 mV ± 1.5 mV (Table 2). Firstly, we used -COOH/C16 (4:1) mixed monolayer terminated silver nanoparticles (Ag-COOH/C16). At pH=3, the zeta potential of -COOH/C16 mixed monolayer terminated silver nanoparticles were measured as 3.9 mV ± 8.8 mV, and at pH=6, it was measured as -23.8 mV ± 6.8 mV (Table 2). In both pH, the LC droplets and -COOH/C16 mixed monolayer terminated silver nanoparticles maintained opposite surface charges. However, at pH=3, -COOH/C16 mixed monolayer terminated silver nanoparticles exhibited surface charge near to isoelectric point. After 1 h adsorption of nanoparticles with concentration of 1.2 x 10^9 particles/mL, LC droplets maintained bipolar configuration frequency of 41.8 ± 4.0% and 53.7 ± 3.3% for pH of 3 and 6, respectively. Preradial configuration frequency was found to be 48.4 ± 16 % and 41.4 ± 9.5% for pH of 3 and 6, respectively. Lastly, LC droplets maintained radial configurations in average of 9.8 ± 12.5% and 5.0 ± 6.6% for pH of 3 and 6, respectively (Figure 4.21A). Secondly, we used -COOH/C16 (4:1) mixed monolayer terminated iron oxide nanoparticles (IONP-COOH/C16). At pH=3, the zeta potential

of -COOH/C16 mixed monolayer terminated iron oxide nanoparticles was measured as +11.4 mV ± 5.9 mV, and at pH=6, it was measured as -12.6 mV ± 9.9 mV (Table 2). In these experiments, at pH=3, LC droplets and -COOH/C16 (4:1) mixed monolayer terminated iron oxide nanoparticles were oppositely charged, while at pH=6, both were negatively charged. LC droplets maintained an average of 32.5 ± 8.6% and 49.9 ± 16.8% frequencies of bipolar configuration for pH=3 and pH=6, respectively. The frequency of preradial configuration was 65.3 ± 11.8% and 44.8 ± 11.3% for pH=3 and pH=6, respectively and the radial configuration frequency was 2.2 ± 3.8% and 5.4 ± 5.9% for pH=3 and pH=6, respectively (Figure 4.21B). From these configuration distributions at different pH of mediums, we hypothesized that the electrostatic repulsion force between nanoparticles and LC droplets was low at pH=3. Hence the adsorption of nanoparticles occurred high enough to obtain partial surface coverage of LC droplet; therefore, higher preradial and radial configuration frequency was observed at pH=3 compared to pH=6. All zeta potential and corresponding pH values can be found in Figure 4.18 and Table 2.

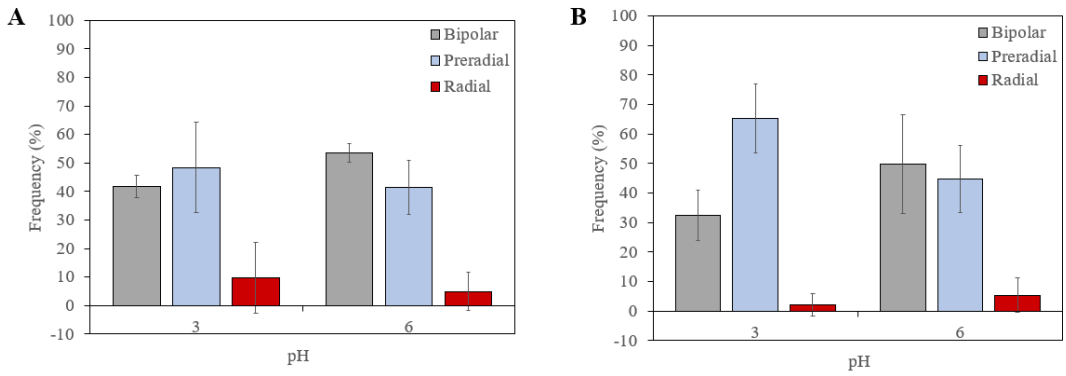

Figure 4.21 Configuration distribution of LC droplets upon adsorption of (A) -COOH/C16 (4:1) mixed monolayer terminated silver nanoparticles, (B) -COOH/C16 (4:1) mixed monolayer terminated IONPs with respect to pH of medium.

Due to the electrostatic attraction force in the case of the oppositely charged nanoparticle and LC droplet (at pH=3), we hypothesized that the nanoparticles are denser at the LC droplet interface. Therefore, we used silica nanoparticles functionalized with DMOAP and -COOH terminated silanes (-COOH/DMOAP mixed monolayer terminated silica nanoparticles (Si-COOH/DMOAP)) to test the

hypothesis. At pH=3, LC droplets and -COOH/DMOAP mixed monolayer terminated silica nanoparticles were oppositely charged (negative and positive). The zeta potential of droplets was -18.2 mV ± 3.3 mV, and the zeta potential of -COOH/DMOAP terminated silica nanoparticles was +21.2 ± 2.7 mV. At pH 6, droplets and nanoparticles were negatively charged, and zeta potentials were measured as -28.2 mV ± 1.5 mV and -21.6 mV ± 2.8 mV, respectively (Figure 4.22A). Firstly, we investigated the response of LC droplets upon adsorption of -COOH/DMOAP mixed monolayer terminated silica nanoparticles at a concentration of 8.1 x 10^9 particles/mL at pH=3 and pH=6. At pH=3, LC droplets maintained bipolar configuration in average of 18.5 ± 9.3% and preradial configuration in average of 80.6 ± 10.2%. However, at pH=6, LC droplets maintained bipolar configuration in average of 35.8 ± 4.9% and preradial configuration in average of 64.2 ± 5.0%. As in -COOH/C16 (4:1) mixed monolayer terminated silver and iron oxide nanoparticles, LC droplets maintained at preradial configuration dominantly at pH=3. SEM images were taken to understand the interface coverage of droplets at pH=3 and 6. As shown in Figure 4.22C-D, even if the concentration of nanoparticles were equal, the nanoparticle adsorption to the LC droplets was more for the pH=3 scenario (Figure 4.22C) than the pH=6 scenario (Figure 4.22D), which is consistent with our response test experiments, hypothesis, and literature[28].

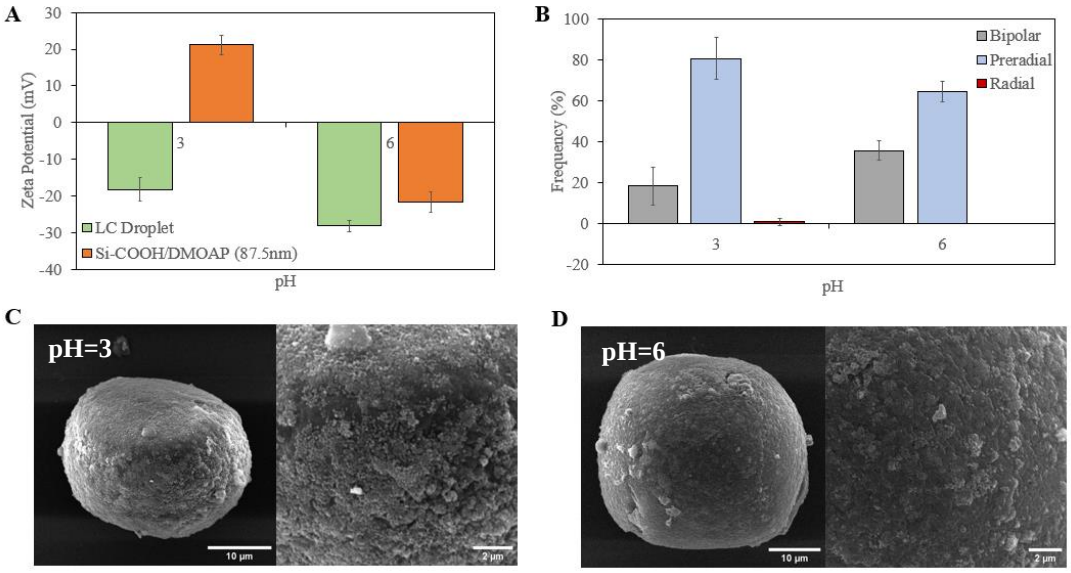

Figure 4.22 (A) Zeta potential measurements for LC droplets and -COOH/DMOAP mixed monolayer terminated silica nanoparticles at pH=3 and pH=6, (B) Configuration distribution of LC droplets upon adsorption of -COOH/DMOAP mixed monolayer terminated silica nanoparticles at different pH values, SEM micrographs of -COOH/DMOAP mixed monolayer terminated silica nanoparticles at the same concentration of 8.1 x 10^9 particles/mL at (C) pH=3, (D) pH=6.

Our last goal in this thesis work is to control the preferential adsorption mechanism of charged nanoparticles and to understand interparticle interactions on an elastic medium. For that purpose, we used different sizes of surface-modified silica nanoparticles (Si NPs). We firstly investigated the dependence of the surface charge of nanoparticles on the pH of medium. We used -NH_2 terminated silica nanoparticles (from 87.5 nm ± 7.2 nm and 417.1 nm ± 22.1 nm-average-sized bare silica) and -COOH and terminated silica nanoparticles (from 87.5 nm ± 7.2 nm and 51.2 nm ± 9.0 nm-average-sized bare silica). The isoelectric point of -COOH terminated silica nanoparticles (Si-COOH) were found at approximately pH~ 3.4 and for -NH_2 terminated silica nanoparticles (Si-NH_2), approximately pH~ 6.5, which are consistent with literature[28,73,74]. Zeta potential measurements are shown in Figure 4.23.

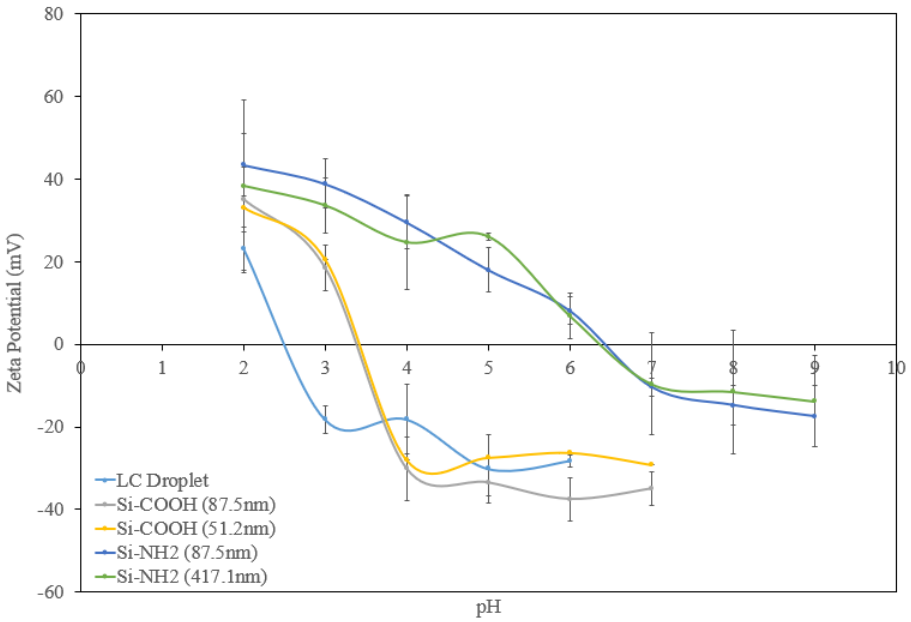

Figure 4.23 Zeta potential of the LC droplets and surface-modified silica nanoparticles as a function of pH.

-COOH terminated 87.5 nm ± 7.2 nm-average-sized-silica nanoparticles (Si-COOH) did not change the LC droplet response upon nanoparticles' adsorption at pH 3 or 6 which is consistent with literature[28] (Figure 4.24A). We observed silica nanoparticles to be more concentrated on LC droplet surfaces for concentration of 1.6 x 10^{10} particles/mL compared to 5.0 x 10^{8} particles/mL at pH=3, as expected (Figure 4.24B-C). Besides even the concentration of 1.6 x 10^{10} particles/mL at pH=6 was higher than the concentration of 5.0 x 10^{8} particles/mL at pH=3, we observed a higher density of nanoparticles on LC droplet interface at pH=3 (Figure 4.24C-D). At pH 3, LC droplet and -COOH terminated silica nanoparticles were oppositely charged (-18.2 mV ± 3.3 mV and 18.5 mV ± 5.6 mV) (Figure 4.23); therefore, the attraction force between LC droplet and -COOH terminated silica nanoparticles resulting in more adsorption on the interface as indicated before. Wrinkling of the particle monolayer was observed on the droplet interfaces at pH=3 at a concentration of 1.6 x 10^{10} particles/mL (Figure 4.24B). This phenomenon resulted from the shrinkage of the polymerized LC droplets after the extraction of the 5CB[20,24,25,28]. One of the important observations from the SEM micrographs was the particle characteristics

on elastic medium at different pH values. We observed that at pH=3, the nanoparticles absorbed on LC droplets were more aggregate than those at pH=6 (Figure 4.24C-D). The literature indicates that the lower zeta potential of a colloidal suspension implies the electrostatic repulsion or energy barrier in between nanoparticles is lowered, which promotes particle aggregation in the suspension[76–78]. Thus, we concluded the reason of the particle aggregation was resulted from the lower zeta potential in pH=3 than pH=6 (Figure 4.23). Therefore, we desired further investigation of adsorbed nanoparticle characteristics upon changing the pH of the medium.

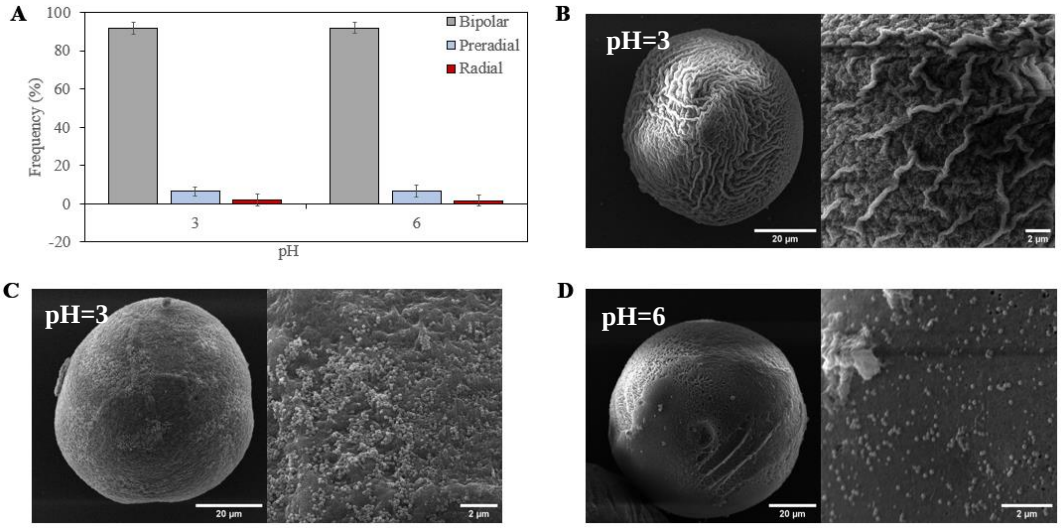

Figure 4.24 (A) Configuration distribution of LC droplets upon adsorption of -COOH terminated silica nanoparticles at different pH values, SEM micrographs of polymerized LC droplets upon adsorption of -COOH terminated silica nanoparticles at concentration of (B) 1.6 x 10^{10} particles/mL at pH=3, (C) 5.0 x 10^{8} particles/mL at pH=3, (C) 1.6 x 10^{10} particles/mL at pH=6.

To investigate whether we can manipulate the interparticle interaction and position of nanoparticle on an elastic medium, we designed an experiment with -COOH terminated 87.5 nm ± 7.2 nm-average-sized silica nanoparticles (Si-COOH). As a first step, we aimed to disaggregate the aggregated-adsorbed nanoparticles at pH=3 by using electrostatic interactions as shown in Figure 4.25. Studies showing that nanoparticles adsorbed on the interface of LC droplets are mobile on the surface and maintain their position after polymerization are mentioned in the Literature Review

section above[15,51,57,79–82]. Firstly, we exposed polymerizable LC droplets (mixtures of the reactive mesogen RM257 in 5CB (25% by weight)) to -COOH terminated silica nanoparticles with a concentration of 5.0 x 10^8 particles/mL at pH=3. After 30 min adsorption, we allowed the nanoparticles-adsorbed polymerizable LC droplets naturally sediment. After natural sedimentation, we first changed the supernatant with fresh pure water with a pH of 3 at least three times to remove free nanoparticles from the system. Then, we changed the supernatant with fresh pure water with a pH of 6 at least three times and equilibrated for 1 h. Finally, we polymerized the LC droplets. For the control group, we did not change the system pH to 6; we directly polymerized the LC droplets after removing the free nanoparticles. After polymerization, we expected no mobilization of nanoparticles on polymerized LC droplets as in literature[13,51]. Representative SEM micrographs of the control group, which described the characteristics of adsorbed nanoparticles at pH of 3, were shown in Figure 4.26A. In the control group, we observed aggregated-adsorbed nanoparticles as before. Scatter map of nanoparticles that were adsorbed at pH of 3 to the interface of the LC droplet confirms the aggregation (Figure 4.26C). After pH was changed to 6, we observed a more homogeneous LC droplet interface. The aggregated nanoparticles were disturbed and spread over the droplet's interface (Figure 4.26B). Scatter map of nanoparticles that adsorbed at pH of 3 and changed to pH of 6 before polymerization confirmed more homogeneous and singular nanoparticles on the interface (Figure 4.26D). The nanoparticle's disaggregation on the interface resulted from the increase in the zeta potential of nanoparticles (absolute values). At pH of 3 and 6, -COOH terminated silica nanoparticles exhibited zeta potential of 18.5 mV ± 5.6 mV and -37.5 mV ± 5.2 mV, respectively (Figure 4.23). The higher zeta potential of nanoparticles causes an increase in electrostatic repulsion or overcoming the energy barrier between nanoparticles, which results in particle separation.

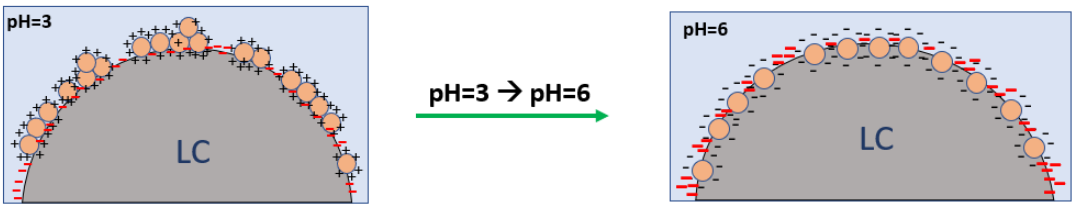

Figure 4.25 Schematic illustration of disaggregating the aggregated-adsorbed nanoparticles on LC-water interface.

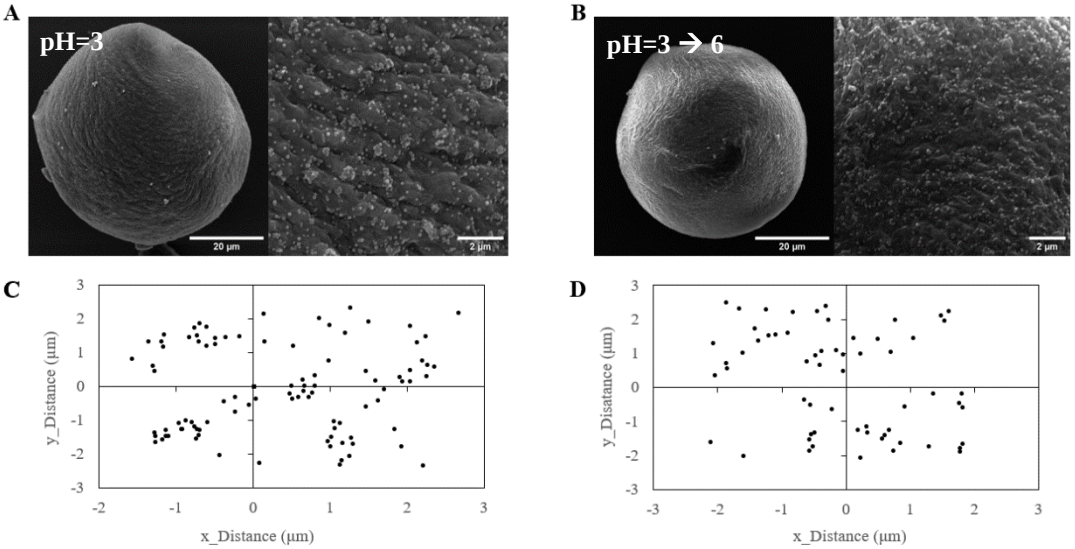

Figure 4.26 SEM micrographs of nanoparticles adsorbed-polymerized LC droplets. The LC droplets were exposed to (A) -COOH terminated silica nanoparticles with a concentration of 5.0 x 10^8 particles/mL at pH=3, (B) -COOH terminated silica nanoparticles at pH=3, and after the pH of the medium was changed to pH=6, (C) scatter map of adsorbed nanoparticles on the surface of LC droplet at pH=3 (initial state), (D) scatter map of adsorbed nanoparticles that being adsorbed at pH of 3 and changed to pH of 6 (final state).

As a second step, we aimed to unite individual adsorbed nanoparticles at a pH of 6 to several random points by changing the pH to 3 as shown in Figure 4.27. Similarly, with experiment that was mentioned in the above paragraph, we first adsorbed -COOH terminated 87.5 nm ± 7.2 nm-average-sized-silica nanoparticles (Si-COOH) with a concentration of 1.6 x 10^{10} particles/mL at pH=6 to the LC droplet (composed of reactive mesogen RM257 in 5CB (25% by weight)) and equilibrated for 1 h. We removed the free nanoparticles by changing the aqueous medium with fresh pure

water with a pH of 6. For the control group, we polymerized the nanoparticles adsorbed-LC droplets at that step. For the test group, after removing free nanoparticles from the system, we changed the pH of the medium to 3. As expected, nanoparticles exhibited homogeneous, singular, and dispersed characteristics at a pH of 6 on LC droplets (Figure 4.28A), which was confirmed by a scatter map of adsorbed nanoparticles as shown in Figure 4.28C. However, after the pH of the medium changed from 6 to 3, nanoparticles were aggregated on the LC droplet interface as shown in Figure 4.28B. The scatter map of adsorbed nanoparticles that were exposed to pH change from 6 to 3 was confirmed by the aggregation characteristics on the interface (Figure 4.28D). The change of nanoparticle characteristics upon change of medium pH to 3 resulted from a decrease in the zeta potential of -COOH terminated silica nanoparticles from -37.5 mV ± 5.2 mV to 18.5 mV ± 5.6 mV (absolute). The lower zeta potential of nanoparticles results in decreases in electrostatic repulsion or energy barrier between nanoparticles which promotes particle aggregation consistent with the experiments.

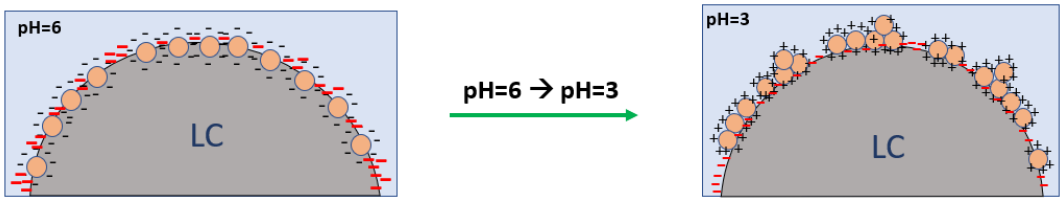

Figure 4.27 Schematic illustration of aggregating the individual adsorbed nanoparticles on LC-water interface.

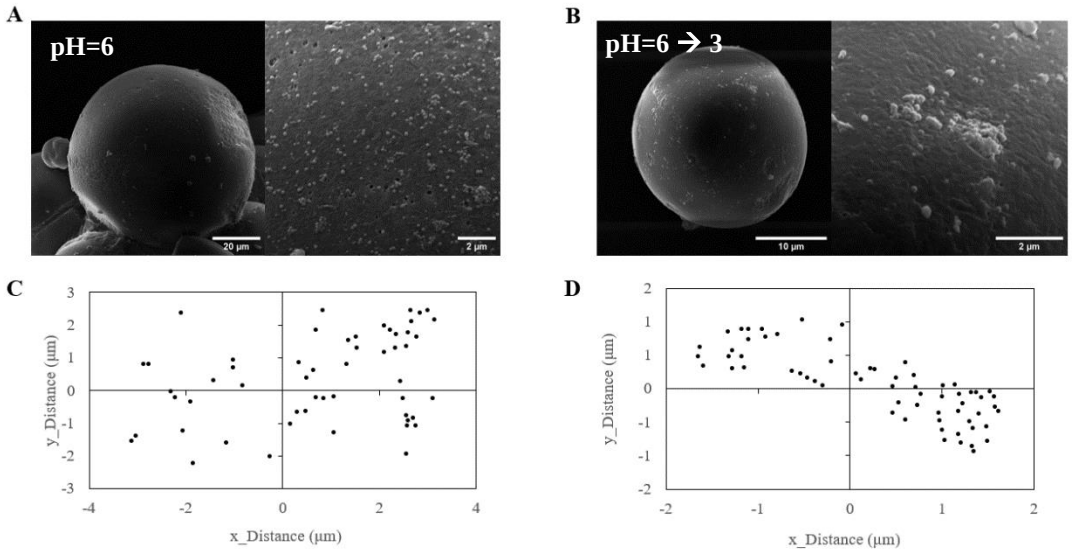

Figure 4.28 SEM micrographs of nanoparticles adsorbed-polymerized LC droplets. The LC droplets were exposed to (A) -COOH terminated silica nanoparticles with a concentration of 1.6 x 10^{10} particles/mL at pH=6, (B) -COOH terminated silica nanoparticles at pH=6 and after the pH of medium was changed to pH=3, (C) scatter map of adsorbed nanoparticles on the surface of LC droplet at pH=6 (initial state), (D) scatter map of adsorbed nanoparticles that being adsorbed at pH of 6 and changed to pH of 3 (final state).

For further investigation, we performed the response test to surface modified silica nanoparticles adsorbed LC droplets before and after pH change to see configuration change due to the nanoparticle's reorganization. For that purpose, we adsorbed nanoparticles at pH 3 or 6 and changed the pH of medium to 6 or 3, respectively, and we analyzed the configuration of LC droplets before and after pH change. As expected, bare LC droplet configuration distribution did not change with the pH of the medium, and LC droplets maintained bipolar configuration (Figure 4.29A). Although the characteristics of -COOH terminated silica nanoparticles (Si-COOH) on LC droplets were responsive to the pH change (resulted above), we did not see any configuration distribution to change, and we observed bipolar configuration (Figure 4.29B). DMOAP modified silica nanoparticles (Si-DMOAP) give strong homeotropic anchoring to the LC droplets, and the zeta potential did not depend on pH; therefore, we expect not to observe any change in the configuration after the pH change. The response of LC droplet upon adsorption of DMOAP terminated silica

nanoparticles was the radial configuration for both pH 3 and 6 for high concentrations, and we did not see a significant configuration change after the pH of the medium was altered (Figure 4.29C). The mixed monolayer of -COOH and DMOAP terminated silica nanoparticles (Si-COOH/DMOAP) gave tilted anchoring to the LC droplet, and LC droplets exhibited preradial configuration upon adsorption. Its zeta potential changed with the pH of the medium due to the -COOH group. Similar to other cases, after pH changing, the response of the LC droplets did not change, and we observed preradial configuration for high concentration (Figure 4.29D). This might because there was no desorption of nanoparticles and the partial surface coverage remained stable.

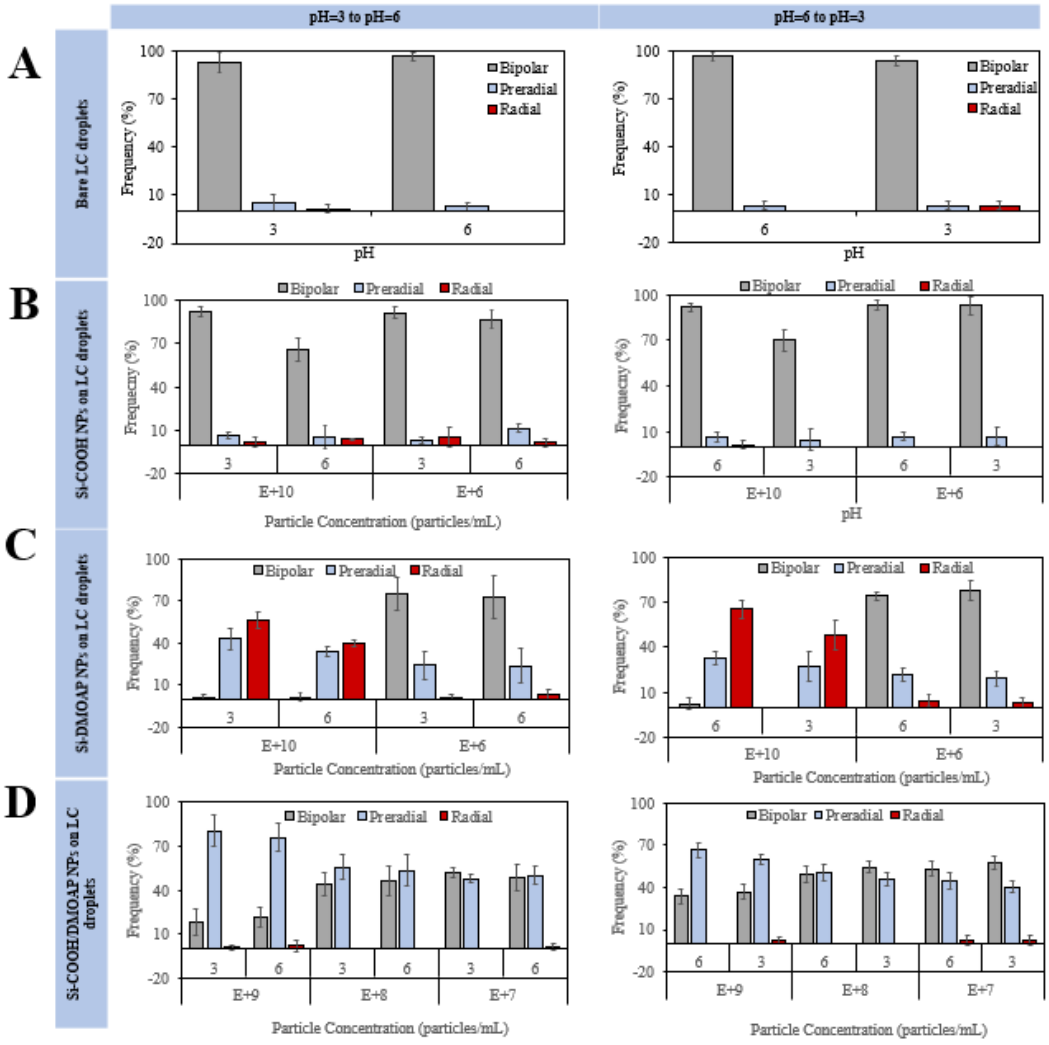

Figure 4.29 Configuration distribution of bare LC droplets or surface modified 87.5 nm sized-silica nanoparticles adsorbed LC droplets before and after pH change. The left graphs are the scenario where the nanoparticles were adsorbed at pH=3 and after pH changed to 6. The right graphs are the scenario where the nanoparticles adsorbed at pH=6 and after pH changed to 3.

The literature indicates that LC-mediated interactions lead to the formation of chains or hexagonal arrays of colloids. The symmetry and structure of the director around a particle depend on the surface anchoring condition of nanoparticles. The particle with a homeotropic anchoring condition gives dipolar or quadrupolar symmetry to the LC. Particles with a planar anchoring condition give quadrupolar symmetry[52]. Multiple micrometer-sized colloids dispersed in planar LC with dipolar or

quadrupolar symmetry forms linear or kinked chains, respectively[52,83]. In the literature, 4 μm sized-silica nanoparticles were found be form long linear chains on bipolar 150-250 μm sized-LC droplets due to the dipole–dipole interaction between like particles. In this study, the droplets were significantly larger than the colloid size, so the colloid organizations were obtained closely similar to planar LC interfaces, as mentioned before[84]. On the contrary, another study investigates the 1 μm sized polystyrene (PS) colloids on 20 μm sized LC droplets. In that study, they found chain-like, hexagonal, and pentagonal patterns according to the number of particles on LC droplets. In short, they found a chain-like structure for 3-4 numbers particles and hexagonal/pentagonal for the higher number of particles. Those structures were not observed in the aqueous-LC interface of a planar 5CB film, so they based their results on the curvature form of droplets[50]. Detailed explanations of those research can be found in the Literature Review section above. The same group also investigated nanoparticles' packing arrangements with planar anchoring on bipolar LC droplets and found the diamond-like, hexagonal arrangement to ensure minimum free energy[52]. To investigate the self-assembly and preferential adsorption of nanoparticles in detail, we tried to manipulate the packing arrangement of nanoparticles on the LC droplet. For that purpose, we used -NH_2 terminated silica nanoparticles (Si- NH_2) with a size of 87.5 nm ± 7.2 nm and 417.1 nm ± 22.1 nm, and we observed different characteristics of the colloidal arrangement. While we observed aggregated and clustered packing arrangements for 87.5 nm ± 7.2 nm-average-sized nanoparticles (Figure 4.30A), chain-like/pentagonal/hexagonal arrangements were observed for larger particles (Figure 4.30B), which is consistent with the assembly of particles resulting from the anisotropic elastic interactions induced by LC deformations at the vicinity of the adsorbed particles.

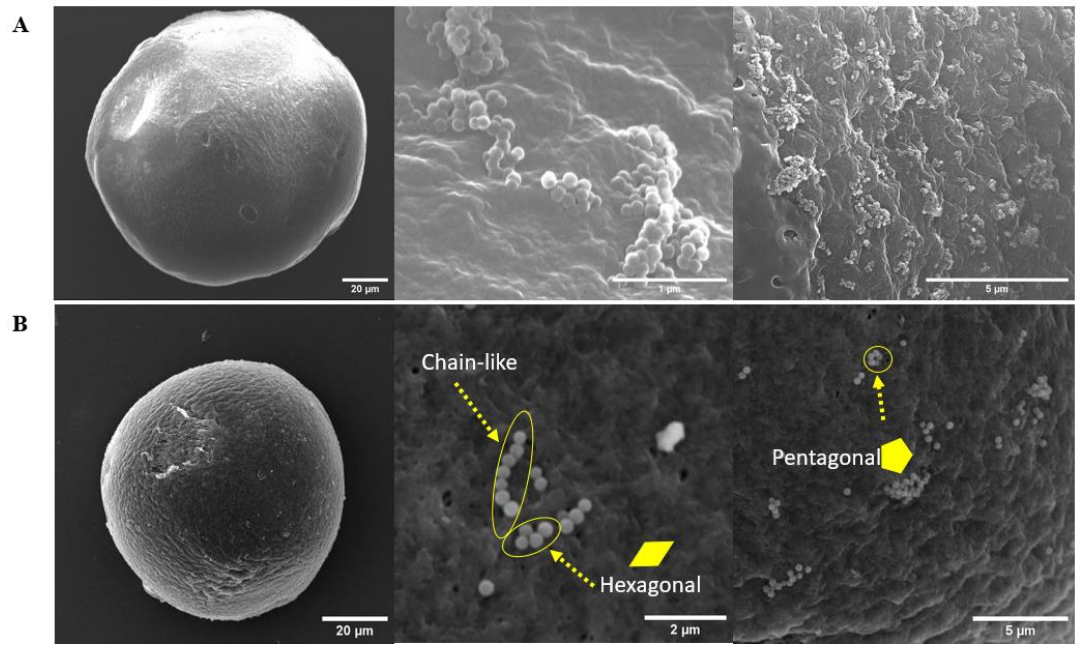

Figure 4.30 SEM micrographs of polymerized LC droplets. LC droplets were exposed to (A) -NH_2 terminated 87.5 nm ± 7.2 nm-average-sized-silica nanoparticles, (B) -NH_2 terminated 417.1 nm ± 22.1 nm-average-sized-silica nanoparticles at pH=4. The yellow arrows indicates the corresponding illusturation of patterns.

To lengthen the chain-like structure of -NH_2 terminated 417.1 nm ± 22.1 nm-average-sized-silica nanoparticles (Si-NH_2), we changed the concentration of nanoparticles. First, we used nanoparticles with a concentration of 5.0 x 10^7 particles/mL. The packing arrangement of nanoparticles formed mainly chain-like with 3.95 ± 1.14 nanoparticles, triangular and pentagonal patterns. Also, the chain-like structure was observed to be discontinuous (Figure 4.31A). Second, we increased the concentration to 8.0 x 10^8 particles/mL; and observed hexagonal, pentagonal, and chain-like structures. The chain-like structures were exhibited to be more continuous and longer (5.95 ± 1.46 particles) than 5.0 x 10^7 particles/mL scenario, as expected (Figure 4.31B).

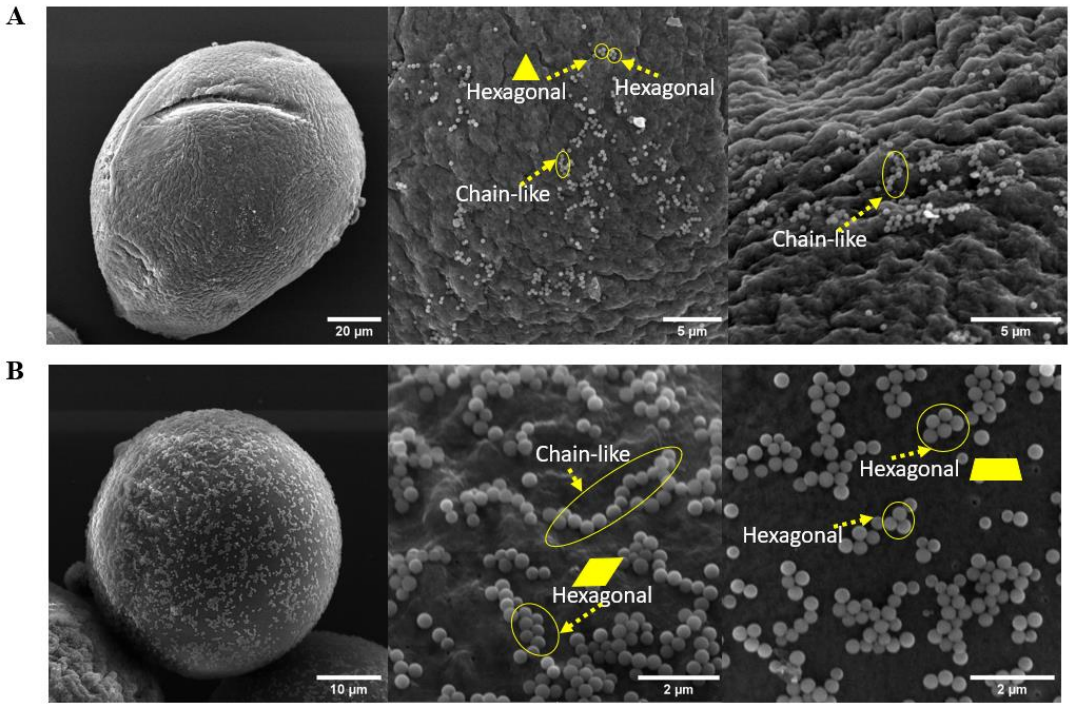

Figure 4.31 SEM micrographs of polymerized LC droplets. LC droplets were exposed to -NH_2 terminated 417.1 nm ± 22.1 nm average-sized-silica nanoparticles with concentration of (A) 5.0 x 10^7 particles/mL, (B) 8.0 x 10^8 particles/mL at pH=4. The yellow arrows indicates the corresponding illusturation of patterns.

Until this point of the study, the relationships of the same kind of surface-modified nanoparticles on the elastic medium and their effects on the LC droplet have been explained. From this point on, we aimed to control the preferential positioning of two nanoparticles with different surface modifications and sizes. We performed experiments with -NH_2 terminated 87.5 nm ± 7.2 nm-average-sized-silica nanoparticles (Si-NH_2) and -COOH terminated 51.2 nm ± 9.0 nm-average-sized-silica nanoparticles (Si-COOH) to test sequential adsorption. In this experiment, we used a pH of 4 to obtain oppositely charged nanoparticles. Zeta potential values of -NH_2 terminated 87.5 nm ± 7.2 nm-average-sized-silica nanoparticles and -COOH terminated 51.2 nm ± 9.0 nm-average-sized-silica nanoparticles were 29.5 mV ± 6.3 mV and -28.0 mV at pH=4, respectively (Figure 4.23). We first adsorbed -NH_2 terminated 87.5 nm ± 7.2 nm-average-sized-silica nanoparticles then -COOH terminated 51.2 nm ± 9.0 nmaverage-sized-silica nanoparticles at the pH=4. We

hypothesized that the attraction force between two kinds of nanoparticles allows sequential adsorption of -COOH terminated 51.2 nm ± 9.0 nm-average-sized-silica nanoparticles on the other nanoparticles. We designed an experiment where the concentration of one kind of nanoparticle was more, less, or equal to the other kind of nanoparticle. The experimental conditions can be found in Table 3. In these experiments, we analyzed the results by using the size distribution of nanoparticles on the polymerized LC droplet. We hypothesized that whichever kind of nanoparticles was more in the medium, the size distribution should be shifted to that side. For Case1, we used the same concentration of -COOH terminated 51.2 nm ± 9.0 nm-average-sized-silica nanoparticles and -NH_2 terminated 87.5 nm ± 7.2 nm-average-sized-silica nanoparticles with a concentration of 1.0 x 10^9 particles/mL (Table 3). The concentration of -COOH terminated 51.2 nm ± 9.0 nm-average-sized-silica and -NH_2 terminated 87.5 nm ± 7.2 nm-average-sized-silica nanoparticles were 1.0 x 10^9 particles/mL and 1.0 x 10^8 particles/mL for Case2, respectively (Table 3). Oppositely, the concentration of -COOH terminated 51.2 nm ± 9.0 nm-average-sized-silica and -NH_2 terminated 87.5 nm ± 7.2 nm-average-sized-silica nanoparticles were 1.0 x 10^8 particles/mL and 1.0 x 10^9 particles/mL for Case3 (Table 3). In summary, in Case1 concentration of the two kinds of nanoparticles was equal, but in Case2 and 3, one was higher than the other.

Table 3 Experimental conditions for sequential adsorption.

	Size	Particle Concentration (particles/mL)			Zeta potential (mV)
		Case1	Case2	Case3	at pH=4
LC droplet					-24.0 mV ± 8.4 mV
Si-NH_2 NPs	87.5 nm ± 7.2 nm	1.0 x 10^9	1.0 x 10^9	1.0 x 10^8	29.5 mV ± 6.3 mV
Si-COOH NPs	51.2 nm ± 9.0 nm	1.0 x 10^9	1.0 x 10^8	1.0 x 10^9	-28.0 mV

As expected, in Case1, the quantitative analysis represented almost equal number (%) nanoparticles (Figure 4.32A). 15% of the particles measured on the surface were in the 50-55 nm size range, another 15% were in the 100-105 nm size range. Particles were detected outside of these size ranges (albeit a small percentage), which may be due to error in measurement or polydisperse synthesis. In Case2, the concentration of -COOH terminated 51.2 nm ± 9.0 nm-average-sized-silica nanoparticles (Si-COOH) was higher than -NH_2 terminated 87.5 nm ± 7.2 nm-average-sized-silica nanoparticles (Si-NH_2), in parallel, size distribution shifted to the smaller sized of nanoparticles as expected (Figure 4.32B). While the highest number of particles was measured in the size range representing 51.2 nm ± 9.0 nm nanoparticles (50-55 nm), fewer particles were detected in the range representing 87.5 nm ± 7.2 nm particles (100-105 nm). Oppositely, in Case3, the concentration of -COOH terminated 51.2 nm ± 9.0 nm-average-sized-silica nanoparticles was lower than -NH_2 terminated 87.5 nm ± 7.2 nm-average-sized-silica nanoparticles, so we obtained higher frequency values for larger sized nanoparticles in size distribution analysis (Figure 4.32C). The highest number of particles was measured in the size range representing 87.5 nm ± 7.2 nm nanoparticles (100-105 nm), fewer particles were detected in the range representing 51.2 nm ± 9.0 nm particles (50-55 nm). From these experiments, we showed that sequential adsorption is possible by attraction forces.

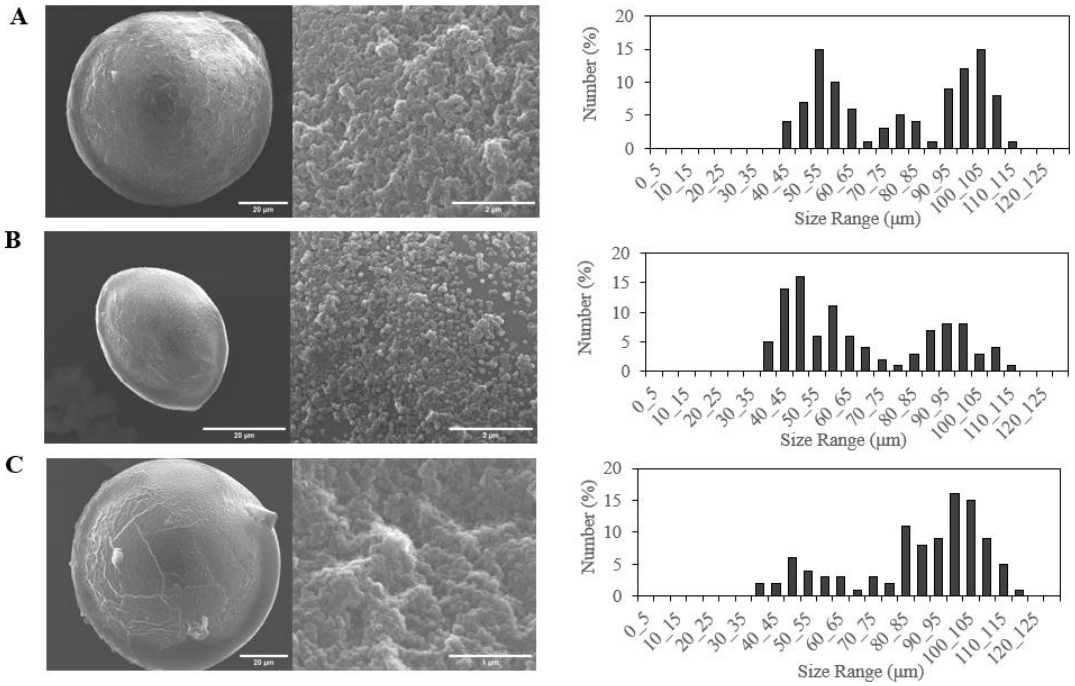

Figure 4.32 SEM micrographs of polymerized LC droplets and size distribution analysis of nanoparticles. Before polymerization LC droplets were exposed to the -NH_2 terminated 87.5 nm ± 7.2 nm-average-sized-silica nanoparticles and -COOH terminated 51.2 nm ± 9.0 nm-average-sized-silica nanoparticles with the concentrations of (A) 1.0 x 10^9 particles/mL for both nanoparticles, (B) 1.0 x 10^8 particles/mL and 1.0 x 10^9 particles/mL, (C) 1.0 x 10^9 particles/mL and 1.0 x 10^8 particles/mL, respectively.

We measured zeta potential of Case1, 2 and 3 before and after addition of -COOH terminated 51.2 nm ± 9.0 nm-average-sized-silica nanoparticles (Si-COOH) to confirm sequential adsorption and analyze the zeta potential change. At pH=4, LC droplets exhibited -24.0 mV ± 8.4 mV zeta potential. -NH_2 terminated 87.5 nm ± 7.2 nm-average-sized-silica nanoparticles (Si-NH_2), and -COOH terminated 51.2 nm ± 9.0 nm-average-sized-silica nanoparticles exhibited zeta potentials of +22.0 mV ± 6.3 mV and -17.0 mV, respectively. Before the addition of -COOH terminated 51.2 nm ± 9.0 nm-average-sized-silica nanoparticles to the system, we measured the zeta potentials of -NH_2 terminated 87.5 nm ± 7.2 nm-average-sized-silica nanoparticles adsorbed-LC droplet and it exhibited zeta potential of +14.6 mV, +24.7 mV and +11 mV, for Case 1-2 and 3, respectively (Figure 4.33). The change in bare LC droplet zeta potential from -24.0 mV ± 8.4 mV to positive values was resulted from the -

NH_2 terminated 87.5 nm ± 7.2 nm-average-sized-silica nanoparticles adsorption to the interface. After the -COOH terminated 51.2 nm ± 9.0 nm-average-sized-silica nanoparticles adsorption to the -NH_2 terminated 87.5 nm ± 7.2 nm-average-sized-silica nanoparticles adsorbed-LC droplet, we expected decrease in zeta potential for each Case because at pH of 4 -COOH terminated 51.2 nm ± 9.0 nm-average-sized-silica nanoparticles exhibited zeta potential of -17.0 mV. As expected, we measured the zeta potential of the mentioned LC droplet system as -19.9 mV, -22.6 mV and -13.0 mV for Case 1-2 and 2, respectively (Figure 4.33). The decrease in the zeta potential confirms our sequential adsorption.

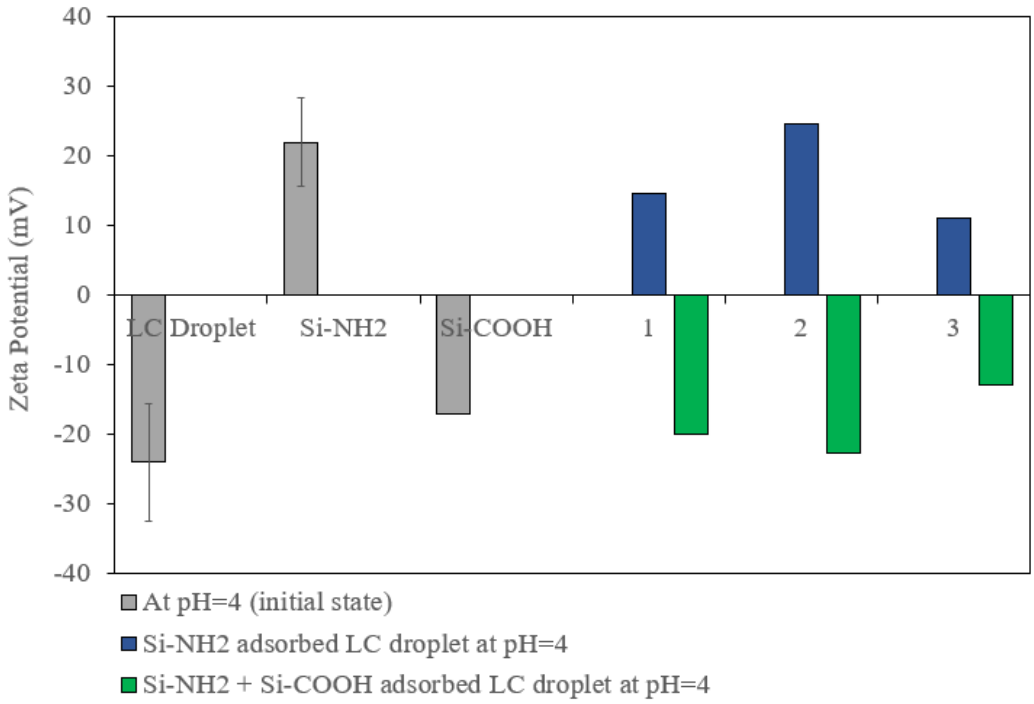

Figure 4.33 Zeta potential measurements of bare LC droplet (5CB), -NH_2 terminated 87.5 nm ± 7.2 nm-average-sized-silica nanoparticles, and -COOH terminated 51.2 nm ± 9.0 nm-average-sized-silica nanoparticles (grey bars) at pH=4, respectively. Blue bars were the zeta potential measurements of -NH_2 terminated 87.5 nm ± 7.2 nm-average-sized-silica nanoparticles adsorbed-LC droplet at pH=4. Green bars were the zeta potential measurements of sequential adsroption of -NH_2 terminated 87.5 nm ± 7.2 nm-average-sized-silica nanoparticles, and -COOH terminated 51.2 nm ± 9.0 nm-average-sized-silica nanoparticles on LC droplet at pH=4.

We already observed a long chain-like structure on LC droplets for larger-sized nanoparticles due to elastic interactions (Figure 4.30 and Figure 4.31); now, we aim to design particle assemblies where smaller-sized nanoparticles are scattered at the LC-water interface or positioned close to a long chain-like structure composed of larger-sized nanoparticles. For this purpose, we used electrostatic interactions of charged -COOH (Si-COOH) and -NH_2 terminated silica nanoparticles (Si-NH_2), which can be tuned via the pH of the suspension medium. We performed an experiment with -COOH terminated 87.5 nm ± 7.2 nm-average-sized-silica nanoparticles with a concentration of 5.0 x 10^8 particles/mL and -NH_2 terminated 417.1 nm ± 22.1 nm-average-sized-silica nanoparticles with a concentration of 1.0 x 10^9 particles/mL. LC droplets (composed of reactive mesogen RM257 in 5CB (25% by weight)) were exposed to -NH_2 terminated 417.1 nm ± 22.1 nm-average-sized-silica nanoparticles at the pH of 2. The -NH_2 terminated 417.1 nm ± 22.1 nm-average-sized-silica nanoparticles and LC droplet exhibit zeta potential values of +38.2 mV ± 20.9 mV and +23.1 mV ± 5.28 mV at pH of 2, respectively, shown in Figure 4.23. The experimental conditions are summarized in Table 4. They were both positively charged. After adsorption of -NH_2 terminated 417.1 nm ± 22.1 nm-average-sized-silica nanoparticles to the LC droplet-water interface, we allowed to naturally sediment the nanoparticles adsorbed-LC droplets and changed the supernatant with fresh pure water with a pH of 2 at least three times to remove free nanoparticles from the system. Then, -COOH terminated 87.5 nm ± 7.2 nm-average-sized-silica nanoparticles were added to the system, and we allowed them to be adsorbed for another 1 h at the pH=2. The -COOH terminated 87.5 nm ± 7.2 nm-average-sized-silica nanoparticles and LC droplet exhibit zeta potential values of +35.0 ± 7.8 mV and +23.1 mV ± 5.28 mV at pH of 2, respectively, as shown in Figure 4.23. The experimental conditions are summarized in Table 4. Again, they were both positively charged. After 1 h adsorption, we naturally sedimented LC droplets, changed the medium with fresh pure water with a pH of 2 to remove free nanoparticles and finally polymerized the LC droplets. SEM images were taken to investigate multiple nanoparticle positioning. As shown in Figure 4.34A, the -NH_2

terminated 417.1 nm ± 22.1 nm-average-sized-silica nanoparticles were found to be a long chain-like structure, as expected, but the -COOH terminated 87.5 nm ± 7.2 nm-average-sized-silica nanoparticles were seen not to be preferentially positioned, can be seen from the scatter map (Figure 4.34B). The orange dot represents the -NH_2 terminated 417.1 nm ± 22.1 nm-average-sized-silica nanoparticles, while the black dot represents the -COOH terminated 87.5 nm ± 7.2 nm-average-sized-silica nanoparticles. The orange dots were accumulated in a line shape, and black dots were distributed on x, and y coordinates, indicating no preferential positioning (Figure 4.34B). The concentration of -COOH terminated 87.5 nm ± 7.2 nm-average-sized-silica nanoparticles was not enough to cover the LC-water droplet interface, which may locate randomly. For a second step, we reduced the concentration of -NH_2 terminated 417.1 nm ± 22.1 nm-average-sized-silica nanoparticles to 8.0 x 10^8 particles/mL and increased the concentration of -COOH terminated 87.5 nm ± 7.2 nm-average-sized-silica nanoparticles to 1.0 x 10^9 particles/mL in order to observe the effects of particle concentrations and clear observation. The same experimental procedure was followed. As shown in Figure 4.34C, we decreased the concentration of -NH_2 terminated 417.1 nm ± 22.1 nm-average-sized-silica nanoparticles to 8.0 x 10^8 particles/mL; still, we observed a chain-like structure. When we increased the concentration of -COOH terminated 87.5 nm ± 7.2 nm-average-sized-silica nanoparticles, we made two observations; first, the density of nanoparticles of the LC droplet interface was also increased, and second, they were positioned randomly on the LC droplet (Figure 4.34C). Those inferences can also be seen from the scatter map, as described above (Figure 4.34D). The reason for the random adsorption on the LC droplet interface is the positive charge of these two nanoparticles which led to high repulsion forces in between nanoparticles.

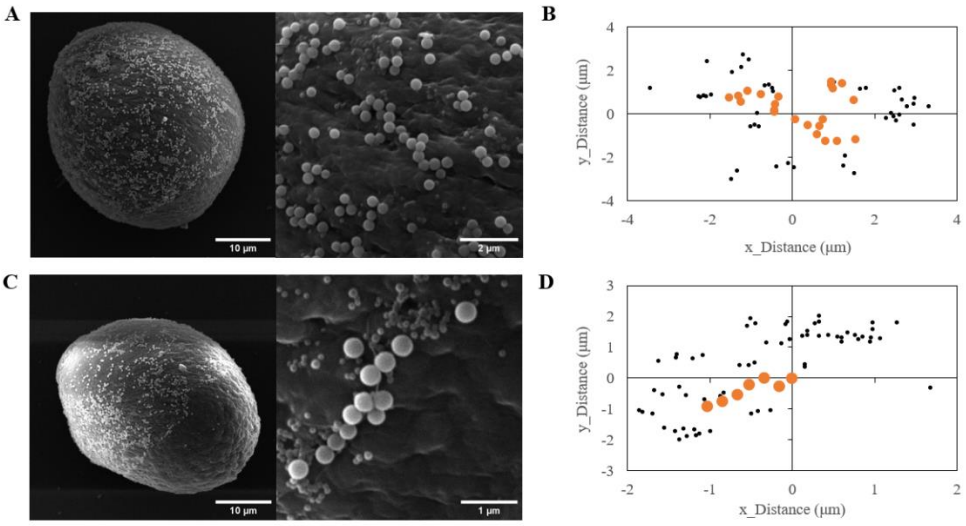

Figure 4.34 SEM micrographs of LC droplets. Before polymerization LC droplets were exposed to (A) -NH_2 terminated 417.1 nm ± 22.1 nm-average-sized-silica nanoparticles with a concentration of 1.0 x 10^9 particles/mL and -COOH terminated 87.5 nm ± 7.2 nm-average-sized-silica nanoparticles with a concentration of 5.0 x 10^8 particles/mL, (B) scatter map of nanoparticles measured from center-to-center distance, (C) -NH_2 terminated 417.1 nm ± 22.1 nm-average-sized-silica nanoparticles with a concentration of 8.0 x 10^8 particles/mL and -COOH terminated 87.5 nm ± 7.2 nm-average-sized-silica nanoparticles with a concentration of 1.0 x 10^9 particles/mL at pH=2, (D) scatter map of nanoparticles measured from center-to-center distance. Orange dots: -NH_2 terminated 417.1 nm ± 22.1 nm-average-sized-silica nanoparticles and black dots: -COOH terminated 87.5 nm ± 7.2 nm-average-sized-silica nanoparticles.

Table 4 Experimental conditions at pH=2.

	Size	**Particle Concentration (particles/mL)**		**Zeta potential (mV)**
		Group1	Group2	at pH=2
LC droplet				23.1 mV ± 5.28 mV
Si-NH_2 NPs	417.1 nm ± 22.1 nm	1.0 x 10^9	8.0 x 10^8	38.2 mV ± 20.9 mV
Si-COOH NPs	87.5 nm ± 7.2 nm	5.0 x 10^8	1.0 x 10^9	35.0 ± 7.8 mV

We repeated the same experimental procedure with the same concentration, size, and functionality of the particles, but instead of using pH=2, we used the pH of 4. At the pH=4 the zeta potential of LC droplets, -NH_2 terminated 417.1 nm ± 22.1 nm-average-sized-silica nanoparticles (Si-NH_2), and -COOH terminated 87.5 nm ± 7.2 nm-average-sized-silica nanoparticles (Si-COOH) were -18.2 mV ± 8.4 mV, +24.6 mV ± 11.5 mV, and -30.1 mV ± 7.6 mV, respectively. The experimental conditions are summarized in Table 5. In this case, the LC droplets and -COOH terminated 87.5 nm ± 7.2 nm-average-sized-silica nanoparticles exhibited negative zeta potential, but -NH_2 terminated 417.1 nm ± 22.1 nm-average-sized-silica nanoparticles exhibited positive zeta potential (Table 5). Since the -COOH terminated 87.5 nm ± 7.2 nm-average-sized-silica nanoparticles and -NH_2 terminated 417.1 nm ± 22.1 nm-average-sized-silica nanoparticles were oppositely charged (Table 5), we expected to observe those two kinds of nanoparticles were positioned to be close to each other. In Figure 4.35A, we used -NH_2 terminated 417.1 nm ± 22.1 nm-average-sized-silica nanoparticles with a concentration of 1.0 x 10^9 particles/mL at a pH of 4. We observed that the nanoparticles were positioned closer to each other than pH=2 due to the decrease in zeta potential but still formed a chain-like structure. LC droplets were exposed to the -COOH terminated 87.5 nm ± 7.2 nm-average-sized-silica nanoparticles with a concentration of 5.0 x 10^8 particles/mL at a pH of 4 with the same experimental procedure as mentioned above. However, the concentration of -COOH terminated 87.5 nm ± 7.2 nm-average-sized-silica nanoparticles at the interface was insufficient to conclude. The scatter map of this scenario indicates the disperse -COOH terminated 87.5 nm ± 7.2 nm-average-sized-silica nanoparticles at the interface; however, it could be the result of the dilute concentration of this particle (Figure 4.35B). Therefore, we increased the concentration of -COOH terminated 87.5 nm ± 7.2 nm-average-sized-silica nanoparticles to 1.0 x 10^9 particles/mL. As shown in Figure 4.35C, the density of -COOH terminated 87.5 nm ± 7.2 nm-average-sized-silica nanoparticles on the surface increased as expected, and the attraction force between -COOH terminated 87.5 nm ± 7.2 nm-average-sized-silica and -NH_2 terminated 417.1 nm ± 22.1 nm-average-sized-silica nanoparticles lead to

preferential adsorption such that the smaller sized nanoparticles located close to chain structure, which was confirmed from scatter map where the black dots follow around the orange dots (Figure 4.35D).

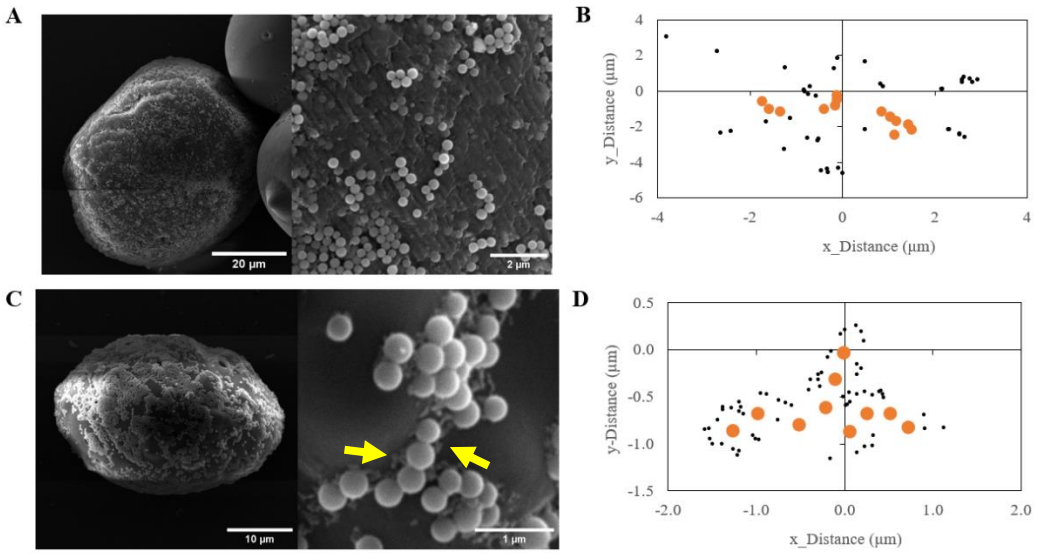

Figure 4.35 SEM micrographs of LC droplets. Before polymerization LC droplets were exposed to (A) -NH_2 terminated 417.1 nm ± 22.1 nm-avrage-sized-silica nanoparticles with a concentration of 1.0 x 10^9 particles/mL and -COOH terminated 87.5 nm ± 7.2 nm-average-sized-silica nanoparticles with a concentration of 5.0 x 10^8 particles/mL, (B) (D) scatter map of nanoparticles measured from center-to-center distance, (C) -NH_2 terminated 417.1 nm ± 22.1 nm-average-sized-silica nanoparticles with a concentration of 8.0 x 10^8 particles/mL and -COOH terminated 87.5 nm ± 7.2 nm-average-sized-silica nanoparticles with a concentration of 1.0 x 10^9 particles/mL at pH=4, (D) scatter map of nanoparticles measured from center-to-center distance.

Table 5 Experimental conditions at pH=4.

	Size	Particle Concentration (particles/mL)		Zeta potential (mV)
		Group1	Group2	at pH=4
LC droplet				-18.2 mV ± 8.4 mV
Si-NH_2 NPs	417.1 nm ± 22.1 nm	1.0 x 10^9	8.0 x 10^8	24.6 mV ± 11.5 mV
Si-COOH NPs	87.5 nm ± 7.2 nm	5.0 x 10^8	1.0 x 10^9	-30.1 mV ± 7.6 mV

We have already confirmed that nanoparticles' characteristics can be tuned on LC droplets via changing the pH of the medium with -COOH terminated 87.5 nm ± 7.2 nm-average-sized-silica nanoparticles (Si-COOH) (Figure 4.26 and Figure 4.28). We designed a complex series of experiments to detail the preferential adsorption mechanism and to observe the effect of changing system pH on preferential positioning. Changing the pH of the medium gave us to control on the surface charge of nanoparticles (Figure 4.23) and the preferential positioning (Figure 4.34 and Figure 4.35). The schematic illustration of the experiment series is given in Figure 4.36.

We divided experiments into three conditions: Group1, Group2, and Group3. In Group1-2-3, LC droplets (composed of reactive mesogen RM257 in 5CB (25% by weight)) were exposed to -NH_2 terminated 417.1 nm ± 22.1 nm-average-sized-silica nanoparticles (Si-NH_2) at a pH of 4 for 15 min. For Group1, after the adsorption of -NH_2 terminated 417.1 nm ± 22.1 nm-average-sized-silica nanoparticles at a pH=4, we naturally sedimented the LC droplets. We changed the pH of the medium to 2 after removing free nanoparticles, as mentioned before. Then, we added -COOH terminated 87.5 nm ± 7.2 nm-average-sized-silica nanoparticles (Si-COOH); and

polymerized the LC droplet after 15 min or 2 h. In this case, initially (at pH=4), LC droplets and -NH_2 terminated 417.1 nm ± 22.1 nm-average-sized-silica nanoparticles have opposite charges. LC droplets and -NH_2 terminated 417.1 nm ± 22.1 nm-average-sized-silica nanoparticles exhibited -18.2 mV ± 8.4 mV and +24.6 ± 11.5 mV, respectively. In the final situation (at pH=2), LC droplets, -NH_2 terminated 417.1 nm ± 22.1 nm-average-sized-silica nanoparticles, and -COOH terminated 87.5 nm ± 7.2 nm-average-sized-silica nanoparticles have positive charges. LC droplets, -NH_2 terminated 417.1 nm ± 22.1 nm-average-sized-silica nanoparticles and -COOH terminated 87.5 nm ± 7.2 nm-average-sized-silica nanoparticles exhibited +23.1 mV ± 5.3 mV, +38.2 mV ± 20.9 mV, and +35.0 mV ± 7.8 mV, respectively. The experimental conditions are summarized in Table 6. In this final situation, due to the high zeta potential, we expected the -COOH terminated 87.5 nm ± 7.2 nm-average-sized-silica nanoparticles would be positioned randomly and separately on the LC droplet interface.

Table 6 Experimental conditions that were used for Group1.

	Size	**Particle Concentration (particles/mL)**	**Zeta potential (mV)**	
		Group1	at pH=4 initial state	at pH=2 final state
LC droplet			-18.2 mV ± 8.4 mV	23.1 mV ± 5.3 mV
Si-NH_2 NPs	417.1 nm ± 22.1 nm	5.0 x 10^7	24.6 mV ± 11.5 mV	38.2 mV ± 20.9 mV
Si-COOH NPs	87.5 nm ± 7.2 nm	1.0 x 10^8		35.0 mV ± 7.8 mV

For Group2, after the adsorption of -NH_2 terminated 417.1 nm ± 22.1 nm-average-sized-silica nanoparticles (Si-NH_2) at pH=4, we naturally sedimented the LC droplets and changed the supernatant with a fresh pure water with a pH of 3 after removing free nanoparticles as mentioned before. Later, we added -COOH terminated 87.5 nm ± 7.2 nm-average-sized-silica nanoparticles (Si-COOH) and

polymerized the LC droplet after 15 min or 2 h. In the final situation (at pH=3), LC droplets have negative zeta potentials, but -NH_2 terminated 417.1 nm ± 22.1 nm-average-sized-silica nanoparticles and -COOH terminated 87.5 nm ± 7.2 nm-average-sized-silica nanoparticles have positive zeta potentials. LC droplets exhibited -18.2 mV ± 3.3 mV. The -NH_2 terminated 417.1 nm ± 22.1 nm-average-sized-silica nanoparticles and -COOH terminated 87.5 nm ± 7.2 nm-average-sized-silica nanoparticles exhibited +33.5 mV ± 6.6 mV and +18.5 mV ± 5.6 mV, respectively. The experimental conditions can be found in Table 7. In the final situation (at pH=3), we hypothesized that due to the positive charges of these two surface-modified nanoparticles, there would be a repulsive force between these two types of nanoparticles. Therefore, they would be positioned away from each other after 15 minutes of -COOH terminated 87.5 nm ± 7.2 nm-average-sized-silica nanoparticles. After 2 h adsorption of -COOH terminated 87.5 nm ± 7.2 nm-average-sized-silica nanoparticles, more random positioning could be observed due to the increase in the adsorption.

Table 7 Experimental conditions that were used for Group2.

	Size	**Particle Concentration (particles/mL)**	**Zeta potential (mV)**	
		Group2	at pH=4 initial state	at pH=3 final state
LC droplet			-18.2 mV ± 8.4 mV	-18.2 mV ± 3.3 mV
Si-NH_2 NPs	417.1 nm ± 22.1 nm	5.0×10^7	24.6 mV ± 11.5 mV	33.5 mV ± 6.6 mV
Si-COOH NPs	87.5 nm ± 7.2 nm	1.0×10^8		18.5 mV ± 5.6 mV

For Group3, after the adsorption of -NH_2 terminated 417.1 nm ± 22.1 nm-average-sized-silica nanoparticles (Si-NH_2) at pH=4, we did not change the pH of the medium, but we removed free nanoparticles, as before. Then, we added -COOH

terminated 87.5 nm ± 7.2 nm-average-sized-silica nanoparticles (Si-COOH); and polymerized the LC droplet after 15 min or 2 h. At pH=4, LC droplets and -COOH terminated 87.5 nm ± 7.2 nm-average-sized-silica nanoparticles exhibited negative zeta potential, -18.2 mV ± 8.4 mV and -30.1 mV ± 7.6 mV, respectively. However, $-NH_2$ terminated 417.1 nm ± 22.1 nm-average-sized-silica nanoparticles exhibited positive zeta potential +24.6 mV ± 11.6 mV, respectively. The experimental conditions are given in Table 8. It can be clearly seen that these two surface-modified nanoparticles are oppositely charged; thus we expected the particles would position close to each other due to the attraction force between these two kinds of nanoparticles after 15 min adsorption. After 2 h adsorption, we hypothesized that -COOH terminated 87.5 nm ± 7.2 nm-average-sized-silica nanoparticles could position close to $-NH_2$ terminated 417.1 nm ± 22.1 nm-average-sized-silica nanoparticles or randomly scattered on LC droplets, according to interface occupancy of nanoparticles.

Table 8 Experimental conditions that were used for Group3.

	Size	**Particle Concentration (particles/mL)**	**Zeta potential (mV)**	
		Group3	at pH=4 initial state	at pH=4 final state
LC droplet			-18.2 mV ± 8.4 mV	-18.2 mV ± 8.4 mV
Si-NH_2 NPs	417.1 nm ± 22.1 nm	5.0×10^7	24.6 mV ± 11.5 mV	24.6 mV ± 11.5 mV
Si-COOH NPs	87.5 nm ± 7.2 nm	1.0×10^8		-30.1 mV ± 7.6 mV

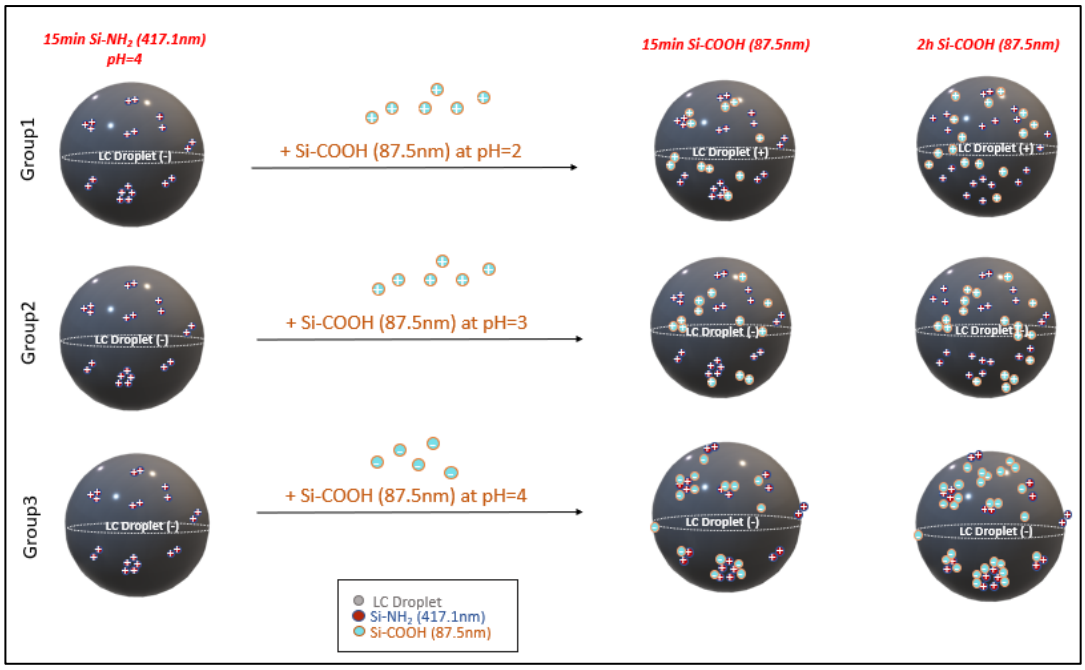

Figure 4.36 Schematic illustration of work of preferential positioning against changes in pH of medium.

We first exposed LC droplets (composed of reactive mesogen RM257 in 5CB (25% by weight)) to -NH_2 terminated 417.1 nm ± 22.1 nm-average-sized-silica nanoparticles (Si-NH_2) with a concentration of 5.0 x 10^7 particles/mL at pH of 4 and collected SEM images, as shown in Figure 4.37. The nanoparticles are adsorbed dispersedly at the interface.

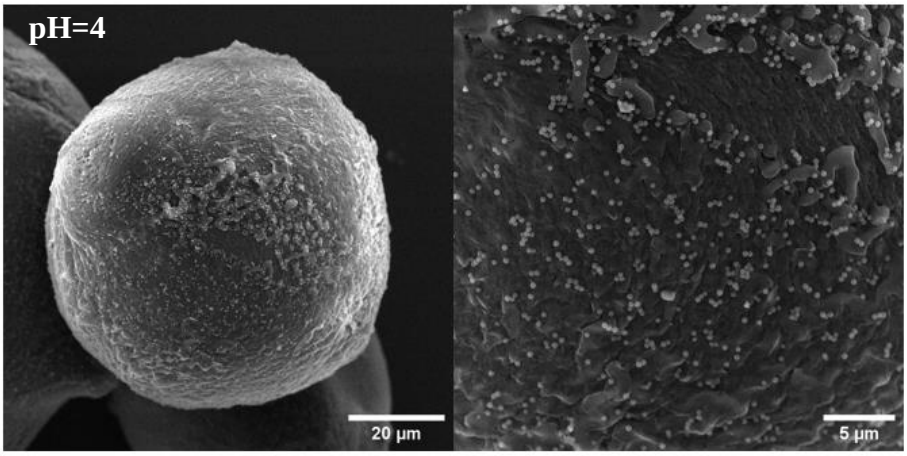

Figure 4.37 Representative SEM images of LC droplets. Before polymerization LC droplets exposed to -NH_2 terminated 417.1 nm ± 22.1 nm-average-sized-silica nanoparticles with a concentration of 5.0 x 10^7 particles/mL at pH of 4.

We performed experiments and collected SEM images for Group1 to test the hypothesis. Figure 4.38A was the representative SEM images for Group1-15 min adsorption of -COOH terminated 87.5 nm ± 7.2 nm-average-sized-silica nanoparticles (Si-COOH). We first adsorbed -NH_2 terminated 417.1 nm ± 22.1 nm-average-sized-silica nanoparticles (Si-NH_2) with a concentration of 5.0 x 10^7 particles/mL at a pH of 4, and then we added -COOH terminated 87.5 nm ± 7.2 nm-average-sized-silica nanoparticles with a concentration of 1.0 x 10^8 particles/mL at the pH=2, as described above. The experimental conditions are listed in Table 6. From the SEM images, we interpreted two essential results. Although the -COOH terminated 87.5 nm ± 7.2 nm-average-sized-silica nanoparticles positioned close to the NH_2 terminated 417.1 nm ± 22.1 nm-average-sized-silica nanoparticles after 15 min adsorption (Figure 4.38A), these two kinds of surface-modified silica nanoparticles were separate from each other and were spread over the interface of LC droplet after 2 h adsorption (Figure 4.38C). We determined that the dispersion of particles on the interface is due to the increase in surface charges and time, which are consistent with our previous experiments (Figure 4.26 and Figure 4.28). The zeta potential of -NH_2 terminated silica nanoparticles were changed from +24.6 ± 11.4 mV to +38.2 mV ± 20.9 mV when we changed the pH of medium from 4 to 2 (Table

6). Moreover -COOH terminated silica nanoparticles exhibited +35.0 mV ± 7.8 mV of zeta potential (Table 6). We used the radial distribution function to confirm our observation with a probability distribution. We found a radial distance from the center of a reference particle (-NH_2 terminated 417.1 nm ± 22.1 nm-average-sized-silica nanoparticle) to another particle (-COOH terminated 87.5 nm ± 7.2 nm-average-sized-silica nanoparticle). We measured the center-to-center distance of -COOH terminated 87.5 nm ± 7.2 nm-average-sized-silica nanoparticles to the -NH_2 terminated 417.1 nm ± 22.1 nm-average-sized-silica nanoparticles. We observed an accumulation of -COOH terminated 87.5 nm ± 7.2 nm-average-sized-silica nanoparticles close to -NH_2 terminated 417.1 nm ± 22.1 nm-average-sized-silica nanoparticles after 15 min adsorption of -COOH terminated 87.5 nm ± 7.2 nm-average-sized-silica nanoparticles. The frequency of -COOH terminated 87.5 nm ± 7.2 nm-average-sized-silica nanoparticles was higher when those positioned close to the -NH_2 terminated 417.1 nm ± 22.1 nm-average-sized-silica nanoparticles. The highest frequency of -COOH terminated 87.5 nm ± 7.2 nm-average-sized-silica nanoparticles was observed at 1.4-1.6 μm of center-to-center distance range (Figure 4.38B). We measured the center-to-center distance of -COOH and -NH_2 terminated silica nanoparticles for 2 h adsorption of -COOH terminated 87.5 nm ± 7.2 nm-average-sized-silica nanoparticles. Then, we obtained radial distribution graphs that confirmed the random distribution of -COOH terminated 87.5 nm ± 7.2 nm-average-sized-silica nanoparticles (Figure 4.38D).

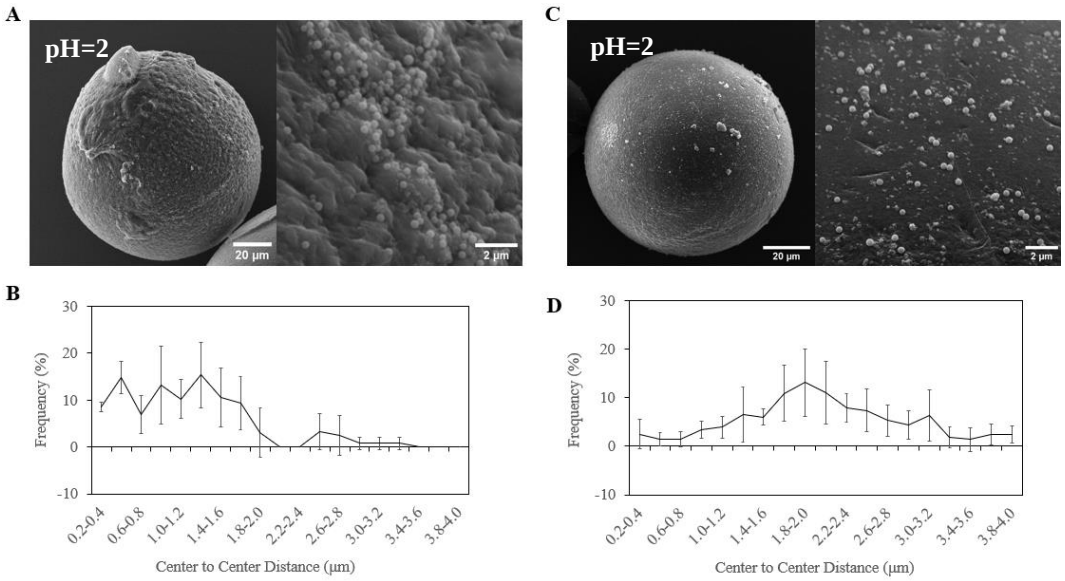

Figure 4.38 SEM micrographs of polymerized LC droplets. Before polymerization droplets were exposed to -NH_2 terminated 417.1 nm ± 22.1 nm-average-sized-silica nanoparticles with a concentration of 5.0 x 10^7 particles/mL at pH=4 for 15 min, and afterwards -COOH terminated 87.5 nm ± 7.2 nm-average-sized-silica nanoparticles with a concentration of 1.0 x 10^8 particles/mL at pH=2 (A) for 15 min adsorption, (C) for 2 h adsorption. The radial distribution graph (B) after 15 min adsorption of -COOH terminated 87.5 nm ± 7.2 nm-average-sized-silica nanoparticles, (D) after 2 h adsorption of -COOH terminated 87.5 nm ± 7.2 nm-average-sized-silica nanoparticles. SEM micrographs represented the result of Group1.

Figure 4.39A was the representative SEM images for Group2 after 15 min adsorption of -COOH terminated 87.5 nm ± 7.2 nm-average-sized-silica nanoparticles (Si-COOH). We first adsorbed -NH_2 terminated 417.1 nm ± 22.1 nm-average-sized-silica nanoparticles (Si-NH_2) with a concentration of 5.0 x 10^7 particles/mL at a pH of 4, and then we added -COOH terminated 87.5 nm ± 7.2 nm-average-sized-silica nanoparticles with a concentration of 1.0 x 10^8 particles/mL at pH=3, as described above. After 15 min adsorption, the -COOH terminated 87.5 nm ± 7.2 nm-average-sized-silica nanoparticles were found to be positioned away from -NH_2 terminated 417.1 nm ± 22.1 nm-average-sized-silica nanoparticles. The positioning characteristics of -COOH terminated 87.5 nm ± 7.2 nm-average-sized-silica nanoparticles were preserved after 2 h adsorption of -COOH terminated 87.5 nm ± 7.2 nm-average-sized-silica nanoparticles (Figure 4.39C). We confirmed our

qualitative analysis with the radial distribution function. In both cases, the frequency of -COOH terminated 87.5 nm ± 7.2 nm-average-sized-silica nanoparticles at the 0.2-0.4 μm of center-to-center distance to the -NH_2 terminated 417.1 nm ± 22.1 nm-average-sized-silica nanoparticles was the lowest. Moreover, as the center-to-center distance between the two kinds of nanoparticles increased, the probability frequency of -COOH terminated 87.5 nm ± 7.2 nm-average-sized-silica nanoparticles increased (Figure 4.39B&D). At pH=3, -NH_2 terminated 417.1 nm ± 22.1 nm-average-sized-silica nanoparticles and -COOH terminated 87.5 nm ± 7.2 nm-average-sized-silica nanoparticles exhibited zeta potential values of +33.5 mV ± 6.6 mV, and +18.5 mV ± 5.6 mV, respectively (Table 7). As expected, the two kinds of nanoparticles were positioned far apart from each other because of the repulsion force between them.

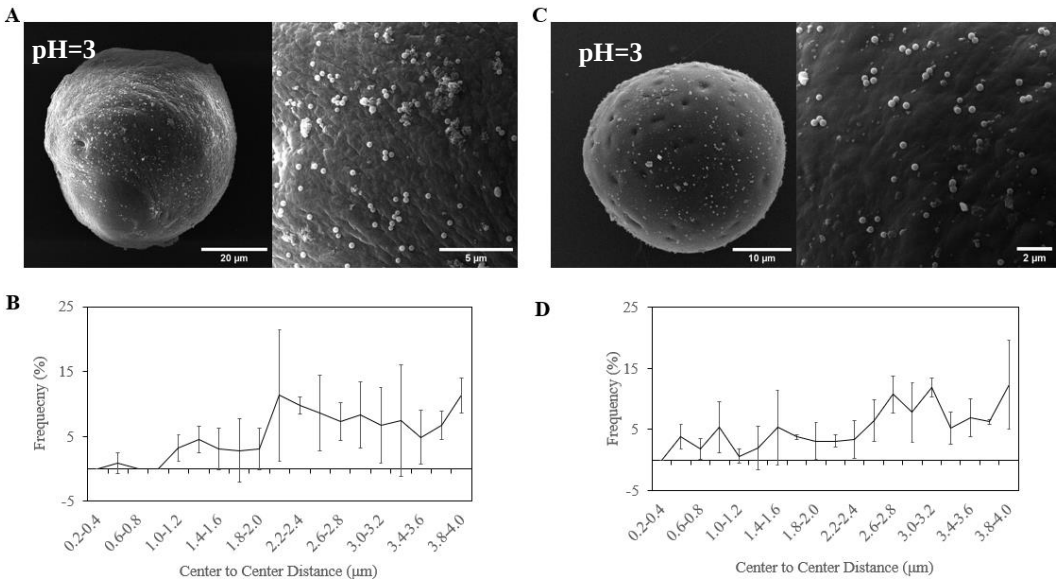

Figure 4.39 SEM micrographs of polymerized LC droplets. Before polymerization droplets were exposed to -NH_2 terminated 417.1 nm ± 22.1 nm-average-sized-silica nanoparticles with a concentration of 5.0 x 10^7 particles/mL at pH=4 for 15 min, and afterwards -COOH terminated 87.5 nm ± 7.2 nm-average-sized-silica nanoparticles with a concentration of 1.0 x 10^8 particles/mL at pH=3 (A) for 15 min adsorption, (C) for 2 h adsorption. The radial distribution graph (B) after 15 min adsorption of -COOH terminated 87.5 nm ± 7.2 nm-average-sized-silica nanoparticles, (D) after 2 h adsorption of -COOH terminated 87.5 nm ± 7.2 nm-average-sized-silica nanoparticles. SEM micrographs represented the result of Group2.

Finally, Figure 4.40A was the representative SEM images for Group3 after 15 min adsorption of -COOH terminated 87.5 nm ± 7.2 nm-average-sized-silica nanoparticles (Si-COOH). In this Group, we did not change the pH of the medium after the adsorption of -NH_2 terminated 417.1 nm ± 22.1 nm-average-sized-silica nanoparticles (Si-NH_2). The experimental conditions are in Table 8. After 15 min adsorption, the -COOH terminated 87.5 nm ± 7.2 nm-average-sized-silica nanoparticles were found to be positioned close to -NH_2 terminated 417.1 nm ± 22.1 nm-average-sized-silica nanoparticles. The -COOH terminated 87.5 nm ± 7.2 nm-average-sized-silica nanoparticles were positioned to fill the vacancies between -NH_2 terminated 417.1 nm ± 22.1 nm-average-sized-silica nanoparticles (Figure 4.40A). After 2 h adsorption of -COOH terminated 87.5 nm ± 7.2 nm-average-sized-silica nanoparticles, we observed a more homogeneous interface (Figure 4.40C). Our quantitative analysis showed that the probability frequency of the -COOH terminated 87.5 nm ± 7.2 nm-average-size silica nanoparticles decreased and finally became almost zero when the center-to-center distance exceeded 1.6 μm for 15 min adsorption. The highest probability frequency was found as 20% at 0.8-1.0 μm of the center-to-center range (Figure 4.40B). Although we observed a more homogeneous surface for 2 h adsorption from the SEM micrographs, the frequency of -COOH terminated 87.5 nm ± 7.2 nm-average-sized-silica nanoparticles was higher at a closer distance range (0.2-2.0 μm). However, the frequency was not decreased below 2.2% (Figure 4.40D). The increase in the frequency of the particle probability when the center-to-center distance is more than 2.0 μm indicates nanoparticle diffusion to the interface.

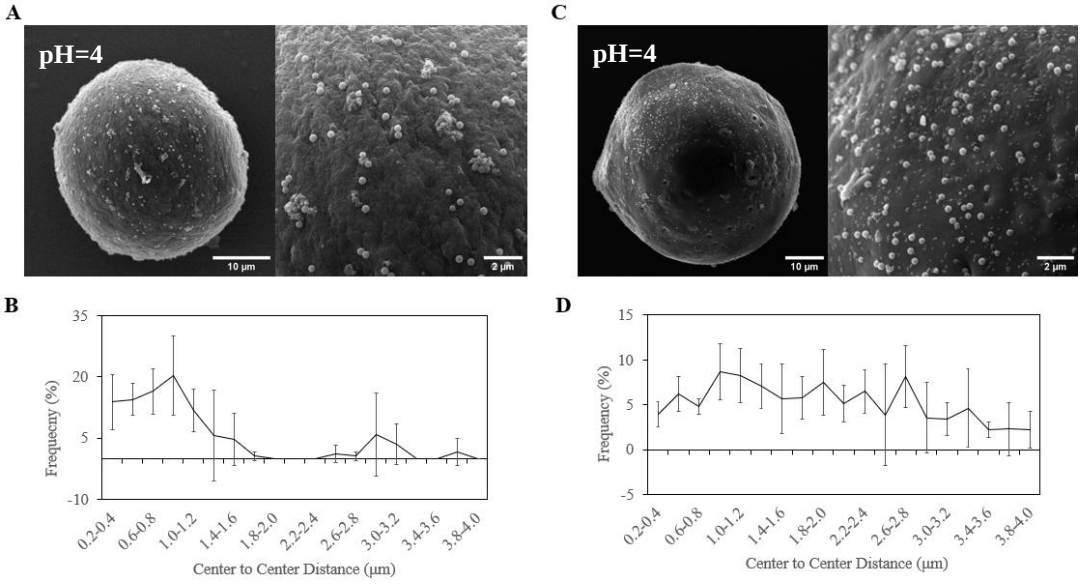

Figure 4.40 SEM micrographs of polymerized LC droplets. Before polymerization droplets were exposed to -NH_2 terminated 417.1 nm ± 22.1 nm-average-sized-silica nanoparticles with a concentration of 5.0 x 10^7 particles/mL at pH=4 for 15 min, and afterwards -COOH terminated 87.5 nm ± 7.2 nm-average-sized-silica nanoparticles with a concentration of 1.0 x 10^8 particles/mL at pH=4 (A) for 15 min adsorption, (C) for 2 h adsorption. The radial distribution graph (B) after 15 min adsorption of -COOH terminated 87.5 nm ± 7.2 nm-average-sized-silica nanoparticles, (D) after 2 h adsorption of -COOH terminated 87.5 nm ± 7.2 nm-average-sized-silica nanoparticles. This SEM micrographs represented the result of Group3.

To analyze the internal structure of polymerized LC droplets decorated with nanoparticles, a polarized optical microscope (POM) was used. Due to the anisotropic structure of polymer matrix, we expected a birefringent appearance of the synthesized micrometer-sized polymer composite particles as in the literature[21]. We used -COOH terminated 87.5 nm ± 7.2 nm-average-sized-silica nanoparticles (Si-COOH), and DMOAP/ -COOH mixed monolayer terminated silanes functionalized 87.5 nm ± 7.2 nm-average-sized-silica nanoparticles (Si-COOH/DMOAP) with the concentration of 1.2 x 10^9 particles/mL and adsorbed them to LC-water interface in ultra-pure water. After adsorption, non-reactive mesogens were extracted from the medium, and polymer composite particles dispersed in the pure water or dropped onto the glass slide and left to dry. The POM images of polymer composite particles were taken for both dry and dispersed in an

ultra-pure water sample, as shown in Figure 4.41. Drying the sample results in pronounced shrinkage of the LC droplets; however, the sample dispersed in the pure water does not. For each group, radial polymer particles were identified from the center defect (from the bright field) and cross-like petal signature (from the dark field) (Figure 4.41A(iii)-B(iii)-C(iii)-D(iii)). Preradial configuration was identified from a single surface defect as shown in Figure 4.41A(ii)-B(ii)-C(ii)-D(ii). Bipolar configurations were identified single point bright appearance from the dark field as shown in Figure 4.41A(i)-B(i)-C(i)-D(i). Even if the images were taken with the same exposure level, the brightness and bright area (in diameter) of the dry samples were observed to be less than the samples that dispersed in pure water, which indicates the shrinkage of dry particles (Figure 4.41A(iii)-B(iii)-C(iii)-D(iii)). The light that passes through the samples that dispersed in pure water spreads over a much wider angle which means the scattering of incident light. This phenomenon enhances brightness (more wide area) and transmittance [85]. However, shrinkage of LC droplets leads to a denser structure that hinders transmittance and brightness; therefore we observed less brightness and smaller bright area. POM images of LC droplets confirm the anisotropic polymer composite particles with a complex internal structure that results from surface-modified nanoparticle adsorption. The characteristic signature of configurations was conserved, which shows the polymerization took place according to the orientation of the LC molecules, as expected.

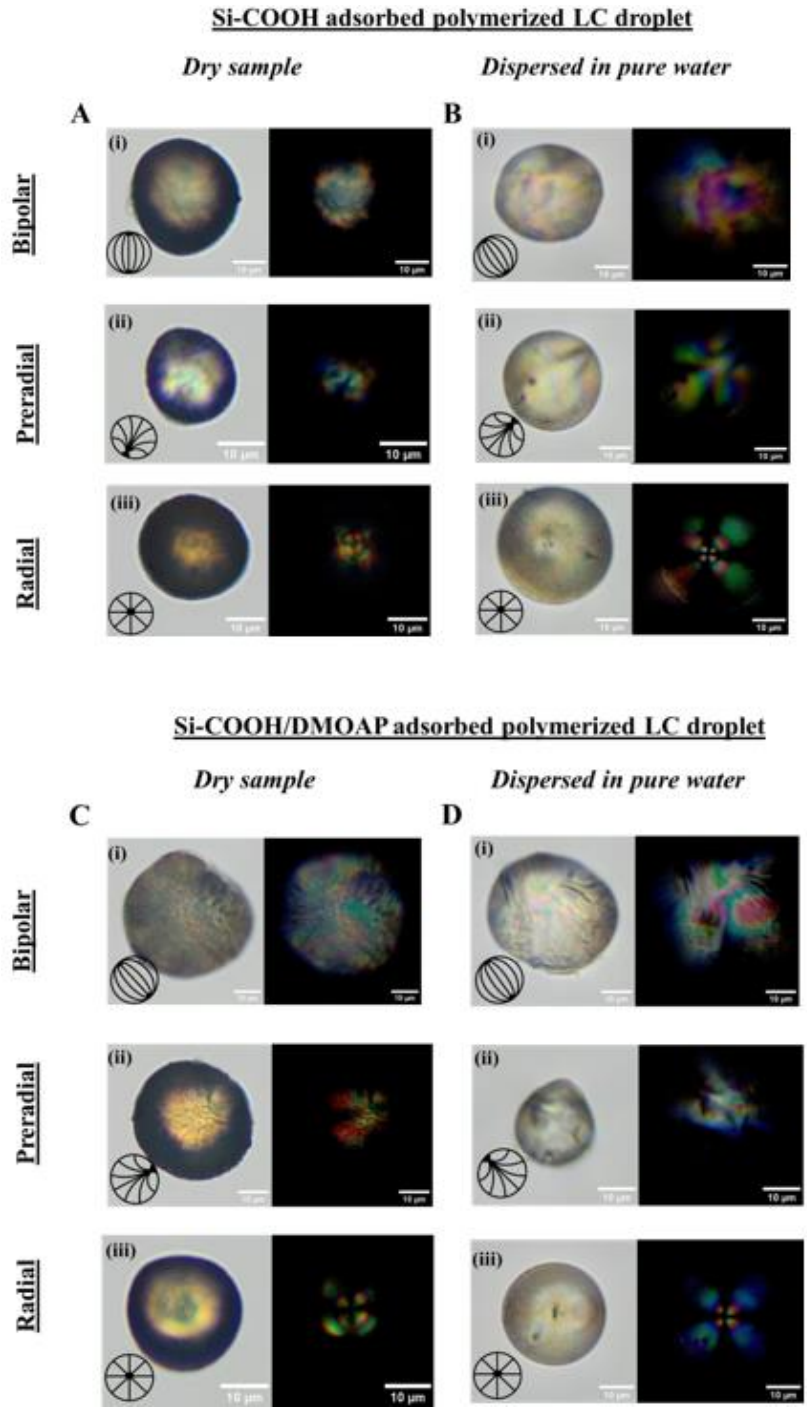

Figure 4.41 POM images of polymerized LC droplet. (A) Dry sample of Si-COOH adsorbed polymerized LC droplet, (B) Si-COOH adsorbed polymerized LC droplet dispersed in pure water, (C) dry sample of Si-COOH/DMOAP adsorbed polymerized LC droplet, (D) Si-COOH adsorbed polymerized LC droplet dispersed in pure water. Bipolar, preradial, and radial configurations were given in (i), (ii), and (iii), respectively, for each group of samples.

Finally, we analyzed the configuration distribution of polymer composite particles templated from LC droplets. Interestingly, we obtained configuration distribution for Si-COOH adsorbed polymerized LC droplet rather than only bipolar configuration (Figure 4.11D and Figure 4.42). Similarly, the radial configuration frequency increased for Si-COOH/DMOAP adsorbed polymerized LC droplets for same concentration of nanoparticles (Figure 4.12A and Figure 4.42). The increase in the preradial and radial configuration for both cases might result from the RM257, which causes the LC to maintain a tilted orientation at the droplet interface in pure water[20]. In the literature, the axial configurations were obtained when reactive LC mixture (20% wt/wt RM257/5CB) was emulsified in pure water for the droplet size 5-20 μm, which is near our size range. Also, preradial and radial configurations were obtained when a reactive LC mixture composed of 30% wt/wt RM257/5CB[21]. In our experiments, we used a reactive LC mixture composed of 25% wt/wt RM257/5CB, and we comment here that RM257 in the 5CB droplet induces the increasing frequencies of preradial or radial configurations through its influence on either the elastic or surface anchoring of the nematic reactive mixture, as in literature[21].

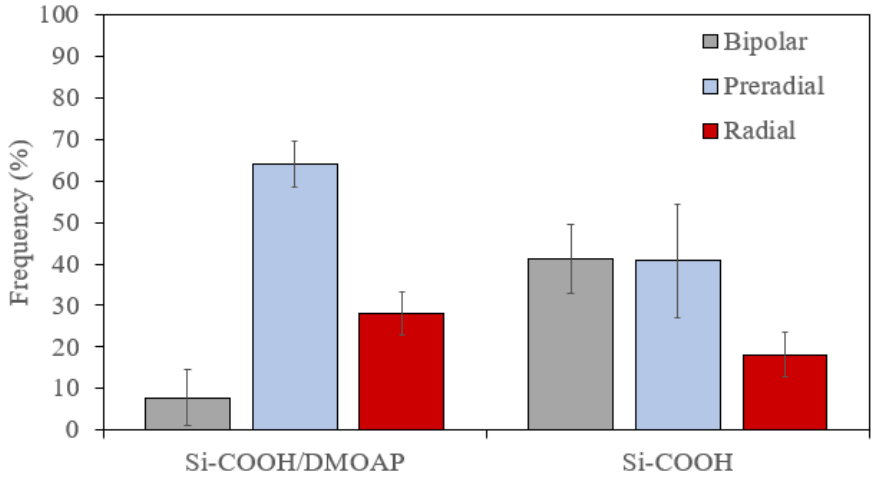

Figure 4.42 Configuration distribution of polymerized LC droplets dispersed in pure water. LC droplets were exposed to surface-modified nanoparticles with a concentration of 1.2 x 10^9 particles/mL before polymerization.

Overall, this study reveals that composite particles with controlled internal and interfacial structuring can be synthesized using surface-modified nanoparticle-adsorbed LC droplets as templates. Also, we provide information about interparticle interactions on an elastic medium. Finely tuned interparticle interactions allow designing self-assembly of nanoparticles to the interface of an elastic medium. The polymeric particles can be synthesized with various surface properties with different nanoparticles. For instance, silver nanoparticles are known to be an antibacterial material. Antibacterial properties of LC templated-composite particles can be adjusted by optimizing the concentration of silver nanoparticles on the surface of LC droplets. Moreover, movable, and self-directed LC templated composite particles can be obtained by optimizing the magnetic properties of LC templated-composite particles. Surface functionalized mesoporous silica nanoparticles can be loaded with biological tools such as drugs and dyes for treatment and diagnosis. Therefore, an analytical on-demand release system can be optimized. Besides drug delivery and imaging systems, materials that can be used in many technologic applications can be developed by positioning more than one nanomaterial with different surface properties (magnetic, antibacterial, hydrophobic, hydrophilic, catalytic, charging, etc.) on the interface in an adjustable manner. Moreover, shape control of polymeric particles is an important parameter for microparticles, as mentioned before. This study not only provides a synthesis of LC templated-composite microparticles with complex internal structures but also gives direction about multiple preferential positioning of nanoparticles to LC droplet by using charged nanoparticles. Comprehensive energy of elastic LC and with the assistance of optical tweezers or surfactant-induced particle spacing have been used for particle assembly on 2D or 3D substrates[15,27]. Alternatively, this study can be broadened to applications for assembly of multiple and different nanoparticles positioning without to need of surfactant or equipment.

To further improve our study, different characterization methods with fluidic, optical, and signal detection/processing systems like flow cytometer can be introduced instead of an optical microscope to save time. Microfluidic devices can

be used to generate monodisperse droplet size. Besides optical investigation, imaging of fractured polymeric LC droplets can be analyzed via SEM and TEM to investigate the internal structure of polymeric particles.

CHAPTER 5

CONCLUSION

This study provided a method for the synthesis of polymeric composite microparticles with complex internal and interfacial structuring using surface-modified nanoparticles-adsorbed LC droplets as a template material. We highlighted a concentration and surface chemistry-dependent configuration change upon adsorption of surface-modified silver, iron oxide, and silica nanoparticles to the LC-water interface; by this way, pre-determined internal structuring control over the polymeric network was offered. The advantage of the surface charging property of surface-modified nanoparticles was used and it provided adsorption control. Tuning the electrostatic interactions of nanoparticles enabled preferential positioning of nanoparticles on an elastic medium, which showed control over interfacial structuring and heterogeneity. Our study differed by using the elastic interactions to tune the control over the multiple nanoparticle adsorption and by investigating the LC droplet configuration change against metal base nanoparticles with different surface properties. This study procured fundamental information about interparticle interactions on an elastic medium and a synthesis method for polymeric composite particles that can be broadened to technological advancements. The findings we arrived at herein can be extended such that the LC templated-composite particles with magnetic properties can be detailed to obtain a self-direction mechanism and moveable particles. LC droplets decorated with nanoparticles can be exposed to external stimuli (magnetic/electric field, light, heat, etc.) that interact with nanoparticles to obtain pre-determined conditions for polymeric particles. Different LC phases confined in droplets, especially cholesteric LC, can be studied for preferential positioning of multiple nanoparticles since the cholesteric LC phase has line defects near to surface, which is energetically favorable for colloidal assemblies at the LC droplet-water interface.

REFERENCES

1. Oka, C., Ushimaru, K., Horiishi, N., Tsuge, T. & Kitamoto, Y. Core-shell composite particles composed of biodegradable polymer particles and magnetic iron oxide nanoparticles for targeted drug delivery. *J. Magn. Magn. Mater*. **381**, 278–284 (2015).

2. Gander, B., Gurny, R., Doelker, E. & Peppas, N. A. Effect of polymeric network structure on drug release from cross-linked poly (vinyl alcohol) micromatrices. *Pharm. Res.* **6**, (1989).

3. Bubb, D. M. *et al.* Laser-based processing of polymer nanocomposites for chemical sensing applications. *J. Appl. Phys.* **89**, 5739–5746 (2001).

4. Halim, A. *et al.* Soft polymeric nanoparticle additives for next generation gas separation membranes. *J. Mater. Chem.* **2**, 4999–5009 (2014).

5. Moaddeb, M. & Koros, W. J. Gas transport properties of thin polymeric membranes in the presence of silicon dioxide particles. *J. Membr. Sci* **125**, 143–163 (1997).

6. Zhang, M., Otanicar, T. P., Phelan, P. E. & Dai, L. L. Multipetal-Structured and Dumbbell-Structured Gold-Polymer Composite Particles with Self-Modulated Catalytic Activity. *Langmuir* **31**, 13191–13200 (2015).

7. Ho, K. M., Li, W. Y., Wong, C. H. & Li, P. Amphiphilic polymeric particles with core-shell nanostructures: Emulsion-based syntheses and potential applications. *Colloid Polym. Sci.* **288**, 1503–1523 (2010).

8. Champion, J. A., Katare, Y. K. & Mitragotri, S. Particle shape: A new design parameter for micro- and nanoscale drug delivery carriers. *J. Control. Release* **121**, 3–9 (2007).

9. Madivala, B., Vandebril, S., Fransaer, J. & Vermant, J. Exploiting particle shape in solid stabilized emulsions. *Soft Matter* **5**, 1717–1727 (2009).

10. Lu, S., Ramos, J. & Forcada, J. Monodisperse magnetic polymeric composite particles for biomedical applications. *Macromol. Symp.* **281**, 89–95 (2009).

11. Liu, Y. D. & Choi, H. J. Recent progress in smart polymer composite particles in electric and magnetic fields. *Polym. Int.* **62**, 147–151 (2013).

12. Sutar, R. S. *et al.* Superhydrophobic Al2O3–Polymer Composite Coating for Self-Cleaning Applications. *Coatings* **11**, (2021).

13. Mondiot, F., Wang, X., de Pablo, J. J. & Abbott, N. L. Liquid crystal-based emulsions for synthesis of spherical and non-spherical particles with chemical patches. *J. Am. Chem. Soc.* **135**, 9972–9975 (2013).

14. Muševič, I., Škarabot, M., Tkalec, U., Ravnik, M. & Žumer, S. Two-dimensional nematic colloidal crystals self-assembled by topological defects. *Science (1979)* **313**, 954–958 (2006).

15. Bukusoglu, E., Pantoja, M. B., Mushenheim, P. C., Wang, X. & Abbott, N. L. Design of Responsive and Active (Soft) Materials Using Liquid Crystals. *Annu Rev Chem Biomol Eng* **7**, 163–196 (2016).

16. Wang, D., Park, S. Y. & Kang, I. K. Liquid crystals: Emerging materials for use in real-time detection applications. *J. Mater. Chem. C* **3**, 9038–9047 (2015).

17. Gupta, J. K., Zimmerman, J. S., de Pablo, J. J., Caruso, F. & Abbott, N. L. Characterization of adsorbate-induced ordering transitions of liquid crystals within monodisperse droplets. *Langmuir* **25**, 9016–9024 (2009).

18. Prischepa, O. O., Shabanov, A. & Zyryanov, V. Y. Transformation of director configuration upon changing boundary conditions in droplets of nematic liquid crystal. *JETP Lett* **79**, 315–319 (2004).

19. Miller, D. S., Wang, X. & Abbott, N. L. Design of functional materials based on liquid crystalline droplets. *Chem. Mater.* **26**, 496–506 (2014).

20. Wang, X., Bukusoglu, E. & Abbott, N. L. A practical guide to the preparation of liquid crystal-templated microparticles. *Chem. Mat.* **29**, 53–61 (2017).

21. Wang, X. *et al.* Synthesis of Optically Complex, Porous, and Anisometric Polymeric Microparticles by Templating from Liquid Crystalline Droplets. *Adv. Funct. Mater.* **26**, 7343–7351 (2016).

22. Akdeniz, B. & Bukusoglu, E. Design Parameters and Principles of Liquid-Crystal-Templated Synthesis of Polymeric Materials via Photolithography. *Langmuir* **35**, 13126–13134 (2019).

23. Karausta, A., Kocaman, C. & Bukusoglu, E. Controlling the shapes and internal complexity of the polymeric particles using liquid crystal-templates confined into microwells. *J. Mol. Liq.* **324**, (2021).

24. Karausta, A. & Bukusoglu, E. Liquid Crystal-Templated Synthesis of Mesoporous Membranes with Predetermined Pore Alignment. *ACS Appl. Mater. Interfaces.* **10**, 33484–33492 (2018).

25. Akdeniz, B. & Bukusoglu, E. Liquid Crystal Templates Combined with Photolithography Enable Synthesis of Chiral Twisted Polymeric Microparticles. *Macromol. Rapid Commun.* **40**, (2019).

26. Lee, J. H., Kamal, T., Roth, S. v., Zhang, P. & Park, S. Y. Structures and alignment of anisotropic liquid crystal particles in a liquid crystal cell. *RSC Adv.* **4**, 40617–40625 (2014).

27. Koenig, G. M., Lin, I. H. & Abbott, N. L. Chemoresponsive assemblies of microparticles at liquid crystalline interfaces. *Proc. Natl. Acad. Sci. U.S.A.* **107**, 3998–4003 (2010).

28. Şengül, S., Aydoğan, N. & Bukusoglu, E. Nanoparticle adsorption induced configurations of nematic liquid crystal droplets. *J. Colloid Interface Sci.* **608**, 2310–2320 (2022).

29. Lavrentovich, O. D. Transport of particles in liquid crystals. *Soft Matter* **10**, 1264–1283 (2014).

30. Omi, S., Ken', I., Katami, A. & Yamamoto, M. Synthesis of Polymeric Microspheres Employing SPG Emulsification Technique. *J. Appl. Polym. Sci.* **51**, 1–11 (1993).

31. Lu, S. & Forcada, J. Preparation and characterization of magnetic polymeric composite particles by miniemulsion polymerization. *J. Polym. Sci. A Polym. Chem.* **44**, 4187–4203 (2006).

32. Chen, J. H., Cheng, C. Y., Chiu, W. Y., Lee, C. F. & Liang, N. Y. Synthesis of ZnO/polystyrene composites particles by Pickering emulsion polymerization. *Eur. Polym. J.* **44**, 3271–3279 (2008).

33. Zheng, G., Wu, J., Wang, W. & Pan, C. Characterizations of expanded graphite/polymer composites prepared by in situ polymerization. *Carbon N Y* **42**, 2839–2847 (2004).

34. Guan, J., Ferrell, N., James Lee, L. & Hansford, D. J. Fabrication of polymeric microparticles for drug delivery by soft lithography. *Biomaterials* **27**, 4034–4041 (2006).

35. Nunes, J. K., Ertas, M., Du, L. & DeSimone, J. M. Hierarchical control of polymer composite nano- and micro-structure with lithography. *Chem. Mater.* **22**, 4069–4075 (2010).

36. Dendukuri, D., Pregibon, D. C., Collins, J., Hatton, T. A. & Doyle, P. S. Continuous-flow lithography for high-throughput microparticle synthesis. *Nat. Mater.* **5**, 365–369 (2006).

37. Karnik, R. *et al.* Microfluidic platform for controlled synthesis of polymeric nanoparticles. *Nano Lett.* **8**, 2906–2912 (2008).

38. Burow, M. & Minoura, N. Molecular Imprinting: Synthesis of Polymer Particles with Antibody-like Binding Characteristics for Glucose Oxidase. *Biochem. Biophys. Res. Commun.* **227**, 419–422 (1996).

39. Avşar, D. I. & Bukusoglu, E. Chameleon skin-inspired polymeric particles for the detection of toluene vapor. *Soft Matter* **16**, 8683–8691 (2020).

40. Batir, O., Bat, E. & Bukusoglu, E. Interpenetrating network based polymeric sensors with enhanced specificity, sensitivity, and reusability. *Sens. Actuators B Chem.* **367**, (2022).

41. Shah, R. R. & Abbott, N. L. Orientational transitions of liquid crystals driven by binding of organoamines to carboxylic acids presented at surfaces with nanometer-scale topography. *Langmuir* **19**, 275–284 (2003).

42. Shah, R. R. & Abbott, N. L. Principles for measurement of chemical exposure based on recognition-driven anchoring transitions in liquid crystals. *Science (1979)* **293**, 1296–1299 (2001).

43. Cadwell, K. D., Alf, M. E. & Abbott, N. L. Infrared spectroscopy of competitive interactions between liquid crystals, metal salts, and dimethyl methylphosphonate at surfaces. *J. Phys. Chem. B* **110**, 26081–26088 (2006).

44. Malone, S. M. & Schwartz, D. K. Macroscopic liquid crystal response to isolated DNA helices. *Langmuir* **27**, 11767–11772 (2011).

45. Gupta, V. K., Skaife, J. J., Dubrovsky, T. B. & Abbott, N. L. Optical Amplification of Ligand-Receptor Binding Using Liquid Crystals. *Science (1979)* **279**, 2077–2080 (1998).

46. Lockwood, N. A., Gupta, J. K. & Abbott, N. L. Self-assembly of amphiphiles, polymers and proteins at interfaces between thermotropic liquid crystals and aqueous phases. *Surf. Sci. Rep.* **63**, 255–293 (2008).

47. Brake, J. M., Daschner, M. K., Luk, Y. Y. & Abbott, N. L. Biomolecular Interactions at Phospholipid-Decorated Surfaces of Liquid Crystals. *Science (1979)* **302**, 2094–2097 (2003).

48. Brake, J. M. & Abbott, N. L. An experimental system for imaging the reversible adsorption of amphiphiles at aqueous-liquid crystal interfaces. *Langmuir* **18**, 6101–6109 (2002).

49. Loudet, J.-C., Barois, P. & Poulin, P. Colloidal ordering from phase separation in a liquid-crystalline continuous phase. *Nature* **407**, (2000).

50. Wang, X., Miller, D. S., de Pablo, J. J. & Abbott, N. L. Organized assemblies of colloids formed at the poles of micrometer-sized droplets of liquid crystal. *Soft Matter* **10**, 8821–8828 (2014).

51. Wang, X., Miller, D. S., de Pablo, J. J. & Abbott, N. L. Reversible switching of liquid crystalline order permits synthesis of homogeneous populations of dipolar patchy microparticles. *Adv. Funct. Mater.* **24**, 6219–6226 (2014).

52. Rahimi, M. *et al.* Nanoparticle self-assembly at the interface of liquid crystal droplets. *Proc. Natl. Acad. Sci. U.S.A.* **112**, 5297–5302 (2015).

53. Stober, W., Fink, A. & Ernst Bohn, D. Controlled Growth of Monodisperse Silica Spheres in the Micron Size Range. *J. Colloid Interface Sci.* **26**, 62–69 (1968).

54. Topuz, B., Şimşek, D. & Çiftçioɨlu, M. Preparation of monodisperse silica spheres and determination of their densification behaviour. *Ceram. Int.* **41**, 43–52 (2015).

55. Yang, J. *et al.* Monodisperse core-shell structured magnetic mesoporous aluminosilicate nanospheres with large dendritic mesochannels. *Nano Res.* **8**, 2503–2514 (2015).

56. Steinigeweg, D. & Schlücker, S. Monodispersity and size control in the synthesis of 20–100 nm quasi-spherical silver nanoparticles by citrate and

ascorbic acid reduction in glycerol–water mixtures. *ChemComm* **48**, 8682–8684 (2012).

57. Koenig, G. M. *et al.* Single nanoparticle tracking reveals influence of chemical functionality of nanoparticles on local ordering of liquid crystals and nanoparticle diffusion coefficients. *Nano Lett.* **9**, 2794–2801 (2009).

58. Beganskienė, A., Sirutkaitis, V., Kurtinaitienė, M., Juškėnas, R. & Kareiva, A. FTIR, TEM and NMR Iinvestigations of Stöber Silica Nanoparticles. *Medziagotyra* **10**, (2004).

59. An, Y., Chen, M., Xue, Q. & Liu, W. Preparation and self-assembly of carboxylic acid-functionalized silica. *J. Colloid Interface Sci.* **311**, 507–513 (2007).

60. Koenig, G. M., de Pablo, J. J. & Abbott, N. L. Characterization of the reversible interaction of pairs of nanoparticles dispersed in nematic liquid crystals. *Langmuir* **25**, 13318–13321 (2009).

61. Li, S. *et al.* Solvothermal synthesis and characterization of monodisperse superparamagnetic iron oxide nanoparticles. *J. Magn. Magn. Mater.* **379**, 226–231 (2015).

62. Yadav, V. K. *et al.* Synthesis and characterization of amorphous iron oxide nanoparticles by the sonochemical method and their application for the remediation of heavy metals from wastewater. *Nanomaterials* **10**, 1–17 (2020).

63. England, C. G., Miller, M. C., Kuttan, A., Trent, J. O. & Frieboes, H. B. Release kinetics of paclitaxel and cisplatin from two and three layered gold nanoparticles. *Eur. J. Pharm. Biopharm.* **92**, 120–129 (2015).

64. Gojzewski, H., Kappl, M. & Ptak, A. Effect of the Chain Length and Temperature on the Adhesive Properties of Alkanethiol Self-Assembled Monolayers. *Langmuir* **33**, 11862–11868 (2017).

65. Tao, A. *et al.* Langmuir-Blodgett silver nanowire monolayers for molecular sensing using surface-enhanced Raman spectroscopy. *Nano Lett.* **3**, 1229–1233 (2003).

66. Drawhorn, R. A. & Abbott, N. L. Anchoring of Nematic Liquid Crystals on Self-Assembled Monolayers Formed from Alkanethiols on Semitransparent Films of Gold. *J. Phys. Chem* **99**, 16511–16515 (1995).

67. Wang, J. & Yoon, R. H. AFM forces measured between gold surfaces coated with self-assembled monolayers of 1-hexadecanethiol. *Langmuir* **24**, 7889–7896 (2008).

68. Palombo, M., Gabrielli, A., Servedio, V. D. P., Ruocco, G. & Capuani, S. Structural disorder and anomalous diffusion in random packing of spheres. *Sci. Rep.* **3**, (2013).

69. Gupta, J. K., Sivakumar, S., Caruso, F. & Abbott, N. L. Size-dependent ordering of liquid crystals observed in polymeric capsules with micrometer and smaller diameters. *Angew. Chem. Int. Ed.* **48**, 1652–1655 (2009).

70. Tjipto, E. *et al.* Tailoring the interfaces between nematic liquid crystal emulsions and aqueous phases via layer-by-layer assembly. *Nano Lett.* **6**, 2243–2248 (2006).

71. Ansar, S. M., Chakraborty, S. & Kitchens, C. L. pH-responsive mercaptoundecanoic acid functionalized gold nanoparticles and applications in catalysis. *Nanomaterials* **8**, (2018).

72. Simsikova, M., Antalík, M., Kaňuchová, M. & Škvarla, J. Anionic 11-mercaptoundecanoic acid capped ZnO nanoparticles. *Appl. Surf. Sci.* **282**, 342–347 (2013).

73. Jayalath, S., Larsen, S. C. & Grassian, V. H. Surface adsorption of Nordic aquatic fulvic acid on amine-functionalized and non-functionalized mesoporous silica nanoparticles. *Environ. Sci. Nano* **5**, 2162–2172 (2018).

74. Otalvaro, J. O., Avena, M. & Brigante, M. Adsorption of organic pollutants by amine functionalized mesoporous silica in aqueous solution. Effects of pH, ionic strength and some consequences of APTES stability. *J. Environ. Chem. Eng.* **7**, (2019).

75. Wu, T. H. *et al.* Determination of functionalized gold nanoparticles incorporated in hydrophilic and hydrophobic microenvironments by surface modification of quartz crystal microbalance. *Appl. Surf. Sci.* **274**, 418–424 (2013).

76. Bagwe, R. P., Hilliard, L. R. & Tan, W. Surface modification of silica nanoparticles to reduce aggregation and nonspecific binding. *Langmuir* **22**, 4357–4362 (2006).

77. Capco, D. G. & Chen, Y. *Nanoparticle Aggregation Principles and Modeling*. (Springer, 2014).

78. Nanda, H. S. Surface modification of promising cerium oxide nanoparticles for nanomedicine applications. *RSC Adv.* **6**, 111889–111894 (2016).

79. Smalyukh, I. I., Lavrentovich, O. D., Kuzmin, A. N., Kachynski, A. v. & Prasad, P. N. Elasticity-mediated self-organization and colloidal interactions of solid spheres with tangential anchoring in a nematic liquid crystal. *Phys. Rev. Lett.* **95**, (2005).

80. Škarabot, M. *et al.* Laser trapping of low refractive index colloids in a nematic liquid crystal. *Phys. Rev. E Stat. Nonlin. Soft Matter Phys.* **73**, (2006).

81. Kotar, J. *et al.* Interparticle potential and drag coefficient in nematic colloids. *Phys. Rev. Lett.* **96**, (2006).

82. Vialetto, J. & Anyfantakis, M. Exploiting Additives for Directing the Adsorption and Organization of Colloid Particles at Fluid Interfaces. *Langmuir* **37**, 9302–9335 (2021).

83. Karabot, M. & Muevi, I. Direct observation of interaction of nanoparticles in a nematic liquid crystal. *Soft Matter* **6**, 5476–5481 (2010).

84. Gharbi, M. A., Nobili, M. & Blanc, C. Use of topological defects as templates to direct assembly of colloidal particles at nematic interfaces. *J. Colloid Interface Sci.* **417**, 250–255 (2014).

85. Luo, S., Xue, J., Xiong, Y., Shen, J. & Guo, S. Light-scattering properties of linear low density polyethylene/polystyrene films fabricated through layer-multiplying technology. *J. Appl. Polym. Sci.* **133**, (2016).